technische universität
dortmund

Interaction dynamics of Rydberg excitons in Cu_2O

Dissertation

Submitted in partial fulfilment of the requirements for the Degree of

Dr. rer. nat.

to the faculty of physics of the
TU Dortmund University, Germany

by
Binodbihari Panda

Accepted by the Faculty of Physics of the TU Dortmund University, Germany

Day of the oral examination: 25th February, 2025

Examination board:

Prof. Dr. Marc Aßmann
Prof. Dr. Zhe Wang
Prof. Dr. Jelger Risselada
Jun. Prof. Dr. Benedikt Fauseweh

Abstract

An exciton is a Coulomb-bound complex of an electron in the conduction band and a hole in the valence band, typically existing in semiconductors and insulators. Cuprous oxide, Cu_2O, is a semiconductor that hosts highly-excited states of excitons, referred to as Rydberg excitons akin to their atomic counterparts, Rydberg atoms. To date, Rydberg excitons with principal quantum numbers up to $n = 30$ have been observed.

The primary factor limiting the further extension of the Rydberg exciton series is the presence of charged impurities or defects, which are inherent to most semiconductors and serve as a major source of charge noise. Thus, a pristine sample devoid of such impurities is essential for any applications sensitive to charge noise. This thesis first demonstrates a technique to reduce charged impurities in semiconductors using Rydberg excitons, referred to as purification. Secondly, the dynamics of purification is studied using time-resolved pump-probe spectroscopy. A careful analysis of the intricate relaxation of the signal after the end of the pump pulse uncovers underlying physical mechanisms of the purification process and provides insights into the exciton-impurity interactions. Lastly, a comprehensive study of the interaction dynamics of Rydberg excitons with other carriers, such as other excitons, electron-hole plasma and impurities, is performed under several excitation scenarios.

Contents

List of Acronyms

RE Rydberg excitons

CW Continuous wave

EF Electric field

TR Time-resolved

FWHM Full width half maximum

PL Photoluminescence

e-h electron-hole

BEIC Bound exciton-impurity complex

Fig. Figure

i.e. That is

e.g. For example

TMM Transfer matrix method

ITO Indium tin oxide

Chapter 1

Introduction

The early history of semiconductors can be aptly summarized by the phrase: "From Faraday to Yesterday" [71]. It began with Faraday's investigation into the temperature dependence of silver sulfide (Ag_2S) and continued to evolve until the invention of transistor in 1947 [46]. Copper oxide (Cu_2O), as a semiconductor, holds a unique place in both physics and industry. Its story begins in 1874 when Arthur Schuster observed the rectification (asymmetric current-voltage response) while making a circuit made up of copper wires bound by screws [61, 71]. The rectification effect became more pronounced if the circuit was left unused for a long time, and it disappeared with the cleaning of copper wires, i.e. the removal of Cu_2O layers. This accidental observation marked the discovery of Cu_2O as a semiconductor. Later, in the early 1920s, L. O. Grondahl demonstrated the rectifying properties of Cu - Cu_2O junctions, paving the way for the first commercial rectifier and its widespread adoption in industrial applications until silicon became dominant in the 1950s [26].

In the early 1950s, Cu_2O drew renewed attention with the discovery of the first-ever excitons in any material, following independent theoretical predictions by Frenkel [22] and Wannier [112] in the late 1930s. An exciton is essentially a Coulomb-bound complex of an electron and a hole, typically observed in semiconductors and insulators. The excitons of the yellow-series up to principal quantum number $n = 8$ were demonstrated by Hayashi et al. [30] and E. Gross et al. [27,28]. Due to the high Rydberg energy ($\sim$90 meV) of excitons in Cu_2O compared to other semiconductors and the availability of high-quality natural crystals, the observation of high-n excitons was anticipated, and significant efforts had been put to further extend the exciton series. These efforts showed minor success in 1996, when Matsumoto et al. extended the exciton series up to $n = 12$ [66]. In 2014, the discovery of excitons with principal quantum number up to $n = 25$ by Kazimierczuk et al. [51] marked the beginning of a new era. It evoked a comparison between these excitons with Rydberg

atoms due to their large spatial extensions, spanning over a billion crystal unit cells, and accordingly, their huge dipole moment. For example, the radius of exciton with $n = 25$ is 1.04 μm, which is comparable to the radius of a hydrogen atom excited to the Rydberg state $n = 140$ ($r_n = 0.53\mathring{A} \times n^2$). These exaggerated properties justify referring to them as Rydberg excitons. Moreover, another analogy between Rydberg atoms and Rydberg excitons may be drawn due to a peculiar property known as Rydberg blockade [39]. When an exciton (or atom) is optically excited to a Rydberg state, the energy required to excite a second exciton (or atom) in its vicinity to a Rydberg state will be modified due to the long-ranged van der Waals interaction acting between the particles. If the energy separation is larger than the linewidth of the laser used for excitation, it is impossible for the second exciton (or atom) to transit to the Rydberg state within a certain volume near the first one. This effect is known as Rydberg blockade, and the corresponding volume is referred to as blockade volume.

In addition to these similarities, excitons differ from atoms in three key aspects [3]. First, excitons are quasi-particles that exist within a solid-state medium which screens Coulomb interactions. Second, while the proton and electron masses in atoms differ considerably, the effective masses of the electron and hole in an exciton are relatively similar. Both factors reduce the Rydberg energy of excitons. Finally, the ground state of an atom is the $1S$ state, whereas, for an exciton, it is the excitonic vacuum state.

The survival of a research field often hinges on its societal utility and technological applicability. While technologies utilizing Rydberg interactions in atoms, such as qubits [1, 84], logic gates [94], etc., have been successfully demonstrated, similar technologies based on Rydberg excitons are yet to be developed. However, over the past few years, much scientific progress has been made that could steer the field of Rydberg exciton towards technological applications. The primary focus is laid on exploiting the huge non-linearity that Rydberg excitons offer. Recently, Morin et al. [68] demonstrated a self-Kerr effect near the resonances of Rydberg excitons. The corresponding non-linear refractive index (n_2) is on the order of 10^{-3} mm^2 /mW, which is at least 3 orders of magnitude larger than n_2 found in atomic medium and 14 orders of magnitude larger than typical nonlinear crystals [32, 59, 67, 111]. Such large Kerr nonlinearity from Rydberg excitons makes them ideal candidate for studying non-linear quantum optics at the few-photon levels [12, 65, 77] and opens up the possibility to develop optical modulators, optical switches, frequency combs, etc.. Pritchett et al. [78] demonstrated a similar Kerr non-linearity in the microwave regime, which could be useful for sensing microwave radiation and conversion of microwaves to optical frequencies. Rydberg exciton-polaritons, which arises from the hybridization of excitons and photons inside a cavity, also shows a similar large Kerr effect, albeit 8 orders of magnitude smaller than for bulk Cu_2O [63]. A major limitation of this

type of resonantly enhanced Kerr nonlinearity is its narrow bandwidth, which renders these mediums unsuitable for broadband applications.

To enable quantum applications that exploit these giant optical nonlinearities, the confinement of Rydberg excitons must be comparable to the size of Rydberg blockade. Paul et al. [73], using focused-ion-beam etching, and Barua et al. [5], through a CMOS-compatible growth technique, have achieved confinement of Rydberg excitons at the micron scale. This confinement allows for local tuning of Rydberg exciton energies through optically induced temperature changes, potentially advancing photon-based scalable quantum simulation. However, only Rydberg excitons with a principal quantum number up to $n = 8$ have been observed in these platforms, likely due to strain or charged impurities in the crystal [37].

In general, most semiconductor devices which exploit excitons and spin states are prone to decoherence arising from charge noise and imperfections of crystal. Thus, high-quality crystals containing low-density charge sources are required to improve the efficiency of such devices. The two main sources of charge in semiconductors include inherent charged impurities, and mobile free charge carriers referred to as electron-hole plasma. A quantitative assessment of their densities is of fundamental interest in determining the quality of a crystal. Rydberg excitons are shown to be a sensitive probe for such charges and can be used for sensing applications [32]. However, along with quantification, the removal of such charges is essential for technological applications.

The present thesis addresses the following issues.

- How can crystal quality be improved, or charged impurities and defects be removed?
- What are the underlying interaction mechanisms of Rydberg excitons and their dynamics?

The thesis is structured as follows: Chapter 2 outlines the theoretical framework necessary to understand the present thesis. Chapter 3 discusses a technique to reduce the impact of charged impurities in semiconductors using high-n Rydberg excitons, a process referred to as 'Purification'. Additionally, Rydberg excitons serve as a highly polarizable medium which can be utilized to neutralize external uniform electric fields. The dynamics of purification, along with interactions of Rydberg excitons with various entities, are discussed in chapter 4 and 5, respectively. This offers insights into the underlying interaction mechanisms of Rydberg excitons.

Chapter 2

Linear absorption spectroscopy of Cu_2O

In this chapter, the key concepts essential to understanding the physics discussed in this thesis are briefly introduced. We begin by presenting the theory of light-matter interaction in semiconductors in section 2.1. Both the scenarios of the weak and strong coupling of light and matter are explained concisely and separately. In section 2.2, the crystal and electronic band structure of the material Cu_2O which is investigated in this thesis are summarized in detail, aiding in the understanding of its optical properties. The concept of excitons is presented in section 2.3. Following this, the high-resolution linear one-photon absorption spectrum of the yellow exciton series of Cu_2O is demonstrated. In section 2.4, the dipole-dipole interaction between Rydberg excitons (RE) is introduced, with emphasis on van der Waals and Förster-type interactions. Lastly, an overview of the interaction between RE and a low-density electron-hole plasma is provided in section 2.5. Based on a quantum many-body theory, the influence of plasma on excitonic lineshape parameters and the band edge is described, and a rate model is used to explain the dynamical changes.

2.1 Light-matter interaction

In this section, we discuss the fundamental microscopic theory that governs the interaction between light and matter. Depending on the strength of light-matter interaction, we distinguish between weak and strong coupling.

2.1.1 Weak coupling regime

In the scenario of weak coupling, both the electromagnetic field and elementary excitations of matter are treated as independent entities or weakly interacting. Therefore, the approach to describing light-matter interaction is based on the framework of perturbation theory.

The theory presented here is mostly derived from the book Semiconductor Optics by Prof. Claus F. Klingshrin [54]. To begin with, we consider a two-level system formed by either the ground and excited states of an atom or by two electronic bands of a solid or any emitters. The transition rate (Γ_{if}) of an electron between two levels in the presence of an electromagnetic field is of interest, and, according to the Fermi Golden rule, it is given by

$$\Gamma_{if} = \frac{2\pi}{\hbar} \left|H_{if}\right|^2 D_f(E), \tag{2.1}$$

where $D_f(E)$ is the density of final states, which depends upon energy, and $H_{if} = \left\langle \psi_f \right| H \left| \psi_i \right\rangle$ is the transition matrix element of the total Hamiltonian H of the system. If m_e is the mass and p_e is the momentum of a single electron subjected to an electrostatic potential $V(r)$, the Hamiltonian H_e is given by

$$H_e = \frac{p_e^2}{2m_e} + V(r). \tag{2.2}$$

Using classical electrodynamics, the interaction of the electrons and electromagnetic field can be best described by the modified Hamiltonian

$$H_e' = \frac{(p_e + eA)^2}{2m_e} + V(r) - e\phi(r), \tag{2.3}$$

where the additional terms A and ϕ are the vector and scalar potential of the electromagnetic wave, respectively. Under the condition of Coulomb gauge, i.e. $\bigtriangledown A = 0$ and $\phi = 0$, and replacing momentum p_e with quantum mechanical operator $\frac{\hbar}{i}\bigtriangledown$

$$\begin{aligned} H_e' &= \frac{1}{2m_e}\left(-\hbar^2 \bigtriangledown^2 + \frac{\hbar}{i} eA \bigtriangledown + e^2A^2\right) + V(r) \\ &= H_e + \frac{e}{m_e} A \cdot P_e + \frac{e^2}{2m_e} A^2, \end{aligned} \tag{2.4}$$

where the vector potential is given by

$$A = A_0 \hat{e} \cdot e^{i(kr - \omega t)}. \tag{2.5}$$

A_0 is the amplitude and $\hat{e}$ defines the polarization direction. Moreover, k and ω are the wave vector and angular frequency of the electromagnetic wave, respectively. The magnitude of k is inversely proportional to the wavelength, i.e. $|k| = \frac{2\pi}{\lambda}$.

As mentioned earlier, we treat the light field perturbatively. Thus, the amplitude A can be assumed to be very small, which allows us to neglect the last term in Eq. 2.4. The second term of Eq. 2.4, i.e. $H_{int} = \frac{e}{m_e} A \cdot P_e$, is the first-order perturbation term responsible

for the optical transition. Therefore, the transition rate (Γ_{if}) from Eq. 2.1 is given by

$$\begin{aligned}\Gamma_{if} &= \frac{2\pi}{\hbar}\left|\left\langle\psi_f\right| H_{int}\left|\psi_i\right\rangle\right|^2 D_f(E) \\ &= \frac{2\pi}{\hbar}\left|\left\langle\psi_f\right| \frac{e}{m_e} A\cdot P_e\left|\psi_i\right\rangle\right|^2 D_f(E).\end{aligned} \tag{2.6}$$

The point to note is that both the radius of an atom (i.e. $r \simeq 0.1$ nm) and the distance between neighbouring atoms (i.e. lattice constant $a \simeq 0.3$ nm) for a solid are way smaller than the wavelength of visible light ($\lambda \simeq 500$ nm). Therefore, the phase shift ($k\cdot r$) of the light field when travelling across an atom and between two adjacent atoms is almost zero. This allows us to expand the term

$$e^{ikr} = 1 + \frac{ikr}{1!} + \frac{(ikr)^2}{2!} + \ldots\ldots\ldots \approx 1 + \frac{ikr}{1!}. \tag{2.7}$$

Thus, the transition matrix element can be written as

$$H_{if} = \left\langle\psi_f\right| H_1\left|\psi_i\right\rangle \approx \frac{eA_0}{m_e}\left\langle\psi_f\right|(\hat{e}\cdot p)\left|\psi_i\right\rangle + \frac{ieA_0}{m_e}\left\langle\psi_f\right|(\hat{e}\cdot p)(k\cdot r)\left|\psi_i\right\rangle. \tag{2.8}$$

The first term in the expression above describes electric-dipole transitions, while the second term encompasses both magnetic dipole and electric quadrupole transitions. Under the so-called dipole approximation, only the first term is considered.

Purcell effect

A manifestation of weak light-matter coupling is the Purcell effect, i.e. the change in the rate of spontaneous emission inside a cavity compared to free space [49, 72]. Essentially, when light is confined in a cavity and in resonance with the cavity field mode, its density of states, $D_f(E)$, is modified in comparison to free space. This leads to a change in the spontaneous emission rate (see Eq. 2.1).

According to Refs. [53, 72], for photons that obey a linear dispersion relation (E= $\hbar\omega$= $\hbar ck$), the 3D density of states in free space is given by

$$D_0(\omega) = \frac{\omega^2 V n^3}{\pi^2 c^3}, \tag{2.9}$$

where c is the speed of light in vacuum, ω is the angular frequency of light, n is the refractive index of medium (for vacuum n = 1) and V is the mode volume. In contrast to free space, the modified density of states in a cavity is [53, 72]

$$D_c(\omega) = \frac{2}{\pi} \frac{\Delta\omega_c^2}{4(\omega - \omega_c)^2 + \Delta\omega_c^2}. \tag{2.10}$$

Here, ω_c is the resonant frequency of the cavity and is related to the Q-factor of the cavity as Q= $\omega_c/\Delta\omega_c$.

The enhancement of spontaneous rate inside a cavity is quantified by a parameter known as the Purcell factor F_p, which is given by [6, 49, 103]

$$F_p = \frac{\Gamma_c}{\Gamma_0} = \frac{3}{4\pi^2}\left(\frac{\lambda_c}{n_c}\right)^3 \frac{Q}{V}. \tag{2.11}$$

Here, Γ_c and Γ_0 represent the spontaneous emission rates inside a cavity and in free space, respectively. The spontaneous emission rate inside a cavity can be controlled by adjusting parameters, such as the Q-factor, mode volume (V), refractive index (n_c) or the mode wavelength (λ_c) of the cavity.

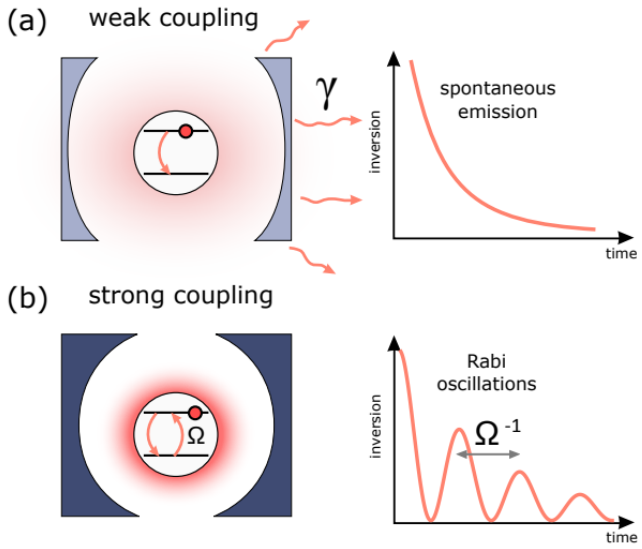

Figure 2.1: Schematic representation of weak (a) and strong (b) coupling between a optical cavity and emitter (two level system). Image adapted from [4].

2.1.2 Strong coupling regime

When an emitter undergoes emission inside a high Q-factor cavity, the emitted photon is reflected from cavity mirrors, leading to the accumulation of photons inside the cavity [40]. As a result, the probability of photon reabsorption by the emitter increases. If the rate of reabsorption exceeds the combined rate of photon leakage from the cavity and the rate of non-resonant emission, the system enters the regime of strong light-matter coupling,

giving rise to new quasiparticles called polaritons. In the regime of strong coupling, light and matter can not be treated independently, in contrast to the weak coupling discussed in section 2.1.1. A schematic representation of weak and strong coupling is shown in Fig. 2.1. Here, we present a quantum description of strong light-matter coupling based on theories described in Refs. [16, 40, 79].

According to Ref. [79], the linear Hamiltonian of a strongly coupled light-matter system, in second quantization, can be expressed as the sum of the Hamiltonians for the photon ($\hat{H}_{ph}$), the emitter ($\hat{H}_{em}$) and an interaction term ($\hat{H}_{int}$).

$$\begin{aligned}\hat{H} &= \hat{H}_{ph} + \hat{H}_{em} + \hat{H}_{int} \\ &= E_C \hat{a}^\dagger \hat{a} + E_X \hat{b}^\dagger \hat{b} + g\left(\hat{a}^\dagger \hat{b} + \hat{a}\hat{b}^\dagger\right),\end{aligned} \tag{2.12}$$

where E_C is the energy of the light field and E_X is the excitation energy of the emitter. The creation $\hat{a}/\hat{b}$ and annihilation $\hat{a}^\dagger/\hat{b}^\dagger$ operators are related to the photon/emitter. g is known as the coupling constant, which is defined as

$$g = \frac{\hbar\Omega_R}{2} \propto A\sqrt{\frac{Nf}{V}}. \tag{2.13}$$

Here, Ω_R is the Rabi frequency, representing the rate at which light and matter exchange energy. A is the strength of the cavity field, N is the number of emitters interacting with photons, f is the oscillator strength of the emitter and V is the mode volume of the cavity. For a system with one cavity photon and one emitter, the coupling can be described by a 2×2 matrix Hamiltonian as follows:

$$\hat{H}\begin{pmatrix} X_{k_\parallel} \\ C_{k_\parallel} \end{pmatrix} = \begin{pmatrix} E_C(k_\parallel) & g \\ g & E_X(k_\parallel) \end{pmatrix}\begin{pmatrix} X_{k_\parallel} \\ C_{k_\parallel} \end{pmatrix} = E\begin{pmatrix} X_{k_\parallel} \\ C_{k_\parallel} \end{pmatrix}. \tag{2.14}$$

The diagonalization of the above matrix Hamiltonian gives information about its eigenvalues, which represent the polariton energies and in-plane dispersion ($k_\parallel$).

$$E_{UP,LP}(k_\parallel) = \frac{1}{2}\left[E_C(k_\parallel) + E_X(k_\parallel) \pm \sqrt{4g^2 + \left\{E_X(k_\parallel) - E_C(k_\parallel)\right\}^2}\right], \tag{2.15}$$

where $E_X(k_\parallel) - E_C(k_\parallel) = \Delta E(k_\parallel)$ is the detuning of cavity photon energy from emitter energy. The eigenvectors of this matrix which represent the Hopfield coefficients are given by

$$\left|X_{k_\parallel}\right|^2 = \frac{1}{2}\left(1 + \frac{\Delta E(k_\parallel)}{\sqrt{\Delta E(k_\parallel)^2 + 4g^2}}\right). \tag{2.16}$$

$$\left|C_{k_\parallel}\right|^2 = \frac{1}{2}\left(1 - \frac{\Delta E(k_\parallel)}{\sqrt{\Delta E(k_\parallel)^2 + 4g^2}}\right), \tag{2.17}$$

The modulus squared of the amplitudes $\left|X_{k_\parallel}\right|^2$ and $\left|C_{k_\parallel}\right|^2$ represent the emitter and photon fraction in both lower and upper polariton branches, and $\left|X_{k_\parallel}\right|^2 + \left|C_{k_\parallel}\right|^2 = 1$. The dispersion curve of both upper and lower polaritons, and the corresponding Hopfield coefficients are schematically shown in Fig. 2.2.

Now, considering the finite lifetime of photons inside the cavity and the emitter lifetime, the eigenenergy is modified as [16]

$$\begin{aligned} E_{UP,LP}(k_\parallel) = \frac{1}{2}\Big[&E_C(k_\parallel) + E_X(k_\parallel) + i(\gamma_C + \gamma_X) \\ &\pm \sqrt{4g^2 + \left\{E_X(k_\parallel) - E_C(k_\parallel) + i(\gamma_C - \gamma_X)\right\}^2}\Big] \end{aligned} \tag{2.18}$$

Here, γ_C and γ_X account for the loss rate of photons through cavity mirrors and the damping rate of the emitter, respectively. When the cavity photon energy matches the emitter energy, i.e. $\Delta E(k_\parallel) = 0$, the modified Rabi splitting is given by

$$\hbar\Omega_R = \sqrt{4g^2 - (\gamma_C - \gamma_X)^2} \tag{2.19}$$

Thus, a splitting is only possible when the coupling constant is larger than half of the difference between the loss rate of cavity photons and the emitter damping rate, i.e.

$$g > \frac{\gamma_C - \gamma_X}{2} \tag{2.20}$$

The above condition must be satisfied to reach the strong light-matter coupling, otherwise the emitter-cavity system is in the weak coupling regime.

2.2 Structure of Cu_2O crystals

Cu_2O is a red-coloured solid (Fig. 2.3(d)), generally found in copper mines worldwide. It can also be fabricated in laboratories [10,60,62,64], albeit the quality of the natural crystal is so far unbeatable. The unit cell of Cu_2O consists of 4 copper and 2 oxygen atoms. The

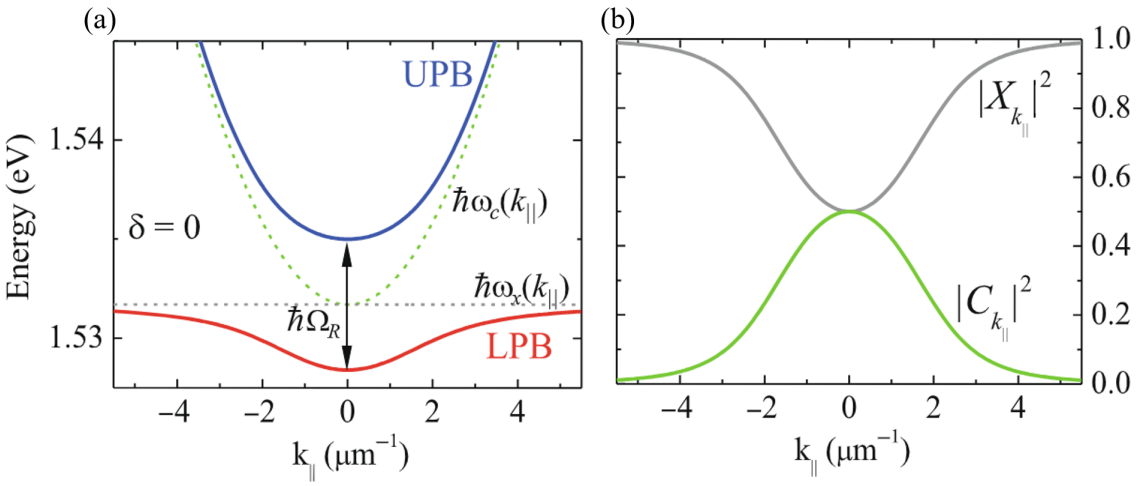

Figure 2.2: (a) Dispersion curves of bare exciton (grey dots) and cavity mode (green dots) along with the dispersion of upper (blue) and lower (red) polariton branches. (b) Related Hopfield coefficients, where $\left|X_{k_{||}}\right|^2 + \left|C_{k_{||}}\right|^2 = 1$. Image adapted from [7].

oxygen atoms form a body-centred cubic (bcc) lattice, while the copper atoms are arranged in a face-centred cubic (fcc) lattice. The bcc lattice is shifted a quarter of the diagonal inside the fcc. The entire structure, as shown in Fig. 2.3(a), is centrosymmetric and can be described based on the symmetry operations of the O_h point group. The lattice constant (a) is 4.26 $\AA$ [74]. Furthermore, the presence of 6 ions in a unit cell results in a total of 3 acoustic and 15 optical phonon branches.

2.2.1 Band structure

Cu_2O is a direct band semiconductor whose optical properties stem from the structure of both the valence and conduction bands at the Γ point (i.e. at K= 0). In the past, several attempts have been made to calculate the band structure, Refs. [13,81,83]. Here, we briefly report the band dispersion calculated by [21] within the framework of density functional theory. The corresponding typical electronic band structure of Cu_2O is shown in Fig. 2.4(a) and (b) as a reference. In this subsection, we focus on explaining the band structure and its symmetry in detail. We use group theory and adopt the notation used in the book by [17] to represent the used operators, electronic bands and excitonic states. Moreover, since Cu_2O has a centrosymmetric crystal structure, parity is a good quantum number. Therefore, positive and negative parity under inversion is indicated using upper indices + and -.

Due to the crystal field (reduced symmetry in the crystal), the fivefold degenerate 3d orbital of the copper atom splits into two bands: the upper Γ_5^+ and the lower Γ_3^+. Similarly, the 4s and 4p orbitals of copper can be represented by Γ_1^+ and Γ_3^- in the crystal field,

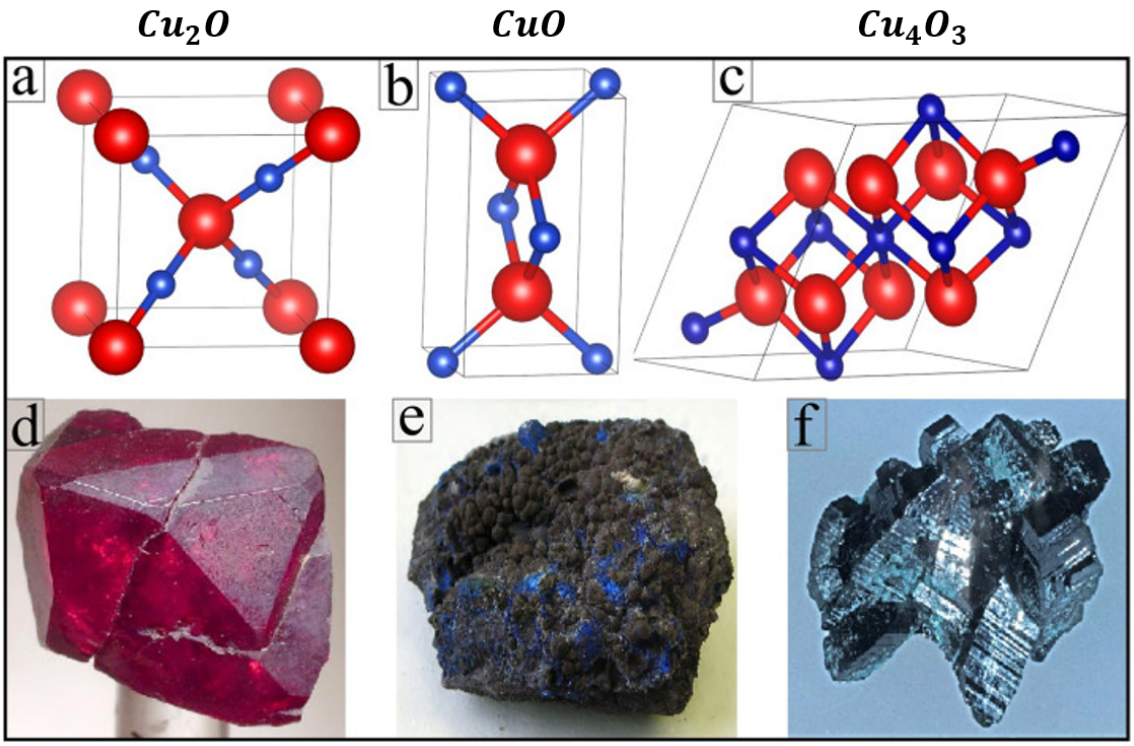

Figure 2.3: A comparison of crystal structure: (a) Cu_2O , (b) CuO and (c) Cu_4O_3 (collected from [70]). Blue dots represent copper atoms while red dots are oxygen atoms. Respective images of the crystals are given in the bottom panels (d), (e) and (f).

respectively [81]. These two orbitals form conduction bands. A schematic of the splitting of orbitals and their representations are shown in Fig. 2.4(a).

Furthermore, spin-orbit coupling plays an important role in the further splitting of orbitals. Γ_5^+ splits into Γ_7^+ and Γ_8^+, forming the uppermost and second uppermost valence bands, respectively. The two bands are separated by 131 meV [87]. It should be noted that the separation value varies across literatures: [21] reports 127.3 meV while [105] found 133.8 meV. Here, the symmetries Γ_7^+ and Γ_8^+ are calculated by multiplying Γ_5^+ with Γ_6^+, where the latter ones represents the spin in the O_h symmetry group. Moreover, according to [21], the deviation of the shape of the uppermost valance band from the parabolic dispersion is due to the spin-orbit coupling. Similarly, under the influence of spin-orbit coupling, the symmetries of the two conduction bands (Γ_1^+ and Γ_3^-) transform into Γ_6^+ and Γ_8^-, as shown in Fig. 2.4(a).

The optical transitions and exciton formation can occur between these energy bands when a light field with suitable energy impinges on the sample. In principle, there are a total of four series of band-to-band transitions, as shown in Fig. 2.4(b). The uppermost valence band and the low-lying conduction band give rise to the so-called yellow series

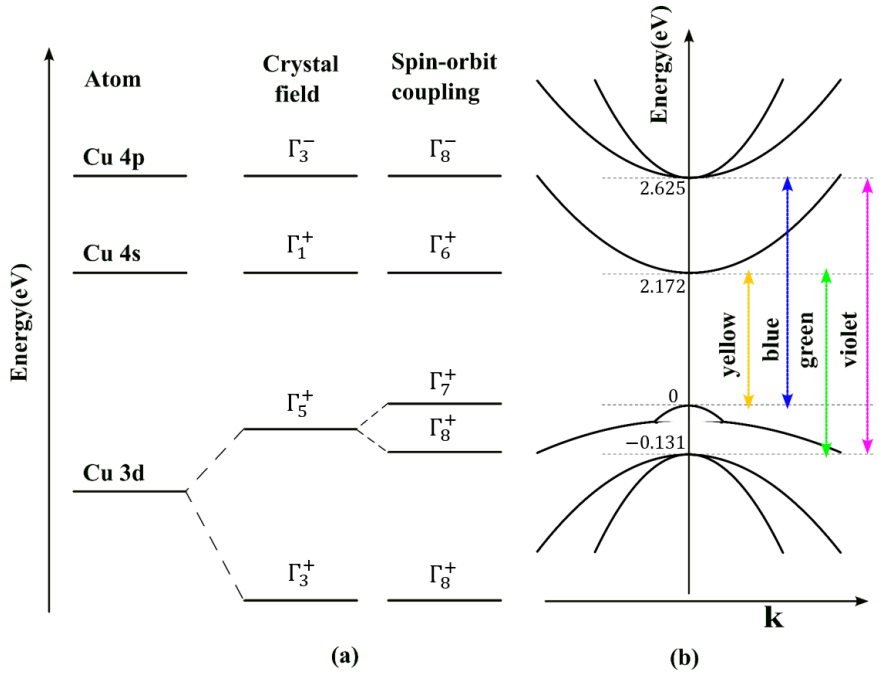

Figure 2.4: (a) Atomic orbitals split due to reduced symmetry (O_h) of crystal environment and spin-orbit coupling. (b) Dispersion curve and interband transitions.

with an electronic bandgap of E_g^y =2.17208 eV [51]. Similarly, the transition between the second-highest valence band and the lowest conduction band constitutes a green series with a bandgap E_g^g =2.3023 eV [43]. The transitions from the uppermost and second uppermost valence bands to the upper conduction band lead to the blue and violet series with bandgaps E_g^b =2.6336 eV and E_g^v =2.756 eV [99], respectively.

2.3 Theory of Excitons

In general, when an electron is excited from the valence to the conduction band in a solid, an electron vacancy is created in the valence band. This vacancy, which is positively charged, is known as a 'hole'. Due to their opposite charges, electrons and holes are attracted by Coulomb forces, forming a Coulomb-correlated bound complex called an 'exciton'. Essentially, an exciton is a quasi-particle, meaning it is a collective excitation of two individual particles (electron and hole) and has characteristics of an actual particle. Primarily, based on their sizes, excitons are of two types: Frenkel exciton and Wannier-Mott exciton [49,54].

Frenkel excitons have smaller wave envelope functions, typically constrained within a single or few crystal unit cells, and thus have larger binding energies (in order of 0.1-1 eV). On the other hand, Wannier-Mott excitons have larger envelope functions extending

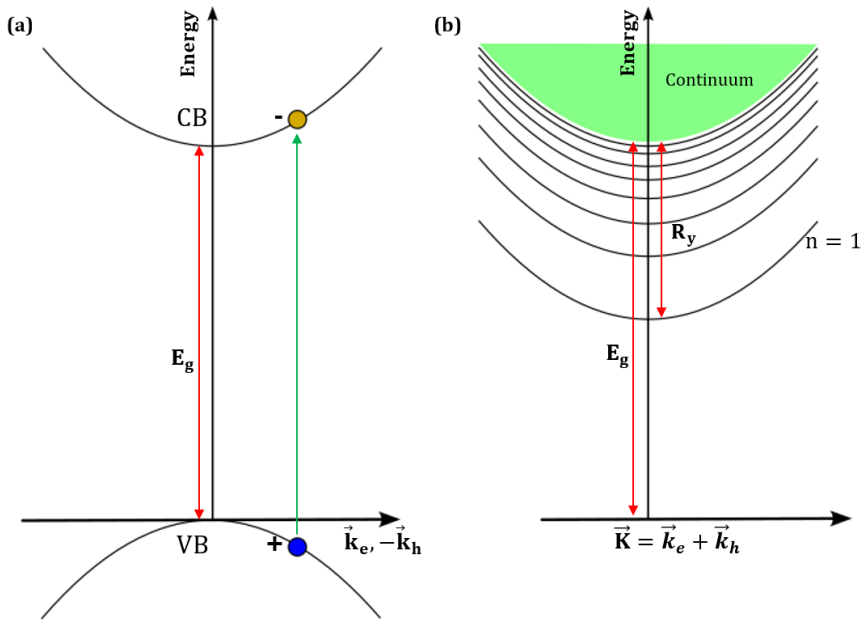

Figure 2.5: (a) Dispersion curve of an individual electron and hole. (b) Dispersion curve of exciton. The x-axis shows the collective momentum of the electron and hole. Distinct excitonic lines are visible below the bandgap energy.

beyond tens of lattice constants and have smaller binding energies (typically a few to hundreds of meV). Frenkel excitons are mostly found in alkali halide and organic materials, while Wannier-Mott excitons are found in semiconductors. Excitons in Cu_2O are of the Wannier-Mott type. Here, we briefly explain the concept of excitons under the effective-mass approximation, i.e. the transition of electron occurs close to the Γ point (k= 0). In this condition, both electron and hole experience a parabolic dispersion in momentum. Thus, they can be treated as free particles, albeit with effective masses m_e and m_h which are independent of momentum (k). The motion of their bound complex, i.e. the exciton, can be described using the following Hamiltonian [54]:

$$H_0 = E_g + \frac{\hbar^2}{2M_{eh}} \bigtriangledown_R^2 + \frac{p_{eh}^2}{2\mu_{eh}} + V(r). \tag{2.21}$$

Here, E_g denotes the bandgap energy. The second term represents the kinetic energy of the centre of mass, where $M_{eh} = m_e + m_h$ is the total translational mass, and R_{eh} is the position of the centre of mass. R_{eh} is given as

$$R_{eh} = \frac{m_e r_e + m_h r_h}{m_e + m_h}, \tag{2.22}$$

where r_e and r_h are the positions of the electron and hole, respectively. The third term in

Eq. 2.21 explains the relative motion of the electron and hole with momentum p_{eh} and the reduced mass μ_{eh}, which is given by

$$\mu_{eh} = \frac{m_e m_h}{m_e + m_h}. \tag{2.23}$$

The fourth term, $V(r)$, is the Coulomb potential energy, which is given by

$$V(r) = -\frac{e^2}{4\pi\varepsilon_0\varepsilon_r r}, \tag{2.24}$$

where e is the elemental unit charge, ε_0 is vacuum permittivity, and ε_r is the relative permittivity of the material medium. The distance between electron and hole is denoted as $r = |r| = |r_e - r_h|$. The dispersion energy corresponding to the Hamiltonian above is as follows:

$$E_{ex}(n,K) = E_g - \frac{R_y^{ex}}{n^2} + \frac{\hbar^2 K^2}{2M}, \tag{2.25}$$

where n is the principal quantum number and the exciton Rydberg energy (R_y) is given by

$$R_y^{ex} = R_y^H \frac{\mu}{m_0}\frac{1}{\varepsilon_r^2}. \tag{2.26}$$

Here, m_0 is the mass of the free electron, and $R_y^H = 13.6$ eV is the Rydberg energy of the hydrogen atom. For the yellow exciton series in Cu_2O , the R_y^{ex} is 92 meV. As a reference, Table 2.1 compares the binding energy of the exciton in different materials. Moreover, the third term in Eq. 2.25 represents the kinetic energy of the centre of mass with the wave vector of the exciton being defined as $\vec{K} = \vec{k_e} + \vec{k_h}$.

Akin to the Eq. 2.26, the Bohr radius of an exciton is related to the hydrogen atom as follows:

$$a_B^{ex} = \frac{m_0}{\mu}\varepsilon_r a_B^H, \tag{2.27}$$

where $a_B^H = 0.53$ Å and a_B^{ex} = 1.11 nm. The values of R_y^{ex} and a_B^{ex} given here are applicable for exciton states $n \geq 2$. Similarly, the radius of the exciton increases with the principal quantum number n

$$\langle r_{n,l} \rangle = \frac{a_B^{ex}}{2}\left[3n^2 - l(l+1)\right], \tag{2.28}$$

l is the angular momentum quantum number. For example, for the Rydberg exciton state $n = 25$, the radius reaches up to ~ 1 μm.

The wave function of an exciton can be defined as the product of the individual wave functions of a hole $\Phi_h(r_h)$ in the valence band, an electron $\Phi_e(r_e)$ in the conduction band

Material	E_g[eV]	R_y[meV]
H, alkali atoms	0	13600
TMD monolayers	1-2.1	400-700
CuCl	3.397	190
Cu_2O	2.172	92
ZnO	3.37	59
CdS	2.55	28
ZnSe	2.82	19
Si	1.12	14.3
AlAs	3.13	10
GaAs	1.519	4.2
Ge	0.89	2.1-5.1

Table 2.1: Comparison of exciton binding energy for alkali atoms and different materials, measured at temperature 4.2 K. The values are collected from [51, 76, 85, 92, 100, 106, 110] .

and the envelope function $\Phi^{env}_{nlm}(r_e - r_h)$

$$\Phi(K,n,l,m) = \Omega^{-1/2} e^{iKR} \Phi_e(r_e)\Phi_h(r_h)\Phi^{env}_{nlm}(r_e - r_h). \tag{2.29}$$

Here, $\Omega^{-1/2}$ is the normalization factor [54]. The movement of the centre of mass is accommodated using the plane wave function e^{iKR}. The relative motion of the electron and hole is described using the envelop function $\Phi^{env}_{nlm}(r_e - r_h)$.

2.3.1 Excitonic absorption in Cu_2O

In this section, we present an overview of the absorption spectrum of the yellow exciton series in Cu_2O . The spectrum is acquired by scanning laser energy from 2.0284 to 2.1978 eV. The sample used here is of high quality with a minimal number of impurities, enabling us to observe excitons with principal quantum numbers up to $n = 22$. Details of the experimental setup employed are given later in section 4.1 of Chapter 3.

Figure 2.6 illustrates the absorption spectrum shown by the blue curve. The spectrum starts with a quadrupole-allowed $1S$-ortho exciton resonance, which exhibits a Lorentzian shape. A closer examination of the resonance reveals its splitting into two components, as shown in inset I. The two resonances are $\sim$6 μeV apart, with individual linewidths $\sim$ 4 μeV and 2 μeV. The reason for splitting is attributed to the K-dependent exchange interaction, extensively investigated by G. Dashbach [14, 15, 23]. Additionally, the deviation of the valance band structure (see Fig. 2.4) from a parabolic shape contributes to this splitting [31]. This effect is particularly noticeable in the case of $1S$ exciton due to its smaller size

and larger momentum spread ($\hbar K$). On the other hand, strain could potentially cause such splitting. However, we use both strain-free sample holders and samples, ruling out strain as a factor in this scenario.

The second inset (inset II) plots the absorption of the weak quadrupole-allowed $2S$ exciton of the yellow series and the $1S$ exciton of the green series at energies $E_{2S_y} = 2.1375$ eV and $E_{1S_g} = 2.15439$ eV, respectively. The spectral positions of both exciton resonances match the findings reported by Mund et al. [69].

The continuous phonon background of the Γ_3^- phonon branch begins at an energy $E_{ph}^{\Gamma_3^-} = 13.5$ meV higher than that of the $1S$ yellow exciton resonance, as shown in the black curve of Fig. 2.6(a). The absorption coefficient (α) shows a square-root dependence on energy, i.e. $\alpha \propto \left[E - (E_{1S} + E_{ph}^{\Gamma_3^-})\right]^{1/2}$. Additionally, we observed that there are a total of four phonon branches that contribute to the continuous absorption background. The starting energy of these phonon branches is indicated by vertical dashed lines. The second phonon branch (Γ_4^-), which couples to the $1S$-ortho exciton, begins at 82.1 meV higher energy ($E_{1S}^{\Gamma_4^-}$) compared to the $1S$ exciton. Similarly, the Γ_3^- phonon couples to the $2S$ yellow and $1S$ green exciton, contributing to the background absorption which is depicted in brown and green colours, respectively.

In addition to the continuum phonon background, the impact of impurities and vacancies is evident in terms of an exponential increase in absorption starting around $n = 10$ and ending near the energy $\tilde{E}_g = 2.171915$ eV, as indicated by the orange curve. At $\tilde{E}_g$, the exciton resonances smear into the continuum. Essentially, the micro-electric fields originating from charged impurities is inhomogeneously distributed across the crystal, leading to the ionization of high-lying RE and resulting in an exponentially increasing absorption continuum near the bandgap. Further details about this tail-like feature and its genesis can be found in Refs. [18, 58]. The exponential tail can be described by using an Urbach-tail-like function

$$\alpha_U = C_U e^{(E-\tilde{E}_g)/E_U}. \tag{2.30}$$

Here, C_U is the amplitude and E_U is the Urbach energy which dictates the width. For the data shown in Fig. 2.6, E_U is found to be 170 μeV.

When $E > \tilde{E}_g$, the absorption can be described using as follows [88]:

$$\alpha_{con} = C_{con} \cdot \frac{1}{E}\left(E - \tilde{E}_g\right)^{3/2} \cdot \frac{\bar{\gamma} e^{\bar{\gamma}}}{\sinh \bar{\gamma}} \left(1 + \frac{\bar{\gamma}^2}{\pi^2}\right). \tag{2.31}$$

Here, C_{con} denotes the amplitude and the absorption increases as $\left(E - \tilde{E}_g\right)^{3/2}$, as detailed in Ref [19]. The last term represents the Sommerfeld enhancement factor, where $\bar{\gamma} =$

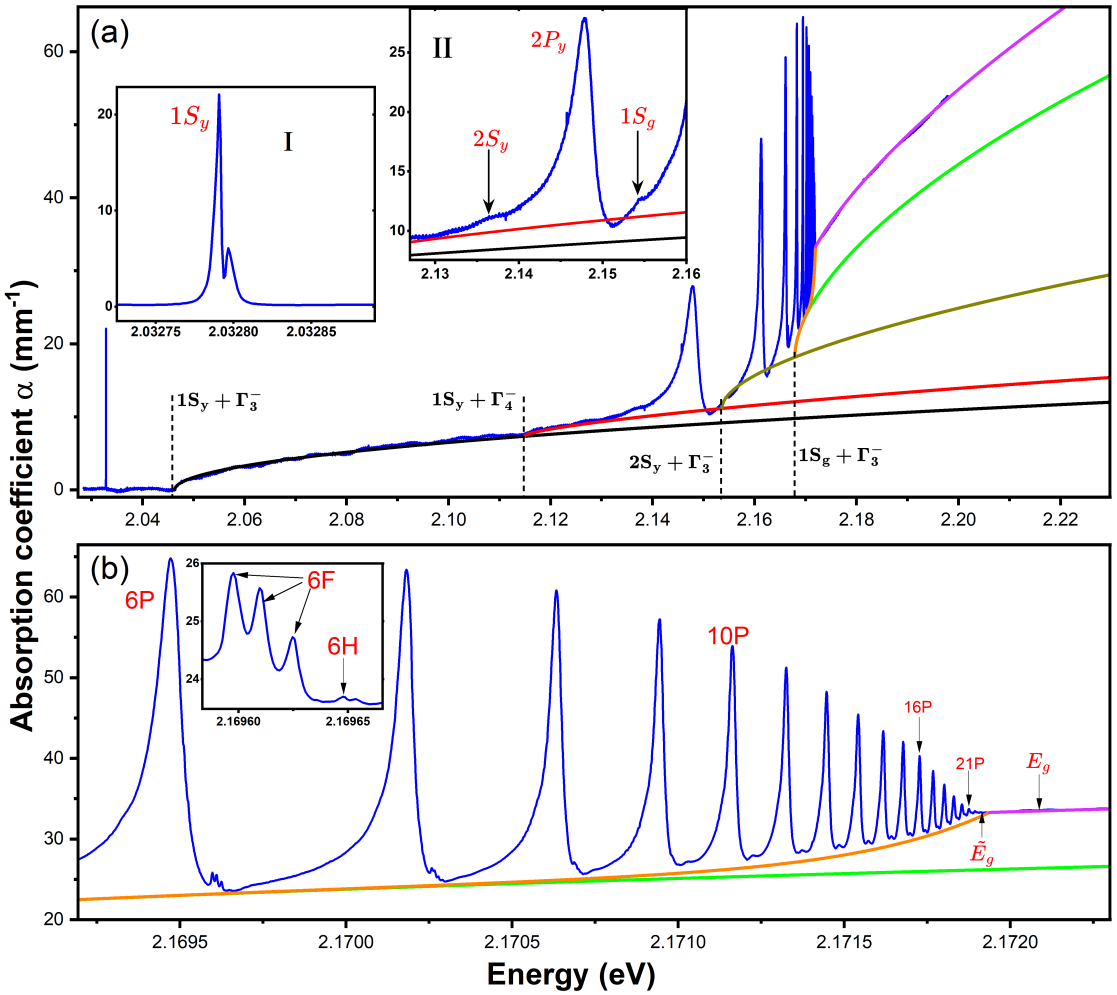

Figure 2.6: (a) Blue curve: linear absorption spectrum of Cu_2O in the spectral range of yellow excitons, obtained by scanning laser energy from 2.0284 to 2.1978 eV. The laser power is 1μW. Distinct exciton resonances are visible as asymmetric Lorentzian lines, which are laid over continuum phonon absorption backgrounds as shown in black, red, brown and green colours. The asymmetric nature of lines arises due to the quantum interference of two oscillators: a symmetric exciton line and a phonon continuum. The vertical dashed lines represent the starting energy of different phonon backgrounds. (b) High-n Rydberg states are enlarged. S, F and H states are shown using zoomed insets. The end of the exciton series is indicated using $\tilde{E}_g$, which is 172 μeV below the normal band gap E_g. The data used here is adapted from [31]

$\left(\frac{\pi^2 R_y}{E-\tilde{E}_g}\right)^{1/2}$, accounting for the increase in oscillator strength near the band edge due to the Coulomb interaction between free charge carriers.

In general, the overall background beneath the exciton resonances is given by

$$\alpha_{bkg} = \alpha_{1S_y}^{\Gamma_3^-} + \alpha_{1S_y}^{\Gamma_4^-} + \alpha_{2S_y}^{\Gamma_3^-} + \alpha_{1S_g}^{\Gamma_3^-} + \alpha_U + \alpha_{con}. \tag{2.32}$$

The parameters used to fit the background absorption are summarized in the table 2.2

Parameter	Value	Unit
$C_{1S_y}^{\Gamma_3^-}$	28	$(mm\sqrt{eV})^{-1}$
$C_{1S_y}^{\Gamma_4^-}$	10	$(mm\sqrt{eV})^{-1}$
$C_{2S_y}^{\Gamma_3^-}$	51	$(mm\sqrt{eV})^{-1}$
$C_{1S_g}^{\Gamma_3^-}$	72.8	$(mm\sqrt{eV})^{-1}$
C_U	5.5	mm^{-1}
E_U	170	μeV
$\tilde{E}_g$	2.1719050	eV
C_{con}	105	mm^{-1}

Table 2.2: Parameters used to describe the total background absorption in Fig. 2.6, adapted from [31].

2.4 Exciton-exciton interaction

Ever since the discovery of high-n RE in Cu_2O by Kazimierczuk et al. [51], it has been observed that the exciton absorption lines bleach with increasing excitation laser power, which was attributed to the exciton-exciton interaction, particularly Rydberg blockade among RE. Additionally, Heckötter et al. [39] came up with a detailed study of the Rydberg blockade mechanism among excitons. In this section, a brief overview of exciton-exciton interaction and Rydberg blockade is provided.

Rydberg excitons exhibit a substantial dipole moment (μ) owing to their large electron-hole pair separation. The dipole moment grows as the square of the principal quantum number, i.e. $\mu \propto n^2$. Therefore, RE are expected to demonstrate strong dipole-dipole interaction, which is modelled as follows. Consider two excitons, A and B, with principal quantum numbers n and n', separated by a distance R, where $R = \left|\vec{R}\right| = \left|\vec{R_{n'}} - \vec{R_n}\right|$ (see Fig. 2.7). The potential energy corresponding to the dipole-dipole interaction is given by

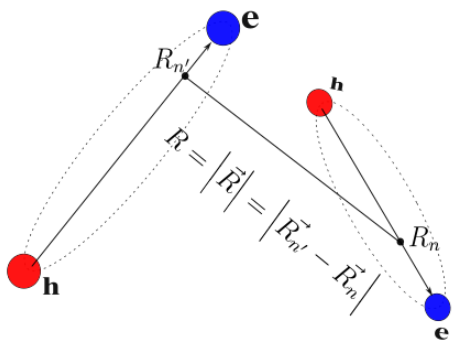

Figure 2.7: Sketch of two excitons. $R_{n'}$ and R_n are the center of mass coordinates of both excitons.

$$V_{dd} = \frac{1}{4\pi\varepsilon_0\varepsilon_r}\frac{\mu_n\mu_{n'} - 3(\mu_n\cdot\hat{R})(\mu_{n'}\cdot\hat{R})}{R^3}. \tag{2.33}$$

Here, $\hat{R} = \frac{\vec{R}}{|\vec{R}|}$. μ_n and $\mu_{n'}$ are the dipole moments of exciton A and B, respectively. The unperturbed paired state of both excitons, without any interaction, can be represented as $|n,\, n'\rangle$ with an unperturbed energy $E_{n,n'} = E_n + E_{n'}$.

When the two excitons interact with each other, this introduces a coupling to other pair states $|m,m'\rangle$ with energy $E_{m,m'}$, where m and m' are the principal quantum numbers of the individual virtual states. In the case of non-degenerate pair states, according to second-order perturbation theory, the energy correction to the pair state $|n,n'\rangle$ is given by

$$\Delta E_{vdW} = \sum_{m,m'}\frac{|\langle n,n'|\, V_{dd}\,|m,m'\rangle|^2}{E_{n,n'} - E_{m,m'}} = \pm\frac{C_6}{R^6}, \tag{2.34}$$

where $E_{n,n'} - E_{m,m'}$ is the energy difference between pair states, often referred to as the Förster defect. The summation consists of all the pair states $|m,m'\rangle$ that couple to $|n,n'\rangle$. The term $\frac{1}{R^6}$ stems from the dependence of energy shift (ΔE_{vdW}) on the square of V_{dd}, i.e. $\Delta E_{vdW} \propto |V_{dd}|^2$. According to [31, 39, 108], the C_6 coefficient can be expressed as

$$C_6(n,n') \propto \frac{\mu_{n,m}^2\mu_{n',m'}^2}{\Delta_{n,m} + \Delta_{n',m'}}. \tag{2.35}$$

Here, $\Delta_{n,m}$ and $\Delta_{n',m'}$ represent the energy separations between the states $n(n')$ and their coupled states $m(m')$, where $\Delta_{n,m}$ scales as n^{-3}. The dipole matrix elements $\mu_{n,m} = \langle n|\,\mu_{n,m}\,|m\rangle$ and $\mu_{n',m'} = \langle n'|\,\mu_{n',m'}\,|m'\rangle$ in the numerator are proportional to n^2 and n'^2, respectively, considering $n \approx m$ ($n' \approx m'$). Therefore, the expression above Eq. 2.35 reduces to

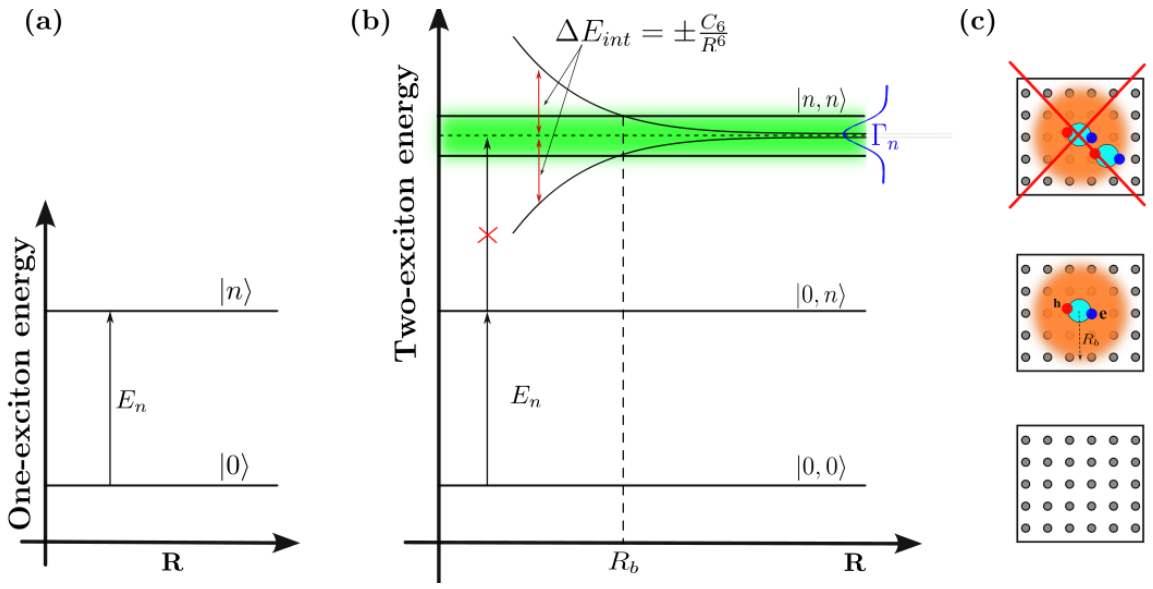

Figure 2.8: (a) Sketch of the energy levels of an exciton. (b) Sketch of the energy levels of two excitons. One exciton in a Rydberg state prevents the excitation of a second exciton to a Rydberg state within its blockade radius R_b. (c) Schematic presentation of the Rydberg blockade process.

$$C_6(n,n') \propto \begin{cases} n^7\,(n')^4 & \text{for } n \ll n' \\ n^4\,(n')^7 & \text{for } n \gg n' \end{cases} \tag{2.36}$$

When $n \ll n'$, the first term in denominator ($\Delta_{n,m} \propto n^{-3}$) dominates, whereas in the scenario of $n \gg n'$, the second term, i.e. $\Delta_{n',m'} \propto n'^{-3}$ becomes more prominent. Furthermore, when $n \neq n'$, i.e. two lasers excite different Rydberg exciton states, the interaction is termed asymmetric or non-degenerate Rydberg blockade. When both lasers excite the same Rydberg exciton states, i.e. $n = n'$, the interaction is called symmetric Rydberg blockade and the corresponding C_6 coefficient is given by

$$C_6(n) \propto n^{11}. \tag{2.37}$$

On the other hand, when the pair states $E_{n,n'}$ and $E_{m,m'}$ are degenerate, only the first-order corrections to the energy contribute. This is called resonant dipole-dipole or Förster interaction.

$$\Delta E_F = \pm\langle n,n'|\,V_{dd}\,|m,m'\rangle = \pm\frac{C_3}{R^3} \tag{2.38}$$

For both scenarios of asymmetric and symmetric Förster interaction, the coefficient C_3 is given as follows

$$C_3(n,n') \propto n^2 \left(n'\right)^2 \text{ ,when } n \neq n' \tag{2.39}$$

and

$$C_3(n) \propto n^4 \text{ ,when } n = n'. \tag{2.40}$$

As a reference, the Rydberg blockade mechanism is schematically illustrated in Fig. 2.8. Unlike the atomic system where initial pair states are described by the ground states of the interacting atoms, here, in the case of excitons, initial ground pair states are formed by the empty crystals which are denoted as $|0,0\rangle$. When only one exciton is subjected to a Rydberg excitation, the corresponding pair state is denoted as $|0,n\rangle$, and its energy is $E_{0,n} = E_n$ as marked using a horizontal line in the middle. However, the energy of the doubly excited pair state $|n,n\rangle$ is modified due to the exciton-exciton interaction. Instead of a simple sum of the energies of both Rydberg excitons, i.e. $2E_n$ (upper horizontal dashed line), total energy contains an additional interaction term ΔE_{int}.

In principle, the additional energy can stem from either van der Waals or Förster interaction depending upon the degeneracy of the pair state and the nature of the excitonic dipole moment. The sign of ΔE_{int} indicates the character of the force between excitons. If it is positive ($\Delta E_{int} > 0$), the force is repulsive, while it is attractive for negative ΔE_{int}. If the shift ΔE_{int} is larger than the linewidth of the excitonic resonance (i.e. $\Delta E_{int} > \Gamma_n$), it is no longer possible to excite the pair state using a single narrow linewidth laser. Furthermore, as mentioned earlier in Eqs. 2.34 and 2.38, ΔE_{int} depends on the relative distance between RE. Thus, there exists a critical radius (R_b) or in general a volume beyond which pair excitation of RE is possible and below which a pair excitation is not possible. This critical volume is called the blockade volume (V_b) which is given by

$$V_b = \frac{4}{3}\pi R_b^3 = \begin{cases} \sqrt{\frac{C_6}{\Gamma_n}} & \text{, van der Waals interaction} \\ \frac{C_3}{\Gamma_n} & \text{, Förster interaction} \end{cases}. \tag{2.41}$$

2.5 Exciton-plasma interaction

In this section, the theory of the interaction between RE and an ultra-low density electron-hole plasma is briefly discussed. So far, two theories have been devised: firstly by Heckötter et al. [33] which is based on the Debye model, and secondly, by Stolz et al. [98] within the framework of quantum many-body theory. Here, we use latter to explain various experimental observations related to RE and a plasma.

Based on its properties, the plasma can be broadly classified into two categories: a non-degenerate and a degenerate plasma, where the degeneracy parameters is expressed

as $\rho_a \Lambda_a^3$. Here, ρ_a denotes the plasma density and $\Lambda_a = \sqrt{2\pi\hbar^2/(\mu_a k_B T)}$ represents the thermal de Broglie wavelength (with μ_a as the reduced mass of plasma particles). The plasma is considered as non-degenerate when $\rho_a \Lambda_a^3 \ll 1$, and as degenerate when $\rho_a \Lambda_a^3 \gg 1$. In our case, the plasma under consideration is non-degenerate.

In 1923, Debye and Hückel derived the fundamental interaction between charged particles surrounded by a plasma using a screened Coulomb potential

$$V_D(r) = \frac{1}{4\pi\varepsilon_0\varepsilon_r}\frac{e^{-\kappa_D r}}{r}, \tag{2.42}$$

where κ_D is the inverse Debye screening length given by

$$\kappa_D = \left(\frac{\rho e^2}{\varepsilon_0\varepsilon_r k_B T}\right)^{1/2}. \tag{2.43}$$

ρ represents the particle density, e denotes the fundamental charge unit, T represents the equilibrium plasma temperature, ε_r stands for the relative permittivity of the medium and k_B represents Boltzmann's constant.

The shift of the single-particle energy due to this screened interaction is given by

$$\Delta E_{sp} = -\frac{1}{2}\frac{e^2}{4\pi\varepsilon_0\varepsilon_r}\kappa_D. \tag{2.44}$$

2.5.1 Influence of plasma on excitons

To investigate the impact of an electron-hole plasma on the bound states of RE, we take advantage of pump-probe spectroscopy which is described in detail in chapter 3. The pump laser is fixed at an energy of 2.1 eV, which lays spectrally in the phonon background between 1S-ortho and 2P exciton resonances. Thus, the creation of 1S excitons is possible via simultaneous emission of a phonon. The 1S excitons either recombine radiatively or produce an e-h plasma through the non-linear Auger process. Simultaneously, a low-intensity probe laser (1 μW) is scanned across the Rydberg exciton resonances up to the band edge (E_g). The corresponding transmission of the probe laser is recorded using a photodiode. Figure 2.9 illustrates the typical absorption spectrum of RE at several pump laser powers.

The impact of the e-h plasma on excitons manifests through changes in several parameters. Each of these observations is discussed separately in the following and analytic expressions are given.

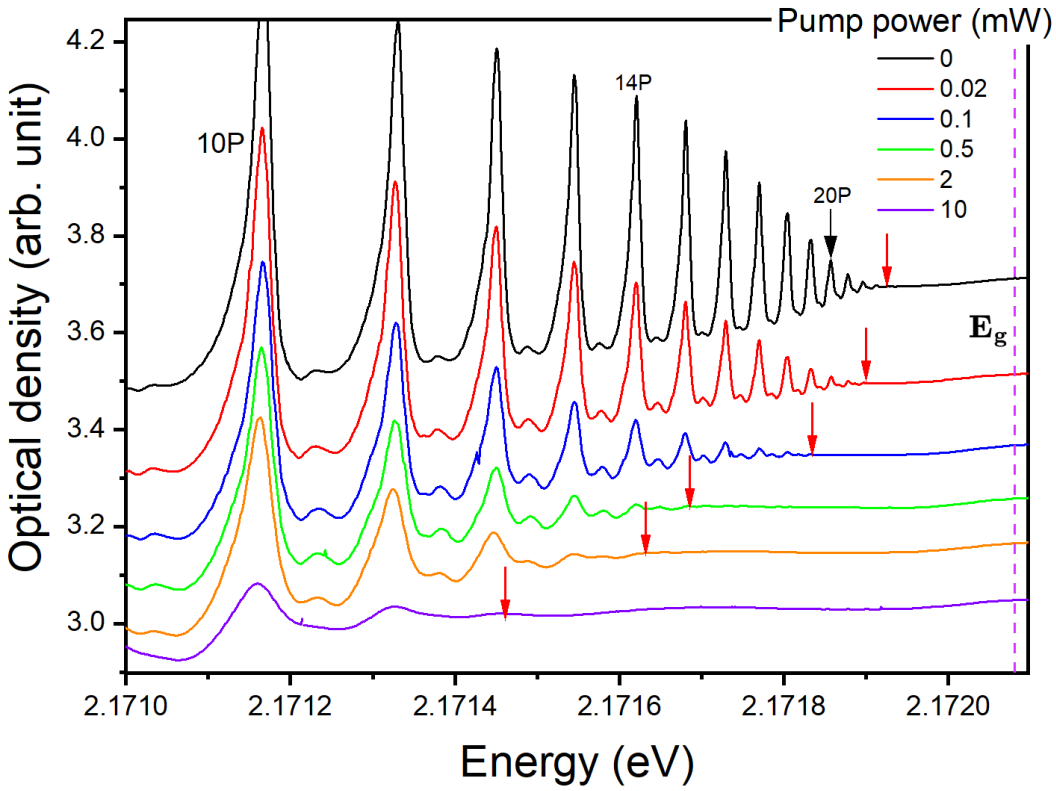

Figure 2.9: Absorption spectra of Rydberg excitons at several pump laser powers. Red arrows indicate the position of the shifted bandgap $\tilde{E}_g$.

Lowering of band edge

The primary and most significant effect of a plasma on RE is the lowering of the band edge. As a reference, the red vertical arrows in Fig. 2.9 indicate the position of the shifted band edge ($\tilde{E}_g$) at several pump laser powers. The shifted band edge is defined as $\tilde{E}_g = E_g + \Delta$, where Δ represents the amount of shift relative to the unperturbed band edge. Even at zero pump laser power, a noticeable shift of $\Delta_0 \approx -140$ μeV is observed. A potential reason is the ionization of high-lying RE caused by the inhomogeneous micro-field that originates from charged impurities [58]. Therefore, the total band edge shift consists of two components: a constant Δ_0 and a plasma dependent Δ_{eh}, given by $\Delta^2 = \Delta_0^2 + \Delta_{eh}^2$.

The plasma-induced band edge shift (Δ_{eh}) which depends on the plasma density (n_{eh}) and temperature (T_{eh}), can be estimated by using the theory developed by [90] as follows

$$\begin{aligned} \Delta_{eh}(n_{eh},\, T_{eh}) &= \sqrt{\Delta^2 - \Delta_0^2} \\ &= -692\ \mu\text{eV} \cdot (n_{eh} T_{eh})^{1/4} \left(\frac{\mu\text{m}^3}{K}\right)^{1/4}. \end{aligned} \tag{2.45}$$

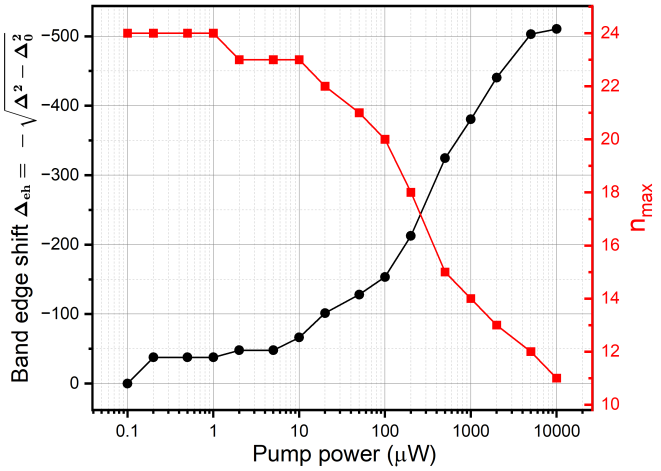

Figure 2.10: Black dots (left ordinate): band gap shift as a function of pump laser power. Red dots (right ordinate): principal quantum number of highest Rydberg exciton (n_{max}) observed.

Since Δ_{eh} can be estimated from the experimental data (shown in black dots of Fig. 2.10), it is evident from the Eq. 2.45 that the product $n_{eh} \cdot T_{eh}$ can be calculated, but not the individual values of n_{eh} and T_{eh}. The essential point to note is that Δ_{eh} also includes the effect of an increased density of charged impurities along with plasma at high pump powers.

Shift of binding energy

As discussed previously, in the presence of a plasma, the pure Coulomb potential that forms bound exciton states is screened. Thus, the formation of electron-hole pairs that constitute excitons has now to be described using the screened coulomb potential (Eq.2.42). This results in a change in the exciton's binding energy or in a shift in the spectral position of the exciton resonance, which is given by

$$\Delta E_{eh}(n, n_{eh}, T_{eh}) = -C_b n^4 n_{eh}(1 + b/T_{eh}^{1/4}). \tag{2.46}$$

Here, $C_b = 1.53 \times 10^{-2}$ μeV μm^3 and b = 0.32. The derivation of the equation above is given in [90, 98]. Moreover, using both Eqs. 2.45 and 2.46, it is possible to evaluate n_{eh} and T_{eh} independently.

Oscillator strength and linewidth of resonances

The total linewidth of an exciton surrounded by an e-h plasma is expressed as the sum of the following two parts.

$$\Gamma_{total}(n) = \Gamma_{phonon}(n) + \Gamma_{plasma}(n) \tag{2.47}$$

Here, Γ_{phonon} comprises phonon-related broadening of linewidth, which is proportional to $\frac{n^2-1}{n^5}$. On the other hand, the plasma-influenced linewidth exhibits a peculiar dependence on n, which is given by

$$\Gamma_{plasma} = C_{plasma}(n-1)^{3.3\pm0.2}, \tag{2.48}$$

where

$$C_{plasma} = 1.6\, n_{eh}/\sqrt{T_{eh}/K}\ \mu\text{eV}\ \mu\text{m}^3. \tag{2.49}$$

The prefactor C_{plasma} is obtained by fitting the absorption spectra (see Ref. [98]). The prefactor increases with an increase in the plasma density (n_{eh}) and drops with an increase in the plasma temperature (T_{eh}). Even though the many-body theory does not predict such a broadening effect [91], Stolz et al. [98] propose that the line broadening stems from the interaction of excitons with plasmons which are the elementary excitations of a plasma. This interaction leads to a scattering of RE, akin to the Frölich interaction (see Refs. [80, 97]).

On the other hand, the oscillator strength ($O(n)$) does not show any systematic variation with the pump laser powers [98]. In total, the change in absorption coefficient ($\Delta\alpha$) due to plasma at a particular exciton resonance is given by

$$\begin{aligned}\Delta\alpha &= \alpha(0) - \alpha(plasma) \\ &= \frac{2O(n)}{\pi}\left[\frac{1}{\Gamma_{phonon}(n)} - \frac{1}{\Gamma_{phonon}(n)+\Gamma_{plasma}(n)}\right].\end{aligned} \tag{2.50}$$

2.5.2 Evaluation of plasma density from pump power

Here, we estimate the density of an e-h plasma created by the pump laser using a rate equation model. The model was formulated by Prof. Heinrich Stolz and Dr. Dirk Semkat from the University of Rostock. Essentially, the model accounts for the time evolution of all processes and different species upon laser excitation.

According to the model, when a certain density of excitons (n_{Oex}) is created, these excitons finally relax to the 1S-ortho exciton state via phonon scattering at rate Γ_{relO1S}. Thus, the density of 1S-ortho excitons (n_{O1S}) is poised to increase. Moreover, 1S-ortho excitons can relax to the lowest lying 1S-para excitons (with density n_{P1S}) through phonon

emission at rate Γ_{OP} [45] or by a spin-flip process at a rate Γ_{SF} [45,50], or they can also non-radiatively decay with rate Γ_{O1Snr}. Additionally, with increasing densities n_{O1S} and n_{P1S}, a two-body Auger process emerges which scales quadratically with the exciton densities. In this process, two excitons collide with each other, whereby one exciton recombines and transfers its energy to the other. The second exciton became ionized and contributes to a plasma (with density n_{eh}) consisting of mobile free electrons and holes. The hot free electron-hole pairs created by the Auger processes may non-radiatively decay with rate Γ_{augnr} or recombine to form excitons with recombination rate Γ_{raug}. The corresponding rate equations are given below.

$$\begin{aligned}\frac{dn_{Oex}}{dt} = \eta_L G(t) - \Gamma_{relO1S} n_{Oex} - \Gamma_{O1Snr} n_{Oex} - \Gamma_{OP} n_{Oex} - \Gamma_{SF} n_{Oex} \\ -2a_{OO} n_{Oex}^2 - a_{OO} n_{Oex} n_{O1S} \\ -a_{OP} n_{Oex} n_{P1S} + \Gamma_{raug} n_{eh}^2\end{aligned} \tag{2.51}$$

$$\begin{aligned}\frac{dn_{O1S}}{dt} = \Gamma_{relO1S} n_{Oex} - \Gamma_{O1Snr} n_{O1S} - \Gamma_{OP} n_{O1S} - 2a_{OO} n_{O1S}^2 \\ -a_{OP} n_{O1S} n_{P1S} - a_{OO} n_{Oex} n_{O1S}\end{aligned} \tag{2.52}$$

$$\begin{aligned}\frac{dn_{P1S}}{dt} = \Gamma_{OP}(n_{O1S} + n_{Oex})\beta_D - \Gamma_{P1Snr} n_{P1S} - 2a_{PP} n_{P1S}^2 \\ -(a_{OP} n_{Oex} n_{P1S} + a_{OP} n_{O1S} n_{P1S})\beta_D\end{aligned} \tag{2.53}$$

$$\begin{aligned}\frac{dn_{eh}}{dt} = a_{PP} n_{P1S}^2 \beta_D + a_{OO} n_{O1S}^2 + a_{OO} n_{Oex} n_{O1S} + a_{OP} n_{Oex} n_{P1S} \beta_D \\ +a_{OP} n_{O1S} n_{P1S} \beta_D - \Gamma_{raug} n_{eh}^2 - \Gamma_{augnr} n_{eh}\end{aligned} \tag{2.54}$$

Here, $G(t)$ represents the temporal profile of the pump laser. The diffusion parameter is given by $\beta_D = \frac{w^2 \Gamma_{P1Snr}}{w^2 \Gamma_{P1Snr} + D}$, where w is the full width at half maximum (FWHM) of the cross-section of the pump beam. β_D is only relevant for $1S$-para excitons because of their long lifetime and hence, high rate of diffusivity ($D > 1000\ cm^2/s$ [98, 102]). The used rate constants in the above equations are given in table 2.11 and the notations used here are adapted from [98].

The equations above are too complex to solve analytically due to the involvement of multiple rate constants and parameters. However, given the short lifetime of $1S$-ortho and P excitons, one can approximate the whole system by considering only $1S$ para excitons and e-h plasma. The corresponding simplified rate equations are

Rate constant	Meaning	Value
Γ_{rOO1S} (*)	Relaxation rate into 1*S ortho*-exciton ground state	100/ns
Γ_{OP}	*Ortho-para* conversion rate	0.2/ns
a_{OO}	*Ortho-ortho* Auger rate	$5 \times 10^{-5}\,\mu m^3/ns$
a_{OP}	*Ortho-para* Auger rate	$a_{OO}/4$
a_{PP}	*Para-para* Auger rate	$4 \times 10^{-6}\,\mu m^3/ns$
Γ_{O1Snr} (*)	Nonradiative decay rate of *ortho*- and	1/500 ns
Γ_{P1Snr}	*para*-excitons	
Fraction of absorbed photons α_O	Absorption of *ortho*-excitons due to phonon process	0.2
Γ_{augnr} (*)	Nonradiative decay rate of hot Auger-generated electrons and holes	1/500 ns
Γ_{raug} (*)	Recombination rate of hot Auger-generated electron-hole pairs into excitons	$1\,\mu m^3/ns$

Figure 2.11: Rate constants used in the above equations are adapted from [98].

$$\frac{dn_{P1S}}{dt} = \alpha_S G(t) - \Gamma_{0P} n_{P1S} - 2a_{0PP} n_{P1S}^2 \tag{2.55}$$

and

$$\frac{dn_{eh}}{dt} = a_{0PP} n_{P1S}^2 - \Gamma_{0augnr} n_{eh} - \Gamma_{0raug} n_{eh}^2. \tag{2.56}$$

The stationary solutions of the coupled differential equations above are

$$n_{P1S}(P) = -\frac{\Gamma_{0P}}{4a_{0PP}} + \sqrt{\left(\frac{\Gamma_{0P}}{4a_{0PP}}\right)^2 + \frac{G(P)}{2a_{0PP}}\alpha_{eff}} \tag{2.57}$$

and

$$n_{eh}(P) = -\frac{\Gamma_{0augnr}}{2\Gamma_{0raug}} + \sqrt{\left(\frac{\Gamma_{0augnr}}{2\Gamma_{0raug}}\right)^2 + \frac{a_{0PP}}{\Gamma_{0raug}} n_{P1S}^2}. \tag{2.58}$$

The two solutions give insight into the densities of 1*S*-para excitons and the e-h plasma in the steady state.

Chapter 3

Interactions between Rydberg excitons and charged impurities

In this chapter, a detailed investigation of the interaction between Rydberg excitons and charged impurities inherent to the semiconductor crystal Cu_2O is discussed. Due to their larger size, Rydberg excitons (RE), analogous to the Rydberg atoms of atomic physics, possess a much stronger dipole moment compared to excitons in the ground state (i.e. 1*S*-ortho). Therefore, RE exhibit a large polarizability (α), which scales as the seventh power with the principal quantum number (i.e. $\alpha \propto n^7$) [35]. This peculiar characteristic of RE makes them extremely sensitive to the perturbation caused by the surrounding external fields. Indeed, a small density of charged impurities on the order of 0.001 μm^{-3}, which creates an electric field and thereby induce a Stark effect, can ionize high-n RE resonances. Thus, charged impurities and defects are primarily responsible for the limit of the highest observed states [37]. Kruger et al. [58] describe how the highest observed Rydberg state changes as a function of the density of charged impurities in the material Cu_2O . The charged impurities broaden the linewidth of odd parity *P*-states and reduce their oscillator strength by redistributing it to the neighbouring optically inaccessible dark-even parity states. As a result, for high-n states, a deviation of excitonic parameters from theoretical predictions is observed. The scaling of oscillator strength and linewidth does not follow the n^{-3} rule with the principal quantum number, as reported in Refs. [37, 51]. Instead, the linewidths exhibit an inhomogeneous broadening, and the oscillator strengths drop drastically in the high-n regime.

Thus, the challenging part is to get a pristine crystal devoid of charged impurities and defects. Here, in section 3.1, we describe an experimental technique to reduce the density of charged impurities by exciting a low density of RE using an additional pump laser. We refer to this process as the "purification" of the crystal. Even though the ideal scaling

laws (i.e. O_n, $\Gamma_n \propto n^{-3}$) for the linewidth and oscillator strength are not fully achieved, a considerable amount of improvement is observed. Moreover, to provide additional evidence of purification, we collect the photoluminescence (PL) signal of impurity sites by applying the settings discussed in section 3.2. The PL signals from all impurity sites show a drop with the excitation of a small density of high-n excitons. In section 3.3, to further expand the idea of neutralization of the electric field, we apply a uniform external electric field and demonstrate that RE, in principle, can cancel out an even stronger electric field by oppositely aligning to it. A part of this chapter is published in Heckötter et al. [38].

3.1 Neutralization of charged impurities

In this section, we demonstrate the enhancement of excitonic absorption in Cu_2O, which results from the reduction of charged impurities and defects. The following subsections provide details of the technique utilized and the corresponding observations, such as the change of different parameters, conditions for optimum enhancement of absorption, etc.

3.1.1 Experimental setup

A two-colour pump-probe technique is employed using two continuous-wave (CW), tunable, and narrow linewidth (10 neV) dye lasers (Sirah Matisse DS). The schematic diagram of the experimental setup is shown in Fig. 3.1. In the experiment, two Cu_2O samples, i.e. sample I and II of thickness 34 and 54 μm, respectively, are used. Sample I is a high-quality natural crystal collected from the Tsumeb mine in Namibia [51], while sample II is an inferior quality crystal artificially grown by Schwab et al. [10, 60]. The samples are immersed in a liquid Helium-3 bath inside a cryostat to maintain a constant temperature of 1.3 K. The probe laser illuminates the sample perpendicular to its surface, while the pump laser is directed at an angle. The diameter of the pump laser at the sample is 300 μm, three times larger than that of the probe laser spot size of 100 μm. Moreover, the spot sizes of both beams are selected in such a way that both beams perfectly overlap, which is further ensured by maximizing the pump-induced change of the probe signal using a lock-in amplifier. At high pump powers, pump stray light on the path of the probe beam may result in erroneous measurement results. Therefore, before hitting the sample, both laser beams are cross-polarized using two Glan-Taylor prisms. Behind the cryostat, on the detection side, a Glan-Taylor prism filters the pump's stray light while ensuring maximum transmission of the probe laser light. Both pump and probe beams are recorded simultaneously using two photodiodes (New focus large area photo receiver 2031). Additionally, the photoluminescence (PL) signal from the sample, in the spectral range of 600 - 900 nm, is acquired

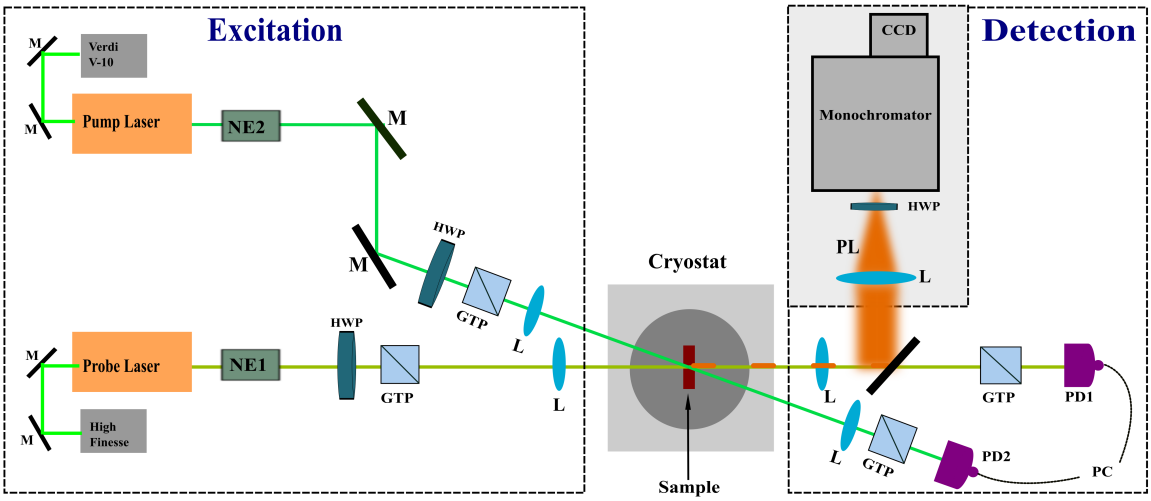

Figure 3.1: Schematic representation of experimental setup: CW pump light excites Rydberg exciton in a cryostat-housed sample. Another CW laser namely a probe laser followed by a photodiode detects the change in crystal behaviour as a means of quality of the scanned absorption spectrum. Abbreviations: NE: noise eater; M: mirror; HWP: half-wave plate; GTP: glan-taylor prism; L: lens, PD: Photodiode, CCD: charge-coupled device.

with the help of a spectrometer (Action SpectralPro-500i). The spectral resolution of the recorded PL spectra is 4 meV.

3.1.2 Enhancement of absorption

First, we discuss the linear absorption spectrum of RE by scanning the probe laser energy (E_{probe}), while the pump laser energy (E_{pump}) is fixed close to the bandgap. The reason for fixing the pump laser energy near the bandgap will be discussed in detail later. The typical absorption spectra are shown in Fig. 3.2(a). The black curve shown here represents the bare spectrum (without additional illumination by the pump laser) from $n = 7P$ up to the bandgap. The probe laser is weak and has a power of 200 nW. Here, the probe power is deliberately kept low to avoid self-blockade effects [51]. The sample used here (sample I) is of high quality. Therefore, resonances of RE up to principal quantum number $n_{max} = 24P$ are readily observed. Moreover, the position of the sample where both beams overlap and impinge plays a key role in determining n_{max} owing to the inhomogeneous distribution of impurities. In our case, the sample quality is more or less uniform. Thus, n_{max} does not vary significantly across the sample. Beyond the n_{max} resonance, we observe a flat continuum with weakly increasing absorption up to the band gap E_g. The starting energy position of this continuum is called apparent band gap $\tilde{E}_g$ (indicated by the red arrow), which is 140

μeV below the nominal band gap $E_g = 2.17208$ eV.

Exciton-exciton [39, 108] or exciton-plasma (e-h) [33, 98] interactions were mostly studied at considerable pump laser powers so far. Although the demarcation of the pump power regime is not so clear, at low pump powers, the effect of impurities on RE is believed to be dominant. In this measurement, we investigate the effect of low pump laser powers on the absorption of the probe laser. We illuminate the crystal with an additional pump laser with energy 2.1719034 eV, close to the apparent bandgap $\tilde{E}_g$. The red and blue curves in Fig. 3.2(a) represent the resulting absorption spectrum measured in the presence of additional pump laser with power 40 nW and 700 nW, respectively. A comparison of the unpumped (black) and pumped (red and blue) spectra reveals the improvement of resonance lines with the presence of merely a few tens of nanowatts of pump power. All exciton resonance lines show an increase in absorption while the absorption between resonances decreases. As a result, for low-n exciton states, the F-exciton triplets become sharper and more pronounced as shown in Fig. 3.2(b). High-n states are further zoomed in panel (c) of Fig. 3.2 to show the enhanced absorption of high Rydberg states in the presence of the pump laser. We observe an increase in absorption by a factor of 1.5 between $n = 10P$ to $15P$ for a single exciton resonance. The change in absorption decreases with increasing n. Furthermore, intermediate peaks that originate either from the coherent superposition of adjacent exciton resonances [29] or even parity D-states [62], vanish in the presence of the pump laser.

3.1.3 Fitting exciton resonances and line-shape parameters

We quantitatively analyze the data and look for changes in various parameters defining a single resonance peak, induced by the pump laser. Therefore, the spectrum is fitted using an asymmetric Lorentzian function with a Fano-like line shape [101, 104]. The fit function is defined as follows

$$\alpha_n(E) = \frac{O_n}{\pi} \frac{\Gamma_n/2 + 2q_n(E - E_n)}{(\Gamma_n/2)^2 + (E - E_n)^2}, \tag{3.1}$$

where O_n is the oscillator strength, Γ_n is the linewidth, E_n is the resonance energy and q_n is the asymmetry parameter. The details of the fitting procedure and a brief demonstration are given in the appendix 6. The parameters obtained after fitting the above function Eq. 3.1 to the experimental data are plotted in Fig. 3.3. Panels (a), (b), (c) and (d) represent O_n, Γ_n, E_n and q_n as a function of principal quantum number n, respectively. In all the panels, black dots indicate the unpumped condition, while red and blue dots corresponds

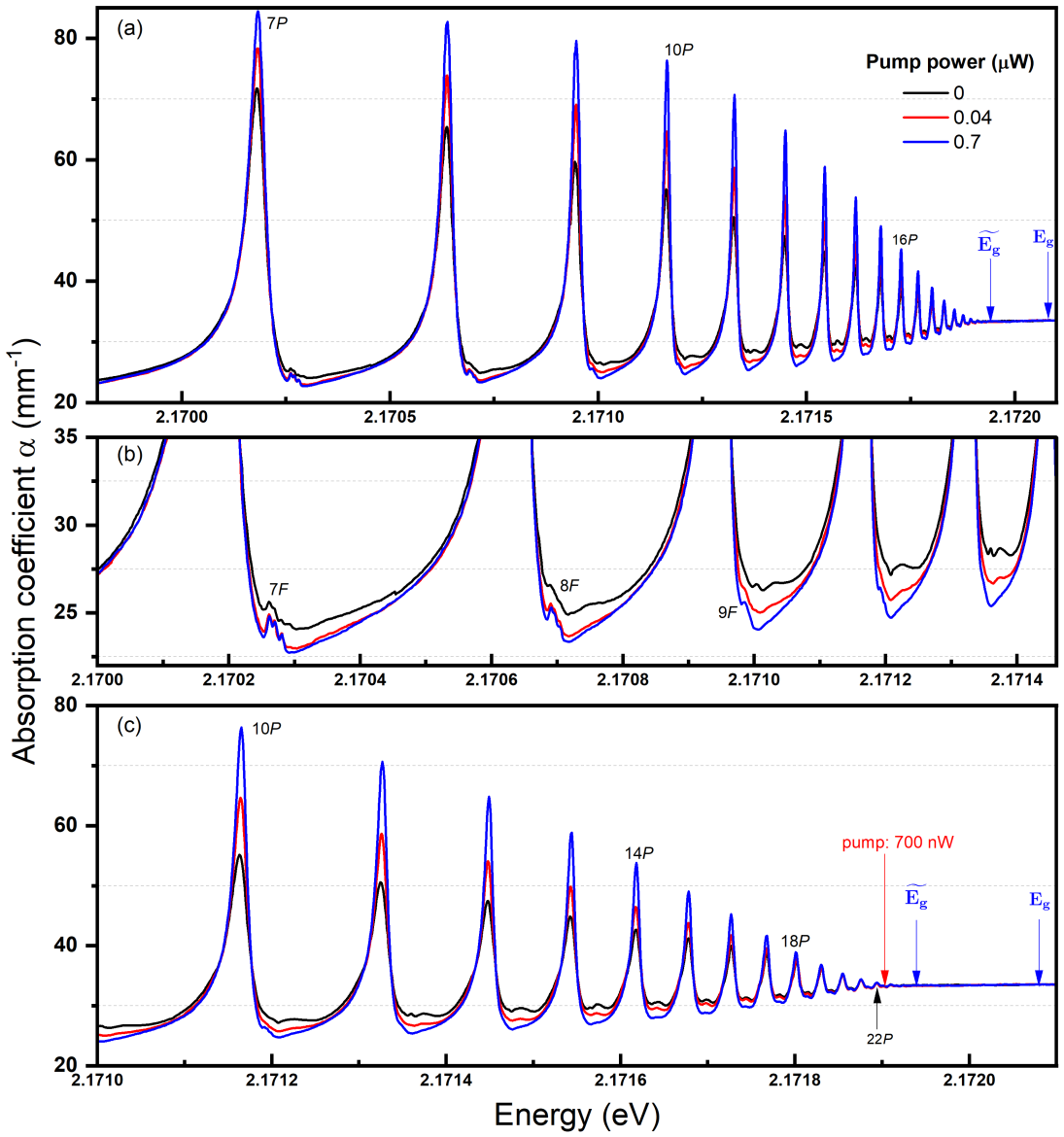

Figure 3.2: (a) Linear absorption spectrum of Rydberg excitons starting from $n = 7P$ up to the band gap, in absence of a pump laser (black) and with an additional pump laser with powers of 40 nW (red) and 700 nW (blue), respectively. The pump laser carries the photon energy 2.1719034 eV, close to the shifted apparent band gap $\tilde{E}_g$ (red). The scanned probe laser power is set to 200 nW. As an influence of the presence of the pump laser, a growth of oscillator strength and a narrowing of resonance lines is observed, which results in increased peak absorption. (b) Highlights the low-n states from $n = 7P$ to $11P$. Absorption between adjacent P-exciton resonances decreased due to the influence of the pump laser. This results in more pronounced and distinct F-exciton resonances. (c) Focuses on high-n states from $n = 10P$ to $22P$. Absorption is increased up to $n = 18P$. However, high n-states ($> 18P$) do not show any improvement. The highest observable state (n_{max}) is also not increased.

to the presence of pump lasers with powers 40 and 700 nW, respectively.

According to Elliot's theory [19], for an ideal system, n^{-3} scaling is expected for oscillator strengths (O_n). Moreover, the linewidths (Γ_n) should also follow a similar n^{-3} scaling. The green straight lines in panels (a) and (b) represent the ideal n^{-3} scaling. In the case of low-lying states (i.e. $n_{probe} < 10P$), both O_n and Γ_n follow the ideal scaling. However, for high-n states (i.e. $n_{probe} > 10P$), strong deviations of parameters from the ideal scaling are observed. In fact, O_n shows a sharp drop, while Γ_n does not change beyond $17P$, leading to a saturation value of 10 μeV. The deviation can be attributed to the presence of charged impurities in the crystal [58], which strongly influences high-n states owing to their large polarizability. On the other hand, surprisingly, the exciton resonance energy (E_n) does not show a significant amount of shift due to the pump laser. Similarly, the asymmetric parameters (q_n) do not change much in the presence of the pump laser.

3.1.4 Pump power dependence of purification

So far, the purification process has been demonstrated by comparing absorption spectra without a pump laser and in the presence of a pump laser with power of 40 nW and 700 nW, respectively. In this subsection, the pump power dependence of the purification process and its amplitude are discussed. We measure the absorption spectra (as shown in Fig. 3.2(a)) at several pump laser powers and estimate the change in absorption coefficient (α) for each exciton resonance. In Fig. 3.4(a), the values of α as a function of pump power are plotted for the principal quantum number from $n = 8$ to 20. The α values mentioned here are calculated without subtracting the underlying continuous phonon background. At low pump powers, for all n_{probe} states, α values strongly increase with the increase of pump laser power up to a maximum (α_{max}). After that, a drop in α values is observed due to the onset of Rydberg or plasma blockade. The pump power needed to obtain α_{max} marginally varies among n_{probe}. For low-n states, slightly more power ($\sim$2 μW) is required while high-n states show maximum change already at 700 nW of pump power. Overall, a relatively small amount of pump power is needed for maximal purification.

In fig. 3.4(b), the change in absorption coefficient ($\Delta\alpha = \alpha_{pump} - \alpha_0$) is plotted as a function of n_{probe} for the three absorption spectra shown in Fig. 3.2, in black, red and blue dots. We observe an increase in $\Delta\alpha$ up to $n = 10$ followed by a steady drop. High-n states beyond $n = 19$ do not show signs of increased absorption. However, the pump laser power needed for the maximum change in absorption ($\Delta\alpha_{max}$) is different for different exciton states. The green dots represent the $\Delta\alpha_{max}$, while purple hollow dots bare α for respective n_{probe}. $\Delta\alpha$ is maximum between $n = 8$ to 13 which is already a factor of 1.5 as compared to the unpumped case. $\Delta\alpha$ reaches the highest value of 24 mm^{-1} for $n = 9$.

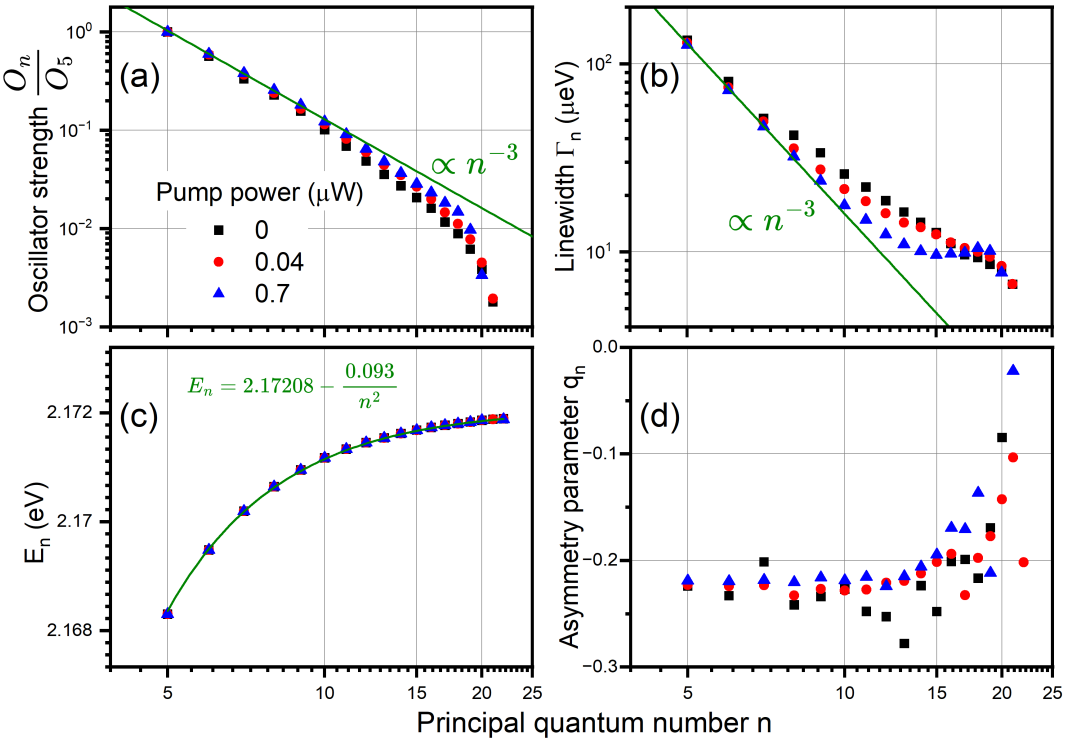

Figure 3.3: Fitting parameters such as normalized oscillator strengths $\frac{O_n}{O_5}$ (a), linewidths Γ_n (b), resonance energies E_n (c) and asymmetry parameters q_n (d) for absorption spectra shown in the Fig. 3.2, as a function of principal quantum number n for three different pumping conditions: Unpumped (black dots), pumped with powers 40 *nW* (red dots) and 700 *nW* (blue dots). With the illumination of a few 100s of nanowatts of pump laser at an energy close to the shifted bandgap, O_n and Γ_n of resonance peaks from 6 to 15*P* are substantially improved and come closer to the ideal n^{-3} scaling (green straight lines in panel (a) and (b)). High-*n* states do not show any improvement. The resonance energy E_n does not change with pump power. Asymmetry parameter q_n increases from a negative value to zero with the increase in n. This indicates the homogeneous broadening of high-*n* exciton resonances due to the influence of charged impurities.

The enhancement of excitonic absorption at an energy (E_n) due to the purification leaves its signature through the narrowing of the linewidths (Γ_n) and increase in the oscillator strengths (O_n). We use Eq. 3.1 to fit the spectra measured at several pump laser powers to evaluate O_n and Γ_n. Figure 3.5(a) and (b) show O_n and Γ_n of the even principal quantum number states as a function of the pump laser power, normalised to their unpumped values. At low pump powers up to 200 nW, we observe a steep increase in O_n, while Γ_n drops. Beyond 200 nW, the growth of O_n and the drop of Γ_n are relatively weak. For n= 18, the increase in O_n is the strongest, reaching up to 50% . Surprisingly, Γ_n does not show a drop but rather an increase of 10%. The decrease in Γ_n is found to be strongest for $n = 12$.

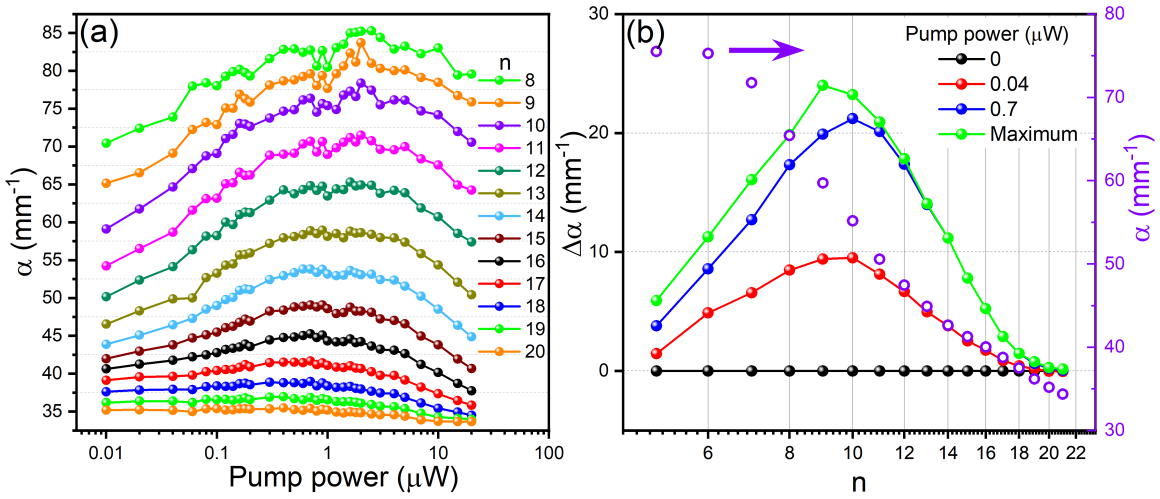

Figure 3.4: (a) Absorption coefficient (α) as a function of pump laser power for different exciton states from $n_{probe} = 8P$ to $20P$. The pump laser energy is 2.1719034 eV close to the apparent bandgap $\tilde{E}_g$. (b) Change in absorption coefficient ($\Delta\alpha = \alpha_{pump} - \alpha_0$) as a function of principal quantum number n from the Fig. 3.2 at zero pump power (black), 40 nW (red) and 700 nW (blue). The maximum change in absorption ($\Delta\alpha_{max}$) for each n_{probe} is plotted in green dots. Low-n states require slightly more pump power for purification than high-n states. The purple open dots represent the bare α_0 at each n_{probe}.

3.1.5 Pump energy dependence of purification

To investigate the role of pump laser energy on purification, we fix the probe laser energy to a specific exciton resonance, in particular $n_{probe} = 14$, and the pump laser is scanned over a wide range of energies from 2.152 to 2.176 eV. The probe and pump laser powers are set to 1 μW and 10 μW, respectively. The transmission of both lasers is monitored individually and simultaneously using two photodiodes. The typical exciton absorption spectrum measured using a pump laser is shown as the black curve in Fig. 3.6(a). The dashed blue line represents background absorption which consists of a phonon background, an exponential Urbach-like tail $\exp((E - \tilde{E}_g)/E_U)$ below the band gap and continuum absorption beyond the band gap. The exponential tail near the band gap originates from the overlap of broadened high-n exciton resonances. The Urbach energy $E_U = 170$ μeV is used here as the width of the tail.

The bare absorption of $n_{probe} = 14$ (i.e. $\alpha_{14,0}$) in the absence of a pump laser is 43 mm^{-1}, indicated as a horizontal grey line in Fig. 3.6(a). Furthermore, the change in probe laser absorption ($\Delta\alpha_{14,pump} = \alpha_{14,pump} - \alpha_{14,0}$) is monitored by scanning the pump laser energy (E_{pump}) across several exciton resonances. The red curve (and right ordinate) depicts the typical probe absorption change ($\Delta\alpha_{14,pump}$) in the presence of a pump laser as a function of E_{pump}. We observe different behaviour of $\Delta\alpha$ depending upon whether the

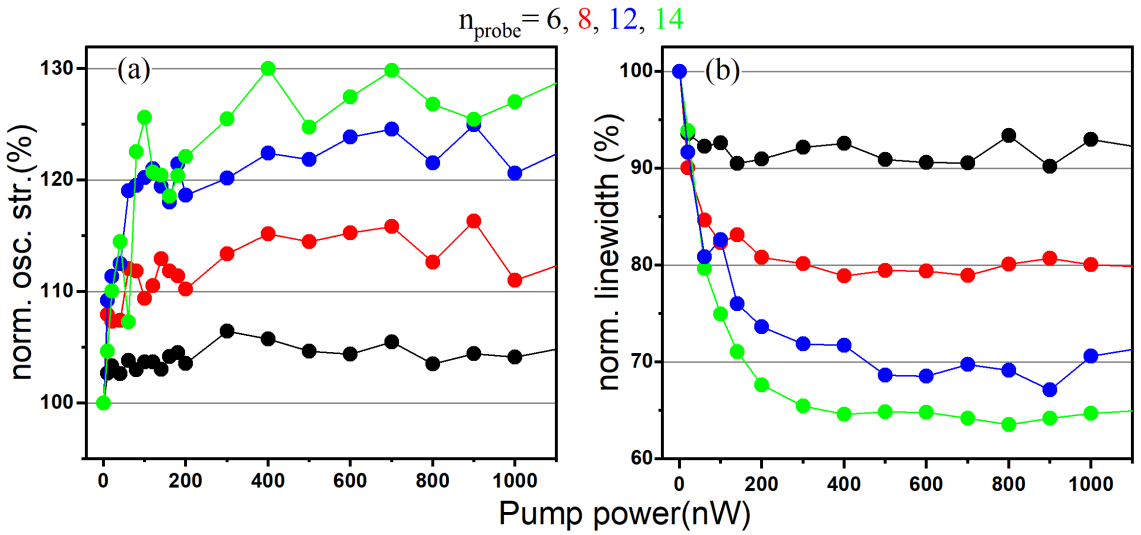

Figure 3.5: Normalised (a) oscillator strength O_n and (b) linewidth Γ_n as a function of pump laser power, for four exciton resonances: 6 (black), 8 (red), 12 (blue) and 14 (green).

pump energy (E_{pump}) is smaller or larger than the probe energy (E_{probe}). Therefore, we discuss both cases separately in the following.

When $E_{pump} < E_{probe}$, we observe a drop in probe laser absorption (i.e. $\Delta\alpha_{14,pump} < 0$). In this situation, the pump laser is either directly absorbed to the low-n exciton states or indirectly to the $1S$ excitons via phonon background. The probe absorption reflects the shape of the phonon background and low-n exciton resonances which can be seen in Fig. 3.6(a). The source of the observed drop in absorption can be attributed to Rydberg blockade or low-density electron-hole plasma formed via Auger decay of $1S$ excitons. The drop in absorption attains its minimum at the pump energy of $n_{pump} = 8$ where the value of α is close to 41 mm^{-1}.

On the other hand, in the case of $E_{pump} > E_{probe}$, generally, an enhancement of absorption (i.e. $\Delta\alpha_{14,pump} > 0$) is observed. This is due to the neutralization of charged impurities by high-lying Rydberg excitons [8, 38]. However, with the increase in E_{pump}, the absorption of the probe also increases steadily until it reaches a maximum. The corresponding E_{pump} at which probe absorption reaches a maximum is $E_{max} = 2.17189$ eV. The energy E_{max} matches with the apparent bandgap $\tilde{E}_g$, the spectral position up to which the highest Rydberg exciton states existing within the investigated sample are excited. The continuous increase in absorption can be described using an Urbach-like exponential tail $\exp((E - \tilde{E}_g)/E_U)$, with $E_U = 170$ μeV, the same width that is used to describe the continuous background absorption in Fig. 3.2(a). The exponential tail is indicated in a dashed violet line in Fig. 3.6(a).

When the pump energy is larger than the apparent band gap, i.e. $E_{pump} > \tilde{E}_g$, the absorption of the probe starts to decrease non-linearly. At these E_{pump}, a low-density electron-hole plasma is created directly, which either screens the charged impurities to create purification or relaxes to the high-n Rydberg states and may thereby neutralize the charged impurities. Overall, the pump energy range, in which enhancement of probe absorption is observed compared to the unperturbed ($\alpha_{14,0}$), extends to around 1500 μeV above the band edge.

During the investigation of probe absorption change with E_{pump}, we find that while scanning E_{pump} across a resonance, the maximum probe absorption change happens at a slightly blue detuning from the resonant energy. This is shown in vertical black and red dashed lines at 10, 12 and 14P exciton resonances in Fig. 3.6(a). The black dashed lines represent the spectral position of the resonance while the red dashed lines stand for the E_{pump} at which the maximum $\Delta\alpha_{14,pump}$ occurs. The energy difference (ΔE) between these two lines drops with the increase in n_{pump}, which is shown in Fig. 3.6(b). The ΔE is found to scale with the inverse power of 3.92 with n_{pump} as portrayed using a fitted red line.

Up until now, the change in probe absorption as a function of the pump laser energy has been investigated by probing at exciton resonance $n_{probe} = 14$. We continue with further investigations of other principal quantum number probe states. We set the probe laser to even principal quantum number states starting from $n_{probe} = 6$ up to 18 and vary the pump laser energy as shown in Fig. 3.7(b). The dashed lines indicate the probe absorption $\alpha_{n,0}$ in the absence of the pump laser, which is acquired by blocking the pump laser. The corresponding resonance for n= 6, 10 and 14 is further illustrated in the right panel. We observe the same characteristic dependence of change in absorption with respect to pump power energy as seen in Fig. 3.6. Pumping at low n leads to a reduction of probe absorption that is followed by an exponential increase up to $E_{max} = 2.17189$ eV which is close to the apparently shifted bandgap $\tilde{E}_g$. The distinct exciton lines are overlaid on top of the continuous background. Overall, for all the probe states, when the pump energy is equal or larger than the probe energy (i.e. $E_{pump} \geq E_{probe}$), probe absorption is enhanced with respect to $\alpha_{n,0}$. E_{max} varies merely within 40 μeV for all the probe n's from $n_{probe} = 8$ up to 18, with $n_{probe} = 6$ being a slight exception which shows a 90 μeV shift from $\tilde{E}_g$.

Beyond the pump energy $\tilde{E}_g$, a reduction of the probe absorption is observed again. The total spectral range in which enhanced absorption is observed drastically drops when the probe energy changes from low-n to high-n. For $n_{probe} = 16$, this range is as narrow as 350 μeV and reduces to around 90 μeV for $n_{probe} = 18$.

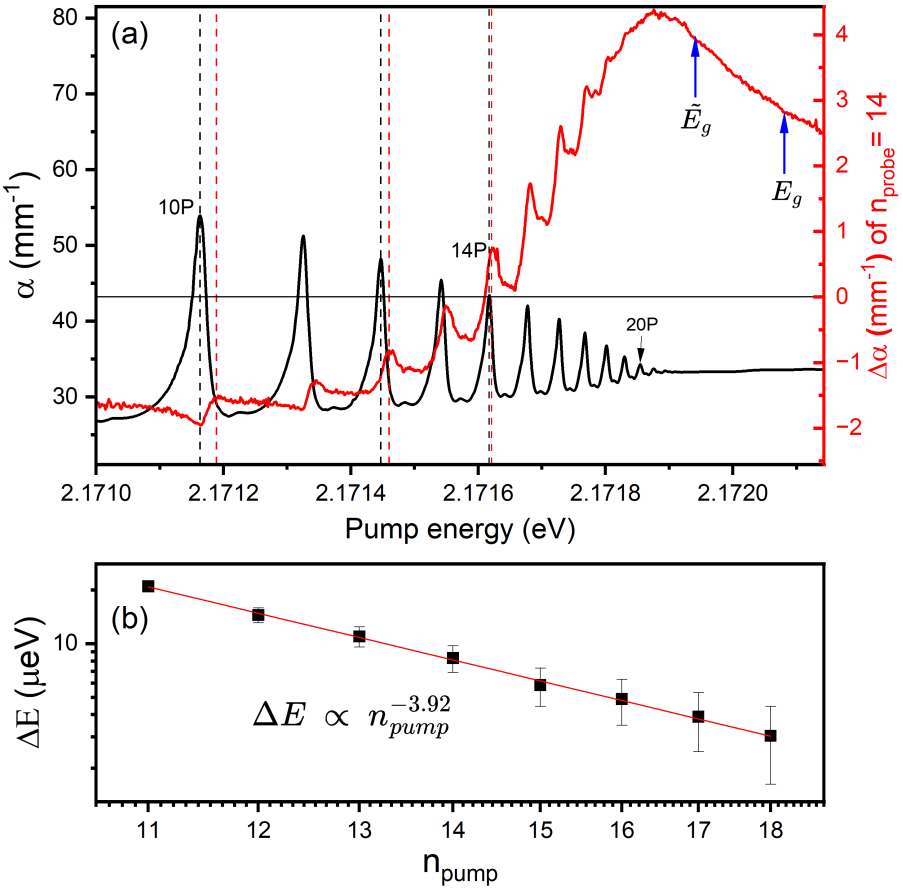

Figure 3.6: (a) Black curve: linear absorption spectrum of exciton resonances (left ordinate). Red curve: change in absorption coefficient ($\Delta\alpha$) of $n_{probe} = 14$ as a function of the pump laser energy (right ordinate) from n= 10 up to the bandgap (E_g). Positive values of $\Delta\alpha$ indicates an increase in absorption, i.e. the purification of crystal, while negative $\Delta\alpha$ represents a reduction of absorption. (b) The energy difference (ΔE) between the maximum probe and pump laser absorption as a function of n_{pump}. ΔE scales as $n_{pump}^{-3.92}$ which is shown in the fitted red straight line.

3.1.6 Sample of inferior quality

So far, the data discussed have been acquired from a high-quality sample (sample I). In this section, the data from an artificially grown inferior quality sample II (sample with large impurity density) is utilised to discuss the enhanced absorption and to further compare it to the high-quality sample. The typical absorption spectrum for sample II is shown in the black curve of Fig. 3.8(a) from n= 6 to band gap E_g. The maximum Rydberg states observed is $14P$, i.e. $n_{max} = 14$. The oscillator strength is damped as compared to sample I. Furthermore, additional peak-like features in between adjacent P-resonances become more prominent. These smaller peaks may be even parity exciton peaks which gain oscillator

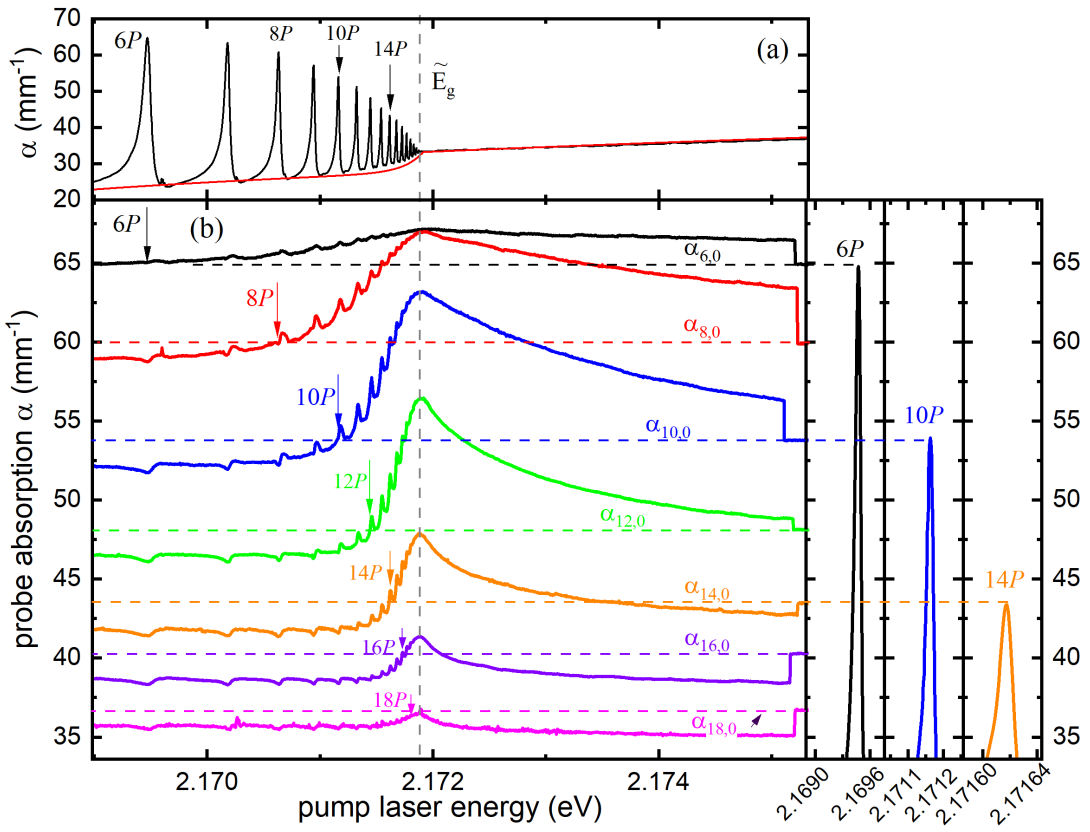

Figure 3.7: (a) Linear absorption spectrum of exciton resonances as shown by black lines. The red line indicates the continuous phonon absorption background and exponential-like Urbach tail below the energy $\tilde{E}_g$. (b) Absorption of probe laser set to the peak of alternate resonances from $n_{probe} = 6$ to $18P$, as a function of the pump laser energy. The plateau shown close to the right y-axis is the absorption of a bare probe laser ($\alpha_{n,0}$) without the pump laser. Based on the pump laser energy, the absorption of n_{probe} is either reduced or enhanced. The maximal absorption for all the n_{probe} is when the pump laser energy is in a spectral range around the apparent bandgap $\tilde{E}_g$. That spectral range reduces with the increase in n_{probe}.

strength due to electric field-induced redistribution from the adjacent P-states. The electric field could be inhomogeneous and weak, stemming from the presence of a higher density of charged impurities.

Akin to Fig. 3.6, we fix n_{probe} at $9P$ and scan the pump laser energy, to determine the maximal energy (E_{max}) that results in the highest absorption enhancement, as shown in Fig. 3.8(b). We found that $E_{max} = 2.17195$ eV, is 250 μeV away from the apparent bandgap $\tilde{E}_g$, which is defined here as the high energy side of $n_{max} = 14$. The spectral position of E_{max} is indicated as a dotted grey line.

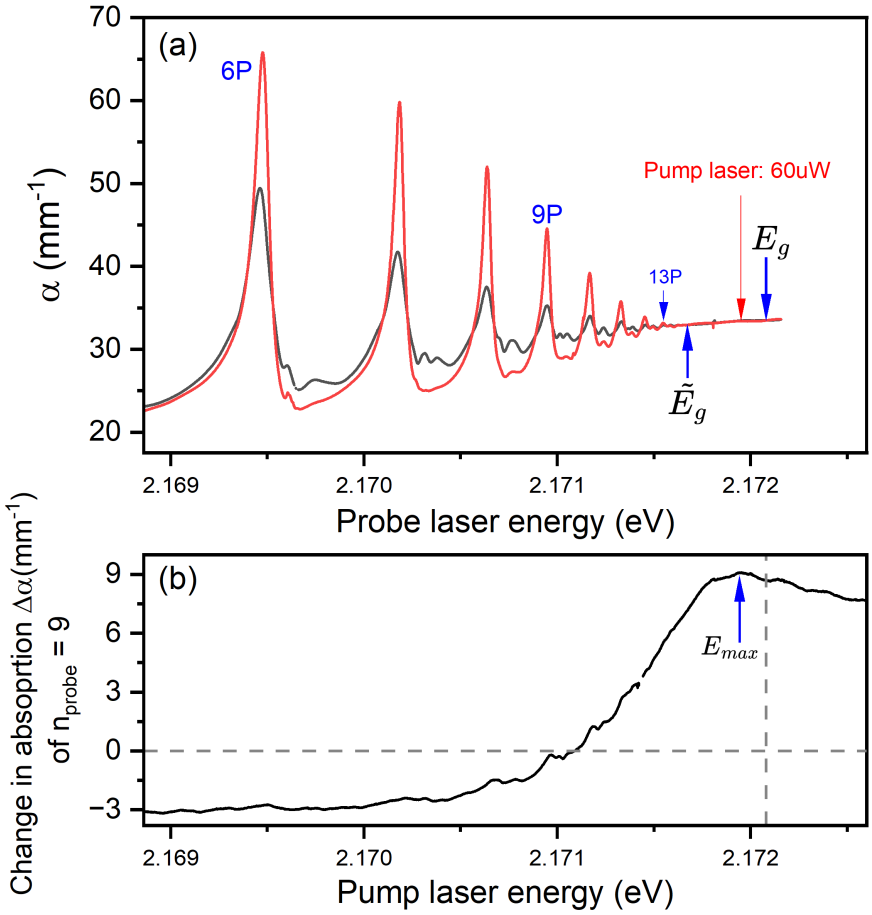

Figure 3.8: (a) Linear absorption spectra of sample II without pump (back) and with pump power of 60 μW (red). The probe laser power is set to 1 μW. (b) Change in probe (n_{probe}= 9) laser absorption as a function of the pump laser energy. The maximal purification is found to be at energy $E_{max} = 2.17195\ eV$. The horizontal grey dashed line indicates the bare absorption of $n_{probe} =$ 9 in the absence of a pump laser.

We fix an additional pump laser with a power of 60 μW at E_{max}, to achieve maximal purification, and scan the probe laser across the Rydberg series up to the bandgap. The corresponding absorption spectrum is shown by the red curve in Fig. 3.8(a). The amplitude of change in absorption is greater in this sample II than in the earlier sample I. For n= 7, absorption is enhanced by a factor of 2, while for $n = 10$, it is thrice. The maximum purification is found to occur at the pump laser power of 60 μW, a factor of 60 higher as compared to the sample I. This further validates our assumption that the sample contains a higher density of impurities, and thus requires a higher density of RE to achieve maximum purification. The intermediate peaks between adjacent low-n states vanish completely and decrease substantially for high-n states. Similar to sample I, the highest number of states does not increase.

3.2 Impurity luminescence

In the previous sections, we have discussed how the absorption spectrum shows narrower lines and more distinct features with an additional excitation of Rydberg states. This observation implies that Rydberg excitons change the charge state of impurities or defects. To further validate this assumption, we look for photoluminescence (PL) of impurities under a similar pump-probe setup. Sample I is used for the PL measurement.

In a typical Cu_2O sample, the common vacancies are Cu, O^+ and O^{++} in increasing order of energy. The O^+ and O^{++} vacancies are predominant in natural crystals, while Cu^- are predominant in artificially grown crystals [41, 42]. As shown in Fig. 3.9, all vacancy emissions are observed at energies below the $1S$ exciton resonance, i.e. below 2.03 eV. Between the resonances of the O^{++} vacancies and the $1S$ exciton resonance, a series of phonon-assisted emission lines of $1S$-para and $1S$-ortho excitons arises. Furthermore, in natural crystals, a broad emission line commonly attributed to excitons bound to metallic impurities exists, which is indicated in region C [42, 44, 96].

During measurement, we excite the crystal non-resonantly using a laser at an energy of 2.33 eV (530 nm) with a power of 10 μW. The free charge carriers formed due to the non-resonant excitation may create excitons which eventually get trapped at the impurity sites. The trapped exciton then radiatively recombines. The resulting emission features are shown as black bold curves in both Fig. 3.9 and 3.10(a). The singly (O^+) and doubly charged oxygen (O^{++}) impurities emit at energy 1.52 and 1.72 eV, respectively. Along with O^+ and O^{++} impurities, we observe a broad emission with an exponential tail-like feature elongated towards lower energy at around 1.9 eV which is indicated as **C**. The appearance of **C** can be attributed to the excitons bound to the metallic impurities.

To investigate the impact of RE on the PL from exciton-bound impurities, we add an additional pump laser whose energy is set close to the shifted bandgap $\tilde{E}_g$. We vary the powers of the pump laser and look for the change in PL. The pump laser may also create additionally PL. During analysis, we carefully subtract the PL originating from the pump laser from the total PL to ensure that we consider only the non-resonantly probe-generated PL which we call residual PL. The validity of this approach depends on the PL signal being far away from saturation, which would result in sub-linear increase of the total PL. We verified that the induced change by the pump laser is much stronger than the expected sub-linear power dependence of the emission features.

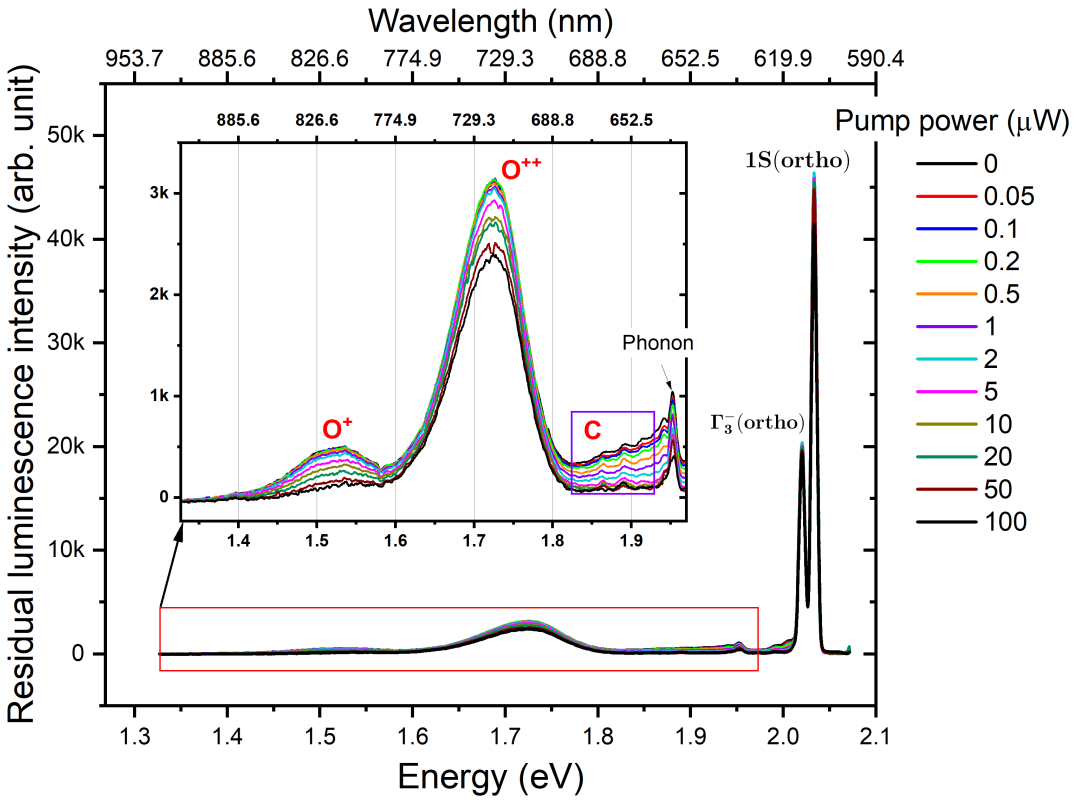

Figure 3.9: Photoluminescence (PL) spectrum measured from energy 1.32703 to 2.071758 eV, at a series of pump laser powers. The probe power is always set to 10 μW. The pump laser is set to an energy of 2.1719034 eV, close to the apparent bandgap $\tilde{E}_g$, while the probe laser is a green laser with an energy 2.33 eV which is above the band gap. Primarily PL emission from O^+ and O^{++} vacancies is observed. PL from Cu^- vacancy is negligible. Additional PL is collected from the spectral region marked as C. In the presence of the pump laser, the PL signal from all of the vacancies starts to drop. This could be due to the neutralization or screening of charged impurities by the pump laser-excited RE.

To quantify the change in emission intensity, we evaluate the area of each emission line by a fit. The O^+ and O^{++} impurity peaks are fitted using Gaussians with amplitude a and width σ at energy E. The emission under **C** curve is fitted as an exponential background decaying from $E_C = 1.95$ eV to lower energies with total amplitude being a_C and decay strength σ_C. The total fitting function is given by

$$f(E) = a_C \cdot e^{-\sigma_C(E-E_C)} + a_+ \cdot e^{-\left(\frac{E-E_+}{\sigma_+}\right)^2} + a_{++} \cdot e^{-\left(\frac{E-E_{++}}{\sigma_{++}}\right)^2} \tag{3.2}$$

The peak area is calculated using the amplitude and width of peaks found from the fittings, which are plotted in Fig. 3.10(b). Blue, green and red dots represent the normalised peak area for vacancies O^+, O^{++} and region **C**, respectively. For all of them, we observe a reduction in their residual PL with increasing pump laser power. The PL signal of **C** shows

an 80% reduction at just 10 μW of pump power. At the same time, to see a similar amount of PL reduction in O^{+}, 10 times more pump laser power is needed. The drop of peak area under O^{++} is a mere 20% at 100 μW.

The total non-resonantly excited PL signal is a measure of the amount of singly and doubly charged oxygen and metallic-bound impurities present in the crystal. The observed drop in PL with pump laser powers can be interpreted as the neutralization or the screening of charged impurities.

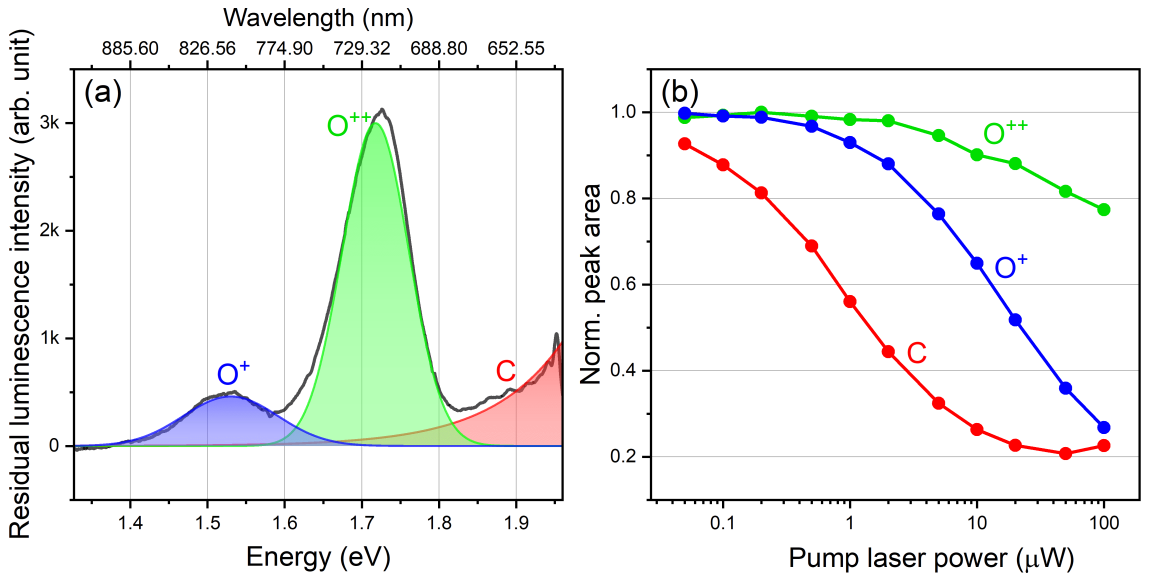

Figure 3.10: (a) Residual PL intensities of excitons bound to different vacancies O^{+}, O^{++} and region **C**, shown in blue, green and red coloured shaded areas, respectively. The area under these PL peaks is calculated using the fitting function (Eq. 3.2). (b) Normalised peak areas of O^{+}, O^{++} and region **C** as a function of pump laser power. The area under all of these vacancies drops with the increase in pump power. The region **C** drops by 80% in just 10 μW of pump power, while O^{+} needs 10 times more power to drop by the same amount. O^{++} drops only 20% at 100 μW.

3.2.1 Temperature dependence of impurity PL

To extend the discussion further, we demonstrate the temperature dependence of photoluminescence of impurities. The measurement is performed on the high-quality sample I by varying temperature from 1.3 K to 70 K at steps of 5 K. The resulting residual PL spectra from 1.32 eV up to 2.06 eV are shown in the upper panel of Fig. 3.11. In the lower panel, the depicted PL spectra are measured in 1 K steps in the low-temperature regime. For better visualization, in both upper and lower panels, the complete spectral regions(i.e. from 1.32

to 2.06 eV) are divided into two parts. Akin to the observation in the previous subsection 3.2, we see singly and doubly charged oxygen vacancies at around 1.52 eV and 1.72 eV, while copper vacancies are almost absent.

When the temperature is cranked up, the integrated emission of O^{+} and O^{++} peaks increases up to a saturation at around 60 K as shown in Fig. 3.11(a). Moreover, the integrated emission of both O^{+} and O^{++} is evaluated by using fit function Eq. 3.2 which is shown by the red and blue dots in Fig. 3.12(b). This is in contradiction with what is observed by Koirala et al. [56], where a drop in PL intensity of oxygen impurities is observed starting from a temperature around 40 K. The drop in PL intensity is expected to begin at the temperature when thermal activation energy (E_A) is enough to free the excitons bound to the impurity sites i.e. $k_B T = E_A$. For O^{++}, E_A is estimated to be 0.033 eV [56]. The PL intensity is defined as follows [75].

$$I(T) = \frac{I_0}{1 + \zeta e^{-\frac{E_A}{k_B T}}}, \tag{3.3}$$

where I_0 is the PL intensity at very low temperature and ζ is the ratio between thermal escape and radiative decay rate.

Furthermore, the exponential tail-like feature in Fig. 3.11(a) which is attributed to the metallic impurities (**C**) strongly decreases at low temperatures and vanishes beyond 10 K. The corresponding area is shown by black dots in Fig. 3.12(a). A similar observation for spectral region **C** is reported by Zhang et al. [44]. Moreover, the vanishing of region **C** at a temperature of 10 K might be related to the reduction of oscillator strength and broadening of the linewidth of Rydberg exciton resonances at the same temperature.

The PL of 1*S*-ortho exciton decreases and the resonance is red-shifted with the increase in temperature. On the contrary, the PL of the Γ_3^- phonon corresponding to 1*S*-ortho exciton reduces slowly and its peak blue shifts until 20 K. After 20 K, we observe a fast rise in the PL signal as well as red shifting of the already blue-shifted peak.

3.3 Screening of external electric fields

Until now, we have discussed the enhancement of absorption of individual exciton resonances upon application of a low-intensity pump laser at an energy close to the shifted band gap $\tilde{E}_g$. The pumped RE neutralize the charged impurities inherent to the crystal and thereby reduce the Stark effect induced by the inhomogeneous stray electric field originating from these static charged impurities. In this section, we demonstrate the neutralization of an external electric field through the injection of high-*n* RE.

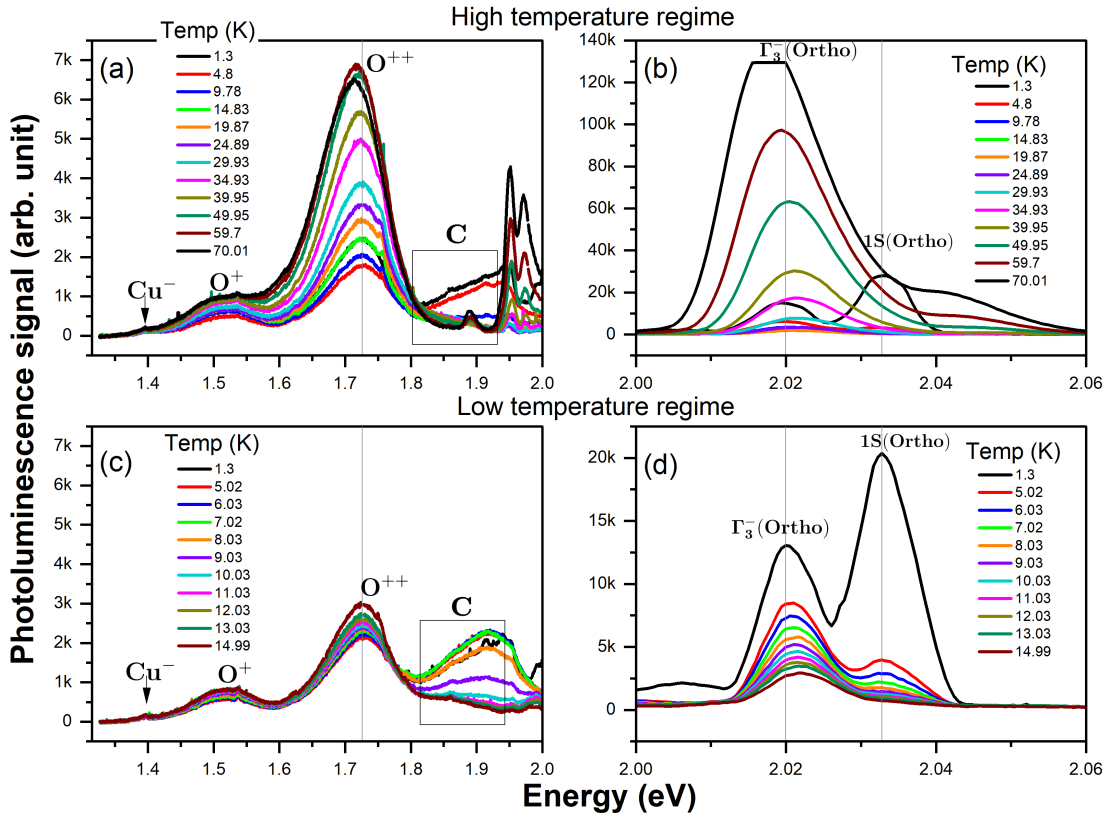

Figure 3.11: (a) and (b) Photoluminescence (PL) spectra from energy 1.32703 eV to 2.071758 eV, at several temperatures starting from 1.3 K to 70 K. Peak PL intensities of O^{+} and O^{++} increase with the increase of temperature up to 60 K. Cu^{-} is almost absent (expected in natural crystal), while the region **C** originating from metallic impurities vanishes at temperature 10 K. The resonance of 1*S*-ortho exciton simultaneously gets red-shifted and its PL intensity drops with an increase in temperature. The PL intensity of Γ_3^- phonon drops at low-temperature up to 15 K and then increases. In the lower panel, (c) and (d) PL spectra are measured at a low-temperature regime at a step of 1 K.

3.3.1 Experimental setup

For the measurement, the same setup as shown in Fig. 3.1 is used, except the sample holder is modified to provide a uniform electric field perpendicular to the sample surface. The schematic diagram of such a modified sample holder is shown in Fig. 3.13. The sample is sandwiched between two electrodes formed by thin layers (∼100 nm) of ITO (Indium tin oxide). The ITO layers are grown on top of 5 mm thick Quartz slabs, which provide strength to the overall structure. The optical transparency of ITO and Quartz layers at the used pump and probe wavelengths ensures that the pump and probe light do not attenuate or interact much while passing through those layers. The ITO electrodes are connected to a signal generator which provides alternating RF signal at a frequency of 2 KHz.

The sample employed here is 54 μm thick and a high quality natural Cu_2O crystal.

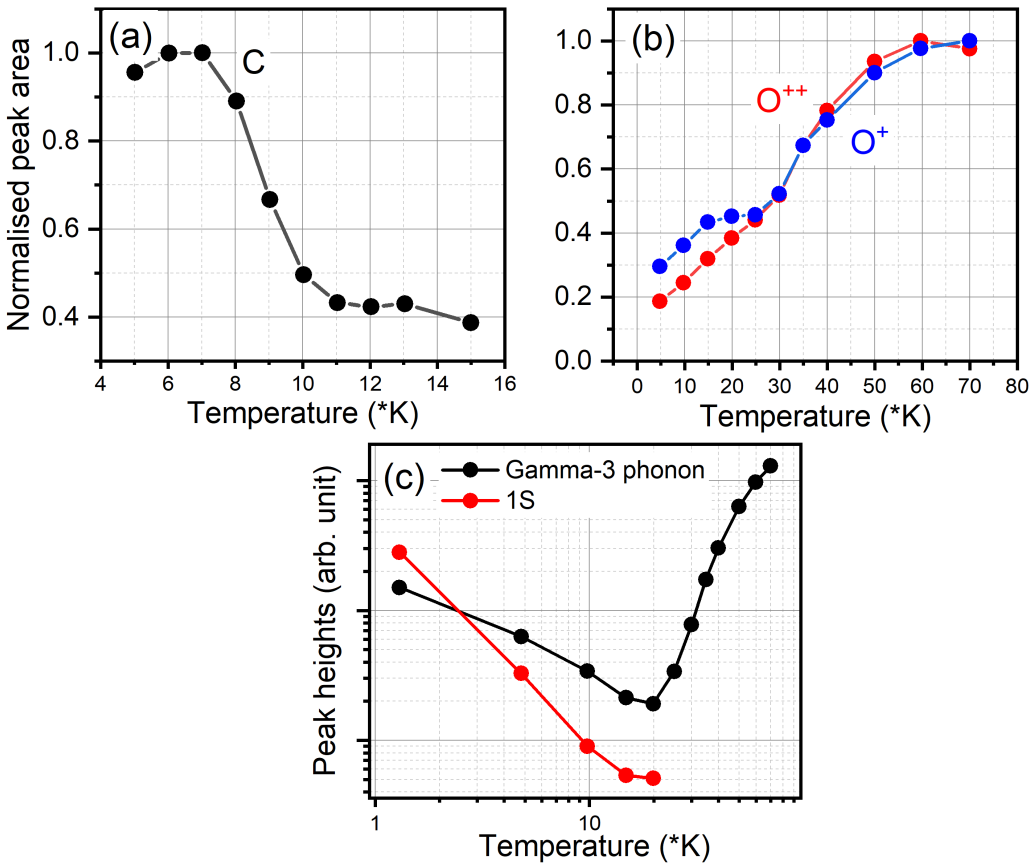

Figure 3.12: (a) Normalized peak area under region **C** of Fig. 3.11 as a function of temperature. The normalized peak area strongly decreases below the temperature of 10 K and becomes constant. (b) Normalised peak area under the PL spectra of O^{+} and O^{++} impurities as a function of temperature. The area monotonically increases up to the temperature of 60 K. (c) Change in peak heights of PL of 1*S*-Ortho exciton (red curve) and Γ_3^- phonon (black) are plotted against temperature. The resonance of 1*S*-ortho exciton is completely ionized at 15 K. On the other hand, PL of Γ_3^- phonon decreases up to around 15 K and starts to increase again.

The quality of the sample is such that maximal Rydberg states up to $n_{max} = 19$ are readily observed. Furthermore, the crystal is cut along the $[110]$ plane. The crystallographic axes are depicted in Fig. 3.14. The electric field is applied along the $[110]$ plane, which is also the direction of the optic axis of the probe laser. The optic axis of the pump laser is at an angle to the $[110]$ plane. The polarization of the probe and the pump laser are set parallel to $[001]$ and $[1\bar{1}0]$ directions, respectively.

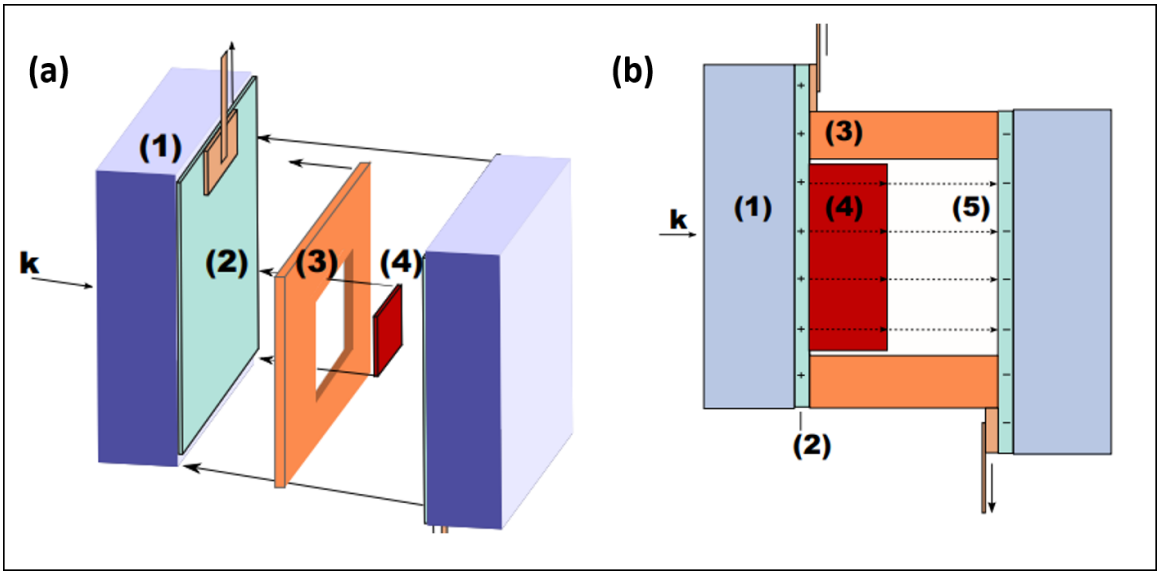

Figure 3.13: Schematic sketch of the sample holder, employed to produce a uniform electric field. (a) exploded view and (b) side view. Quartz plates (1), ITO layers (2), Kapton spacer with thickness 75 μm (3) and Sample (4). Liquid helium fills the free space. Sketch of the sample holder adapted from [34].

3.3.2 Absorption increment in electric field

Akin to the already demonstrated linear absorption measurements in pump-probe settings, we perform analogous measurements in the presence of a uniform external electric field. The green and black curves in Fig. 3.15(a) represent the typical absorption spectrum without an electric field and with a 1Volt electric field, respectively. The spectra are obtained by scanning the probe laser energy from $n = 6P$ up to the bandgap without the presence of an additional pump laser. The power of the probe beam is 1 μW and deliberately kept weak to avoid reaching the non-linear regime and self-blockade effects [51].

Unlike a typical hydrogen atom which is spherically symmetric, excitons are located in a Cu_2O crystal which has a cubic crystal structure, represented by discrete O_h sym-

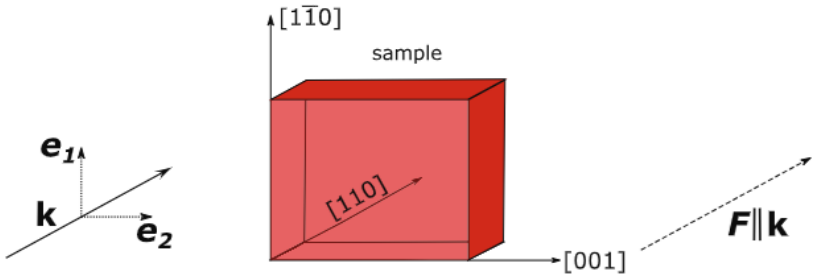

Figure 3.14: Sketch of the crystallographic axes of the sample cut along [110] plane. Picture adapted from [36].

metry. As a result of the symmetry reduction, the degeneracy of different orbital angular momentum (l) multiplets within a single principal quantum number n is naturally lifted and a fine structure splitting is observed even without the application of an electric field. The consequence of that can be observed in the strong deviation of the valance band structure from the generic parabolic dispersion. Thus, the calculation of exciton energy becomes intricate [86, 87, 89].

Besides the reduced symmetry, the parity of valance and conduction band plays an important role in deciding the l states that can be observed. Both the topmost valence band and lowest conduction band which account for the yellow exciton series, have even parity. This renders the electron-hole transition between these bands, electric dipole forbidden. However, excitons having odd envelope wave function (l = 1, 3, 5 $\cdots$) become weakly dipole allowed. Thus, P-type excitons dominate in the absorption spectra as shown by the green lines in Fig. 3.15(a) and (b). However, in the presence of an external electric field, the coulomb potential barrier of the exciton is tilted which leads to the redistribution of oscillator strengths towards adjacent dark excitons. This is directly depicted in the black curve where the oscillator strength of P-states is reduced. At the same time, the growth of oscillator strength of dark even envelope exciton states that are adjacent to odd P-states is observed. Due to the spectral proximity of even and odd parity states, the optical activation of even states may appear as a broadening of P-lines, in particular in the high-n regime.

The red curve in Fig. 3.15 represents the linear absorption spectrum in the presence of an external uniform electric field, and when an additional pump laser is resonant with the state $n_{pump} = 14P$. The pump laser power is set to 50 μW. We observe the regaining of oscillator strength by odd envelop P-states and simultaneously diminishing of dark even envelope states. As a result, the linewidth of P-states is reduced. This indicates the neutralization of the applied electric field by pump laser-induced Rydberg excitons. We expect an alignment of Rydberg excitons along the direction of the electric field and ultimately a stretching of the wave function which leads to an enhancement of its dipole moment. As a consequence, the effective electric field (E_{eff}) inside the crystal is reduced. The E_{eff} is given by

$$E_{eff} = E_{applied} - E_{induced} \tag{3.4}$$

Here, $E_{applied}$ is the electric field that is applied to the crystal and $E_{induced}$ is the field induced due to the counter alignment of RE.

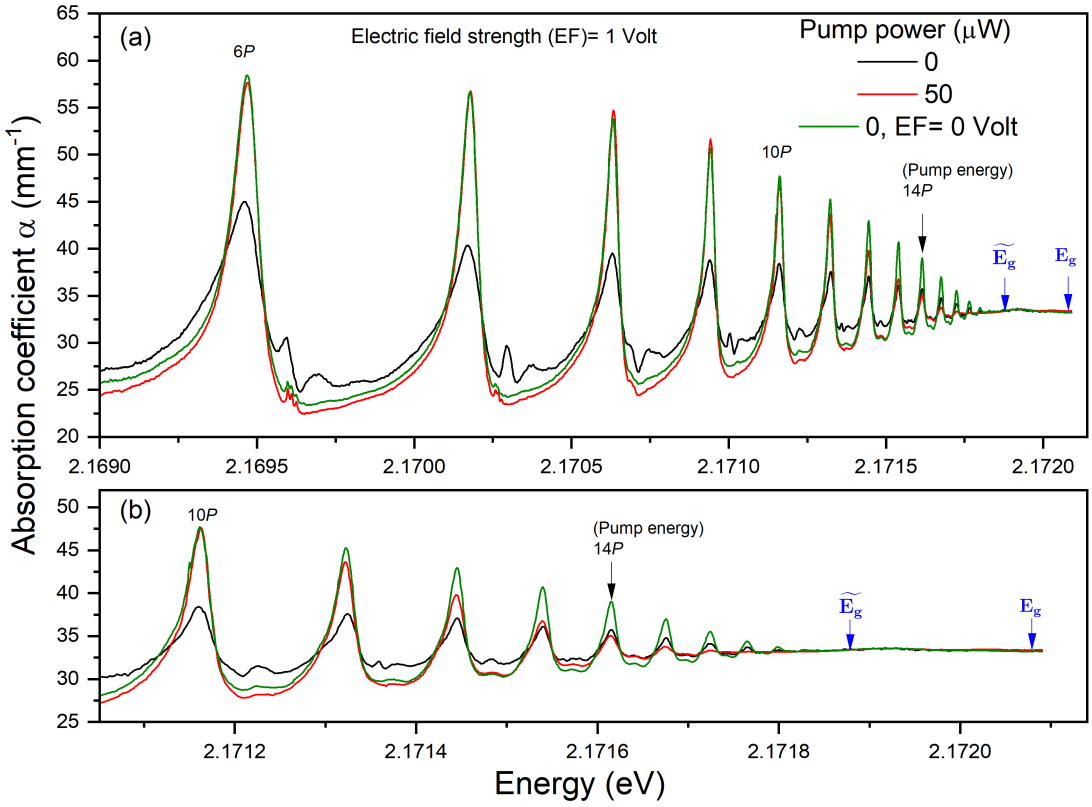

Figure 3.15: (a) Linear absorption spectra in the presence of a uniform external electric field with strength 1 Volt. Black curve: absence of pump laser and red curve: in the presence of a pump laser with power 50 μW, exciting RE at $n_{pump} = 14P$ resonance. The RE align in opposite direction to the applied electric field whereby the net field strength inside the crystal is reduced. Thus, the intermixing of P-states and odd parity states is decreased. As a result, absorption peaks of P-exciton resonances show enhancement and F-exciton triplets become visible. (b) An enlarged version of the spectral region containing High-n Rydberg states. The highest observable state n_{max} does not change.

3.3.3 Pump power dependence of EF neutralization

Similar to the discussions in the previous subsection 3.1.4 and particularly in Fig. 3.4, here, we discuss the change in amplitude of the exciton absorption peaks due to neutralization of the electric field, at several pump laser powers. We acquire the exciton spectra by scanning the probe laser from $n = 6P$ up to bandgap, at different pump laser powers and at a constant electric field strength of 1 Volt. Figure 3.17(a) represents the absorption coefficient α of odd envelope P-states as a function of the pump laser power for different exciton resonance peaks. The values of α are calculated without subtracting the absorption from the phonon background. At low pump powers, the absorption of P-states is enhanced up to a maximal value and then drops. The increase of α at low pump power is due to the neutralization of the external electric field inside the crystal. On the other hand, the reduction of α at

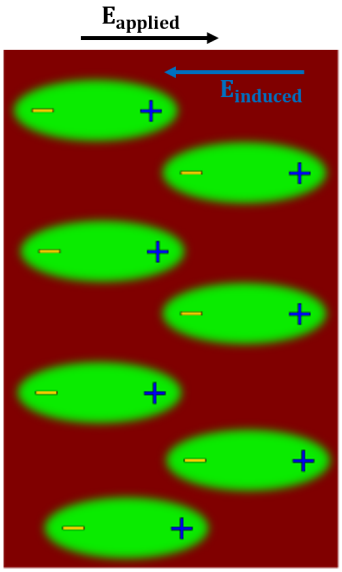

Figure 3.16: External electric field ($E_{applied}$) is applied to a Cu_2O sample. Optically excited RE (green) act as a highly polarizable medium. Thus, RE align opposite to the applied electric field thereby increasing their envelop wave function and dipole moment. The field induced ($E_{induced}$) due to counter polarization of RE reduces the effective field inside the crystal.

large pump powers can be attributed to the onset of enhanced exciton-exciton interaction in an electric field. Basically, due to the enlargement of the envelope wave function and thereby the dipole moment of the RE situated in a uniform electric field, the dipole-dipole interaction between them is likely to be enhanced. At a particular electric field strength, the interaction may even change its character from an induced dipole-dipole interaction (van der Waals type) to a direct dipole-dipole interaction (Förster type). Similar enhancement of the strength of dipole-dipole interaction between Rydberg atoms situated in an uniform electric field, were reported in several past studies, see Refs. [24, 25, 47]. Overall, similar to Fig. 3.4, the pump power required for maximal neutralization of the electric field, drops with an increase in principal quantum numbers.

Figure 3.17(b) shows the change in absorption coefficient ($\Delta\alpha$) as a function of the principal quantum number n, at three different pump laser powers: 5 μW (red), 50 μW (blue) and pump power which give maximal enhancement (green). For $n = 7$, $\Delta\alpha$ has a maximum value of 17.5 mm^{-1}. The maximal value of $\Delta\alpha$ decreases steadily with the increase in n, so much so that for $n = 14$, $\Delta\alpha$ approaches zero.

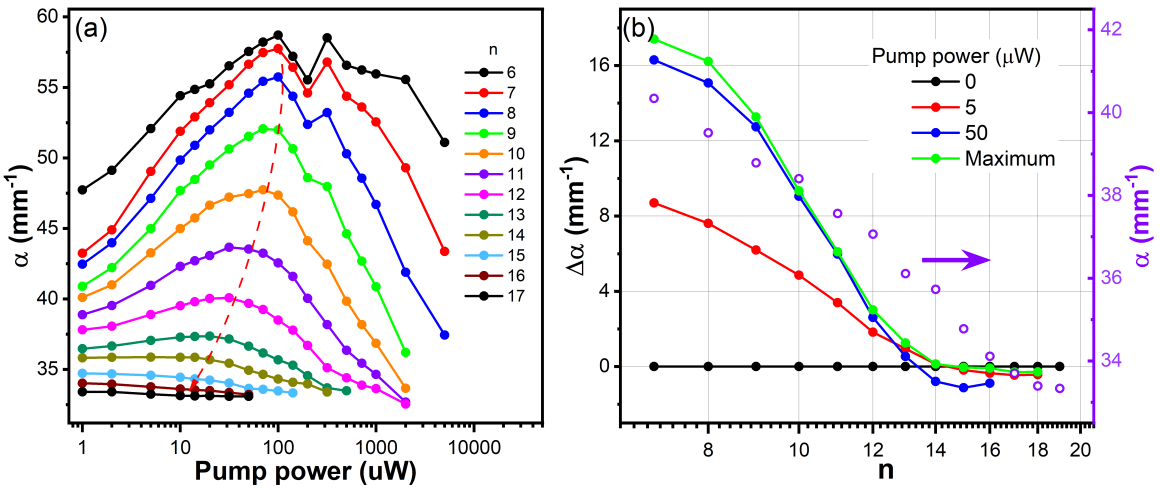

Figure 3.17: (a) Absorption coefficient (α) as a function of pump laser power for different Rydberg states with principal quantum numbers n= 7 to 18P. α increases up to an optimum pump power due to the neutralization of the applied electric field. Thereafter, with the onset of Rydberg blockade α value drops. The optimum pump laser power required to completely neutralize the external electric field decreases with the increase in n. (b) Change in absorption coefficient ($\Delta\alpha$) as a function of principal quantum numbers n without a pump laser (black dots) and in the presence of a pump laser with power 5 μW (red dots) and 50 μW (blue dots). Green dots depict the maximum $\Delta\alpha$ for different P-states at optimum pump laser power. In general, $\Delta\alpha$ drops with the increased n. Purple dots represent the bare α of individual n.

3.3.4 Pump energy dependence of EF neutralization

Akin to the previous investigation of the dependence of purification on the pump laser energy in subsection 3.1.5, here, we enquire about how neutralization of a uniform external electric field changes with the pump laser energy (E_{pump}). On that account, we fix the probe laser to the peak of resonance $n_{probe} = 10P$ and record the transmission of both the pump and the probe laser by scanning the pump laser energy in two different spectral ranges. Firstly, across the 1S resonance which is shown in the left panel of Fig. 3.18 and secondly from the $n = 6P$ to slightly above bandgap which is depicted in the right panel of the same figure. The vertical red line indicates the spectral position of the bandgap (E_g). The pump power is deliberately set to 100 μW (see Fig. 3.17(a)), to achieve maximal enhancement of absorption of $n_{probe} = 10P$ in an electric field. This power is roughly two orders of magnitude higher than in the earlier observation in subsection 3.1.4. The probe laser power is fixed to 1 μW.

For comparison, we record the transmission of both beams at two different settings. First, we apply an external electric field of 1 Volt and in second case, we apply no field at all. The corresponding change in absorption coefficient $\Delta\alpha = \alpha_{pump} - \alpha_0$ as a function of

the pump laser energy is depicted by black and red lines in both left and right panels of Fig. 3.18. Here, the positive value of $\Delta\alpha$, i.e. $\Delta\alpha > 0$, corresponds to an enhancement of absorption, while the negative value ($\Delta\alpha < 0$) indicates the reduction of absorption. The grey horizontal line shows the position where $\Delta\alpha = 0$. Both settings are discussed in detail as follows.

In the presence of an electric field (black curve), for all pump energies (E_{pump}), we observe an enhancement of probe absorption (i.e. $\Delta\alpha > 0$). The maximal increase in absorption ($\Delta\alpha_{max}$) is found to be 10.5 mm^{-1} which is indicated by a blue arrow in the right panel of Fig. 3.18. This occurs when E_{pump} is in the spectral vicinity of the shifted apparent bandgap $\tilde{E}_g$ which is similar to the observation in Fig. 3.6. In general, excitons can align opposite to the applied electric field and gain a permanent dipole moment, thereby reducing the effective electric field inside the crystal. Since, the high-n Rydberg excitons close to $\tilde{E}_g$ have larger polarizability, the efficiency of reduction of an effective electric field should be largest for them. Therefore, $\Delta\alpha_{max}$ occurs near $\tilde{E}_g$. On both high and low energy sides of $\tilde{E}_g$, $\Delta\alpha$ drops steadily. On the high energy side (i.e. $E_{pump} > \tilde{E}_g$), although dropping, $\Delta\alpha$ is still positive above the bandgap up to a few meVs. The reason could be due to the reduction of the net electric field inside the crystal by the polarization of either the directly excited e-h plasma or high-n exciton states created after the relaxation of free carriers. On the opposite side (i.e. $E_{pump} < \tilde{E}_g$), the drop of $\Delta\alpha$ might be due to the relatively small polarizability of low-n excitons (polarizability $\propto n^7$). Interestingly, in this spectral range, the shape of $\Delta\alpha$ as a function of pump laser energy, $\Delta\alpha$ vs E_{pump}, matches with the Urbach tail.

Moreover, we observe $\Delta\alpha \sim 2$ mm^{-1} when E_{pump} is scanned across the 1S-ortho exciton resonance as shown by the black curve in the left panel. This could be due to the indirect formation of a plasma through the Auger effect. Instead of a sharp peak, the zig-zag feature of $\Delta\alpha$ stems from the different transmissivity of the sample holder.

In the absence of an electric field, the recorded $\Delta\alpha$ as a function of E_{pump} is shown by the red curve in the right and left panels of Fig. 3.18. The measurement is akin to what is shown in Fig. 3.6, albeit this time at a higher pump laser power of 100 μW. For all E_{pump}, $\Delta\alpha$ is negative which means the probe absorption is always reduced. This could be due to Rydberg or plasma blockade which usually occurs at high pump power. The minimal value of $|\Delta\alpha| \sim 0$ when E_{pump} is close to the shifted band gap $\tilde{E}_g$, is indicative of the dominance of purification effect by Rydberg excitons even at this pump power.

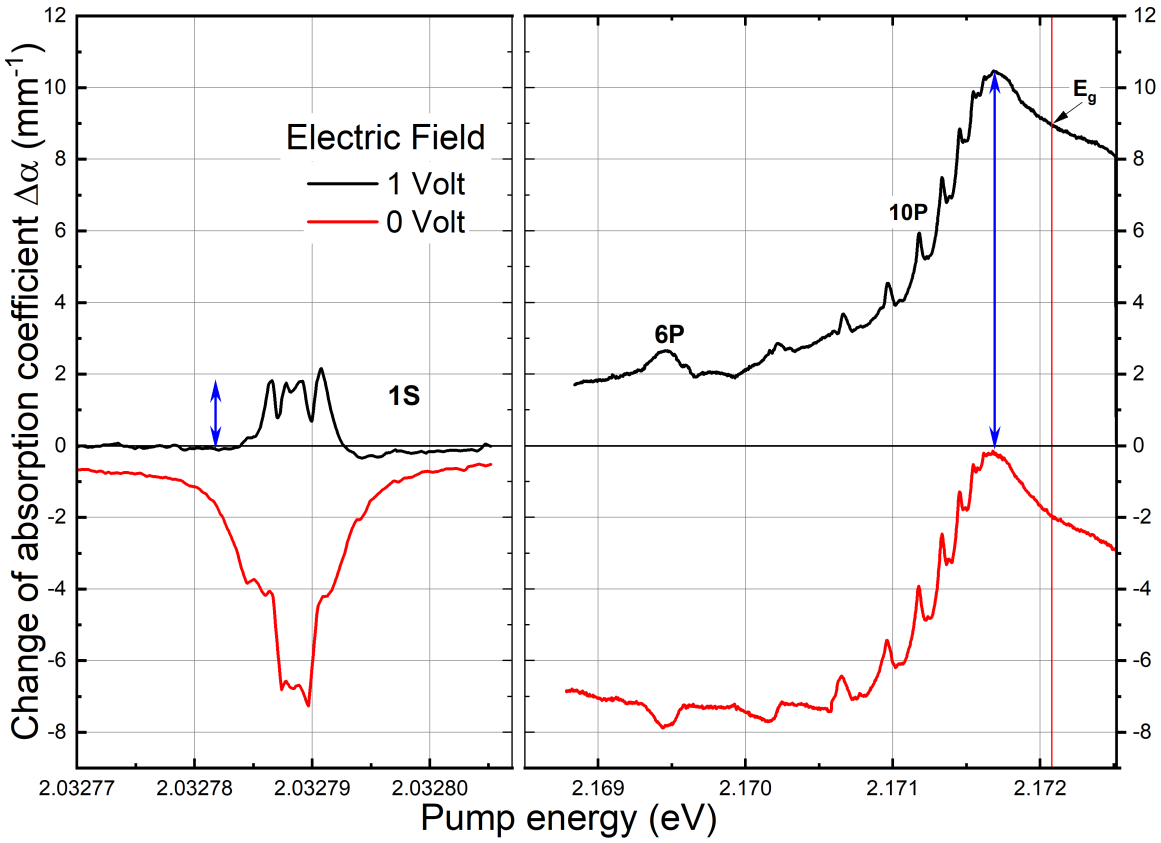

Figure 3.18: Change in absorption coefficient ($\Delta\alpha = \alpha_{pump} - \alpha_0$) for $n_{probe} = 10P$ is plotted as a function of the pump laser energy (E_{pump}). Black curve: with electric field (EF) 1Volt and Red curve: without electric field applied. The pump and probe laser powers are set to 100 and 1 μW, respectively. $\Delta\alpha > 0$ indicates the enhancement of absorption, while $\Delta\alpha < 0$ for a reduction. In the presence of EF, $\Delta\alpha$ is always positive and maximum (10.5 mm^{-1}) when the E_{pump} is at a spectral range close to the shifted bandgap ($\tilde{E}_g$). This indicates the role of high-n Rydberg excitons in the neutralization of EF. At low E_{pump} and particularly for the $1S$ exciton, EF might be reduced due to the counter polarization of Auger-created plasma. When EF is switched off, $\Delta\alpha$ is always negative. The reduction of absorption could arise from known effects like Rydberg or plasma blockade. Moreover, $\Delta\alpha$ is minimal when the E_{pump} is in the vicinity of $\tilde{E}_g$, which can be explained by the purification effect.

3.4 Summary

In this chapter, using CW pump-probe spectroscopy, we demonstrated the so-called "Purification process", which is essentially the neutralization of the charged impurities or vacancies, through excitation of a low density of high-lying Rydberg excitons. As a result of the purification, the Stark effect originating from the inhomogeneous electric field of the charged impurities is reduced, and thus, an enhancement of excitonic absorption up to 100% is observed. The purification sharpens exciton resonances by increasing their oscillator strengths and narrowing their linewidths. The maximal efficiency is achieved when the pump laser energy is at the vicinity of the shifted bandgap ($\tilde{E_g}$) using a pump power between 0.5 to 1 μW.

The purification process was further validated by demonstrating a drop in the photoluminescence (PL) signal from the O^+, O^{++} and metallic impurities (region **C** in Fig. 3.9), upon excitation of a low density of RE. The temperature dependence of PL from impurities was also highlighted. The PL from region **C** vanishes at temperatures around 12 K, while the PL of O^+ and O^{++} increases up to 60 K.

Additionally, we applied an external uniform electric field and demonstrated its neutralization by exciting high-n RE, highlighting the highly polarizable nature of the Rydberg exciton gas.

Chapter 4

Dynamics of purification

In the previous chapter 3, the purification process in a Cu_2O crystal, i.e. the neutralization of charged impurities, was demonstrated under steady state conditions using two CW lasers in a pump-probe configuration. It was observed that purification is most efficient when a low-intensity pump laser is spectrally positioned in the vicinity of the shifted bandgap $\tilde{E}_g = 2.1719034$ eV, and generally when $E_{pump} > E_{probe}$. This chapter provides a more detailed investigation into the origin and temporal dynamics of the purification process using time-resolved (TR) measurements. A first approach was presented by Bergen et al. [8]. In that experiment, the crystal was temporarily driven to a new steady state by employing a pulsed pump laser which excites a certain density of excitons. The corresponding induced dynamical changes in the optical properties of the material, both during and after the end of the pump pulse, were monitored in terms of the change in transmission of a CW probe laser by using a streak camera. However, a fundamental drawback in this type of measurement is the low temporal resolution of the streak camera, which ranges from 100 ns to 1 μs depending upon the selected time window. This limitation practically makes it impossible to estimate, distinguish and segregate the total number of constituent processes contributing to the overall change in probe transmission.

Here, we perform the TR measurement with an improved temporal resolution of 15 ns to study the purification dynamics. We replace the streak camera by a fast photodiode and an oscilloscope. This helps us to explore the intricate temporal dynamics of purification which were not accessible earlier using streak camera. In this chapter, we focus on the purification dynamics under various excitation schemes. The chapter is organised in the following way.

First, we describe the procedure of the TR experiment, including data collection and analysis, in section 4.1. In section 4.2, we discuss measurements where the pump laser energy is set to the energy that yields maximum purification, and we record TR traces of

probe transmission. From these traces, we uncover various underlying constituent phenomena that contribute to the overall purification process. Furthermore, the influence of both the exciton density and an ultra-low density of electron-hole plasma on the purification dynamics are investigated in section 4.3 and 4.4, respectively. In section 4.5, we delve deeper into the investigation of purification dynamics by detuning the probe laser energy from the peak of exciton resonance.

4.1 Experiment

For this measurement, the TR two-colour pump-probe technique is employed using two tunable narrow linewidth (10 neV) dye lasers (Sirah Matisse DS). A schematic diagram of the experimental setup is shown in Fig. 4.1. The continuous wave light from the probe laser impinges perpendicularly on the sample's surface, while the temporally modulated pump light arrives at an angle. The modulation of the pump beam is performed using a signal generator (SIGLENT SDG6032X) and an electro-optic modulator (EOM)(LINOS LM 0202). The signal generator produces a square RF signal at a frequency of 10 kHz and with 2% duty cycle, which is sent to the EOM to modulate the CW pump light. The frequency and duty cycle are chosen based on the longest temporal dynamics we look for, i.e. 100 μs. As a reference, the temporal profile of the pump laser pulse is shown in Fig. 4.3 (a). The rise and fall times of the pump pulse are 2 ns, determined by the signal generator and the EOM used to generate the pulse. Furthermore, a Cu_2O sample with a thickness 34 μm is used for the experiment, which is the same sample I that is used in the previous chapter 3 for the CW purification measurement. The sample is placed inside a bath cryostat and surrounded by liquid helium, ensuring a constant temperature of 1.4 K. This low temperature reduces the risk of thermal ionization of high-lying Rydberg excitons and suppresses the excitation of detrimental phonons. At the sample surface, the diameter of the pump laser is 300 μm, three times larger than that of the probe laser's diameter of 100 μm. Both beams have spatial Gaussian profiles, with their diameters calculated as the full width at half maximum (FWHM). Perfect spatial overlap of both beams is ensured by maximizing the pump pulse-induced change of the transmitted probe signal with the help of a lock-in amplifier or an oscilloscope.

We utilize polarization filtering to discard pump stray light. Before the sample, both laser beams are cross-polarized using two Glan-Taylor prisms. Behind the cryostat, a Glan-Taylor prism filters the pump's stray light while it ensures maximum transmission of the probe laser. On the detection side, a fast avalanche photodiode (Thorlabs, APD430A2) with a bandwidth of 400 MHz collects the transmitted probe light including changes intro-

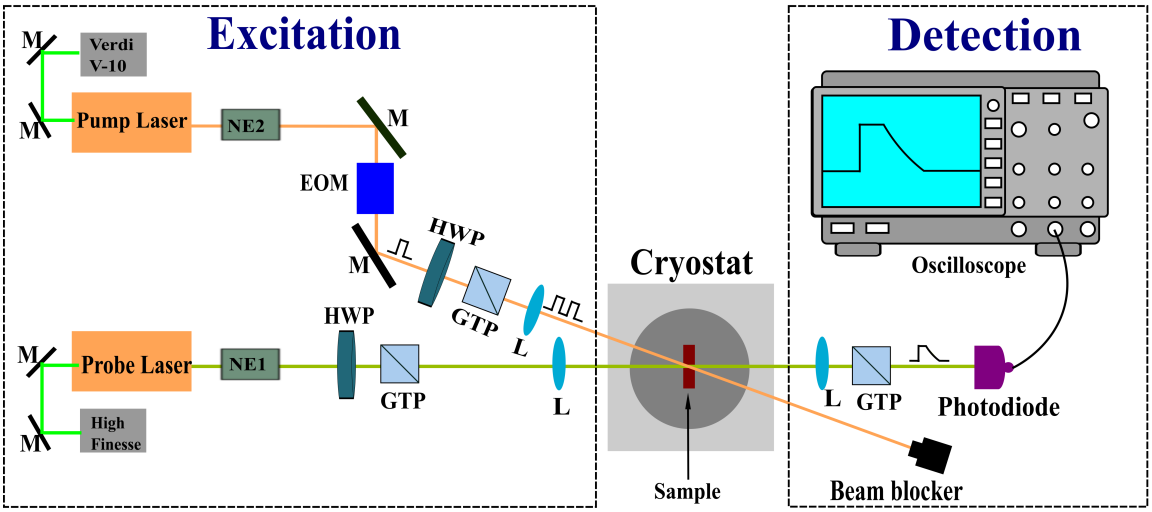

Figure 4.1: Schematic representation of the experimental setup: Modulated pump light periodically induces changes in a cryostat-housed sample which is probed using a CW probe laser accompanied by a fast photo-diode and an oscilloscope. Abbreviations: NE: noise eater; M: mirror; EOM: electro-optic modulator; HWP: half-wave plate; GTP: glan-taylor prism; L: lens

duced by the pump laser. The probe signal is observed and recorded using an oscilloscope (RIGOL MSO5204). The temporal resolution of the oscilloscope is 0.5 ns. Moreover, we collect three different types of transmitted signals as shown in Fig. 4.2(a). The first is the bare signal without probe and pump laser (T_{bkg}) and acts as a background from the surrounding room light and electronic noise of the diode. The second is proportional to the transmitted intensity of the probe laser in the absence of a pump laser, $T_{pr} = T_0 \exp(-\alpha_{pr} d)$, and acts as a reference. The third measures pump pulse-induced changes in the transmission of the probe laser, $T_{pr,pu} = T_0 \exp(-\alpha_{pr,pu} d)$. The corresponding change in absorption coefficient ($\Delta\alpha$) using Lambert's law is defined as follows:

$$\begin{aligned} \Delta\alpha &= \alpha_{pr,pu} - \alpha_{pr} \\ &= -ln\left(\frac{T_{pr,pu}}{T_{pr}}\right) \Big/ d. \end{aligned} \tag{4.1}$$

The term $T_{pr,pu}/T_{pr}$ written in the parenthesis of the above equation is called "Relative transmission" and is calculated after the subtraction of T_{bkg} from both $T_{pr,pu}$ and T_{pr}. As a reference, Fig. 4.2(b) demonstrates the typical evolution of $\Delta\alpha$ with respect to time.

In principle, $\Delta\alpha$ can reach both positive or negative values based on the parameters of the pump and probe laser. A positive value of $\Delta\alpha$ indicates an increase in probe laser absorption caused by purification, as discussed in the previous chapter 3. A negative $\Delta\alpha$ indicates a decrease in absorption, which may arise from well-known effects such as Ry-

dberg blockade [39], exciton-plasma interaction [33, 98, 109] or photoionization of neutral impurities by the excitation laser [58]. Fig. 4.3 demonstrates both conditions of change in α and the corresponding temporal evolution of the probe laser at three different pump intensities.

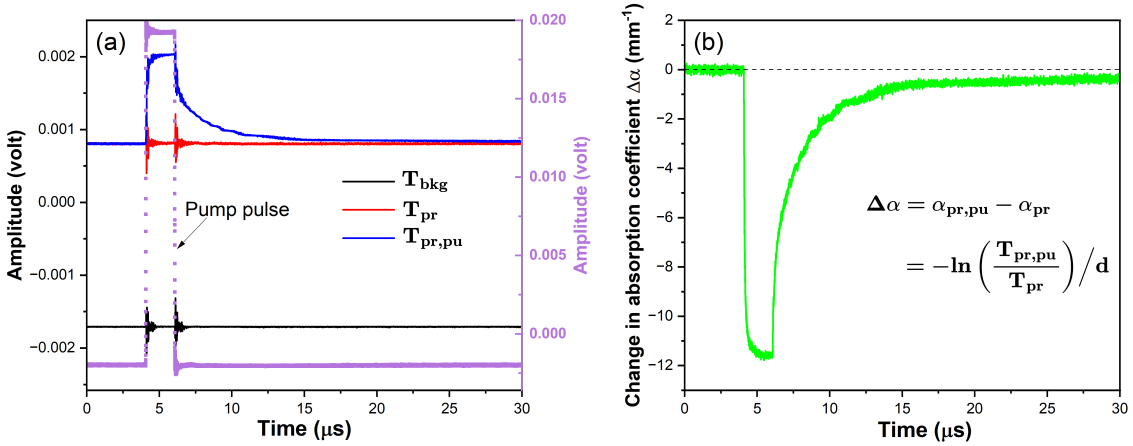

Figure 4.2: (a) (Black) background signal originating from the surrounding light and the electronic noise level of the photodiode (T_{bkg}), (Red) transmission of the probe laser alone (T_{pr}) with an intensity 2.35 mW /cm^2 fixed to the 10P exciton resonance, and (Blue) transmission of the probe laser in the presence of a pulsed pump laser ($T_{pr,pu}$) fixed at energy 2.117957 eV. The purple dots represent the pump pulse in the time domain. (b) Change of absorption coefficient ($\Delta\alpha$) as a function of time. $\Delta\alpha$ is evaluated from (a) using Eq. 4.1.

4.1.1 Response to the pump pulse

The continuous wave probe laser, which measures the absorption, is tuned into a particular exciton resonance. The intensity is kept low to create a finite density of RE. Moreover, the absorption cross-sections and lifetimes of the excitons created determine the exciton density. In addition to creating RE, a certain density of 1S-excitons is also created due to the relaxation of RE and via direct absorption to the underlying phonon background. The probe laser also imbalances the states of impurities present in the crystal, thereby changing their average charge state. The RE created may neutralize a charged impurity or can turn a neutral impurity into a charged one via photoionization. Therefore, for CW illumination at any given point of time the steady state arising is governed by the ratio between the rates of photo-ionization and neutralization. We measure the changes $\Delta\alpha$ in the absorption coefficient relative to this steady state absorption.

Upon arrival of the pump pulse at t_{begin}= 4.065 μs (see Fig. 4.3(a)), the state of impurities is driven out of equilibrium and develops towards a new steady state. In this new state, a complex mixture of carriers is excited based on the intensity and excitation energy of the

pump laser, which results in either an overall increase ($\Delta\alpha > 0$) or a decrease ($\Delta\alpha < 0$) of the probe laser absorption. Furthermore, the rate of change from the old to the new steady state relies on the sum of the contributions arising from the individual carriers. After the end of the pump pulse at t_{end}= 6.065 μs, the probe absorption reverts to the old steady state within a few tens of microseconds.

To demonstrate both scenarios, i.e. $\Delta\alpha > 0$ and $\Delta\alpha < 0$, we spectrally position the probe and pump laser in the following two configurations. In the first case, the probe energy at $n_{probe} = 10P$ is below the pump energy at $n_{pump} = 14P$, i.e. $E_{probe} < E_{pump}$. The corresponding TR traces are shown in Fig. 4.3(b). In the second case, the probe and the pump laser energy are fixed at $n_{probe} = 10P$ and $n_{pump} = 9P$, respectively, i.e. $E_{probe} > E_{pump}$. These TR traces are depicted in Fig. 4.3(c). In both configurations, the pump laser intensity (I_{pu}) is set to three different intensities: 10 (low), 250 (intermediate) and 998 mW /cm^2(high), while the probe intensity (I_{pr}) is constant and set to 1.39 mW /cm^2. The method used to estimate the laser intensities is given in appendix 6.

In the low-intensity regime (black curve), the crystal shows an increase in absorption (i.e. $\Delta\alpha > 0$) when $E_{probe} < E_{pump}$ (Fig. 4.3(b)) as opposed to a reduction in absorption (i.e. $\Delta\alpha < 0$) when $E_{probe} > E_{pump}$ as shown in Fig. 4.3(c). This observation agrees with the CW measurements demonstrated in the previous chapter in Fig. 3.6. The origin of the purification process is from the high-n RE [8, 38] . The drop of absorption in the low-intensity regime is believed to stem from the photo-ionization of neutral impurities inherent to the crystal. This is referred to as positive purification [8]. In each of these cases, the relaxation dynamics after the pump pulse are completely different from the dynamics of the onset of the changes during the presence of the pump pulse.

For the intermediate intensity regime (red curve), in both cases $E_{probe} < E_{pump}$ and $E_{probe} > E_{pump}$, we observe an additional process on top of purification that causes a reduction in absorption. This process exhibits both an instantaneous onset and decay, indicating that its dynamics are faster than the temporal resolution of our setup. Such an instantaneous process may originate from either Rydberg blockade [39] or plasma blockade [33] as discussed in chapter 2, section 2.4 and 2.5. The intricate temporal evolution, as depicted by the red curves of both Fig. 4.3(b) and (c), results from the complex interplay between the slow purification process and the instantaneous Rydberg or plasma blockade.

In the high-intensity regime (green curve), a reduction of absorption ($\Delta\alpha < 0$) is observed for both cases, albeit it is stronger when $E_{probe} < E_{pump}$ compared to $E_{probe} > E_{pump}$. In the former case, the typical purification process reverses its sign, i.e. $\Delta\alpha$ becomes negative, akin to the latter case. In both scenarios, the relaxation consists of slow and instantaneous decays, which may stem from positive purification or Rydberg and plasma blockade, respectively. The horizontal grey dashed lines in both Fig. 4.3(b) and (c) indicate the max-

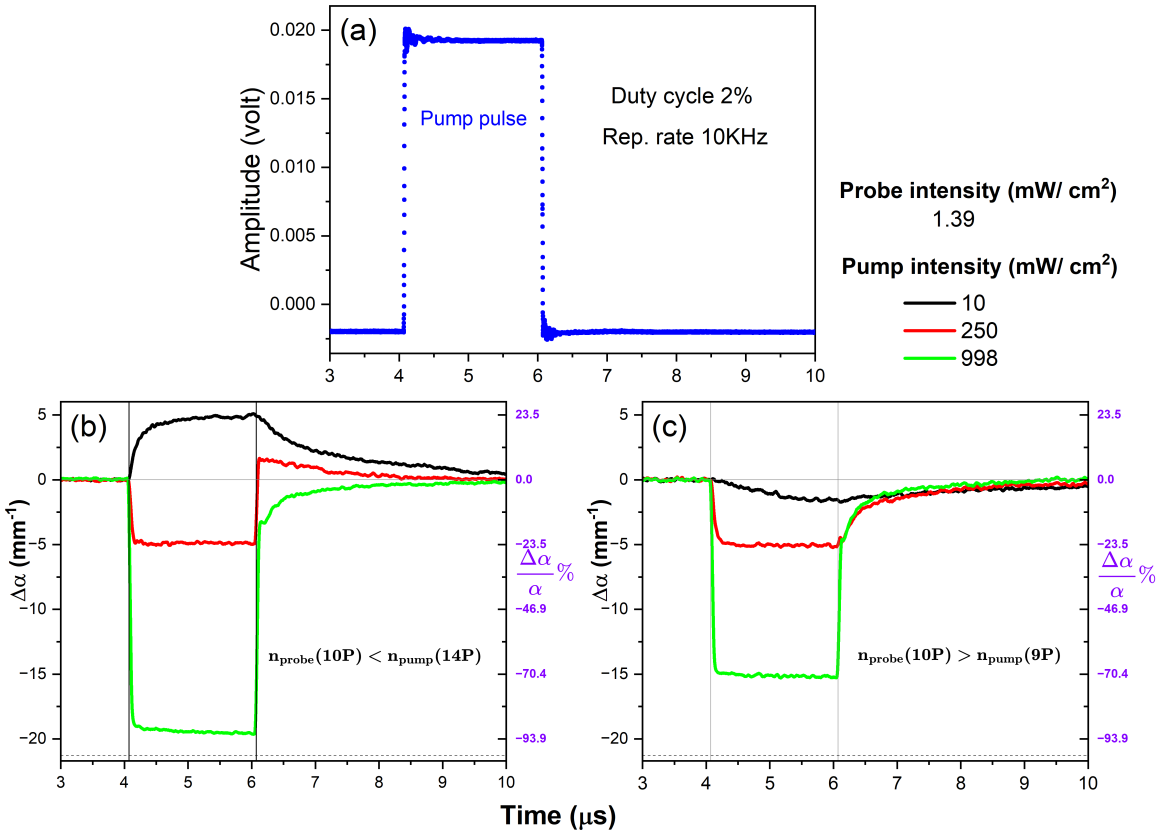

Figure 4.3: (a) Pulse of the pump laser with temporal width 2 μsand repetition rate 10 kHz, generated using an Electro-optic modulator (EOM). In the lower panel, TR traces of the change in probe absorption $\Delta\alpha$ are shown at two different settings of the probe and the pump laser energy: (b) $n_{probe}(10P) < n_{pump}(14P)$ and (c) $n_{probe}(10P) > n_{pump}(9P)$. For each scenarios, three different pump laser intensities (I_{pu}) are demonstrated: 10 (black), 250 (red) and 998 mW /cm^2(green), while the probe intensity (I_{pr}) is always set to 1.39 mW /cm^2. Traces are smoothed for better visual clarity. (b) At low I_{pu} (black), the crystal is purified of charged impurities leading to the probe absorption enhancement. Then, at intermediate I_{pu} (red), blockade sets in on top of purification, resulting in an overall reduction of absorption. Both purification and blockade can be distinguished by their relaxation time scale after the pump pulse ends. Purification exhibits a longer relaxation time compared to blockade, which is almost instantaneous (resolution limited) in our case. At high I_{pu}, along with blockade, positive purification is observed with a long relaxation time, albeit $\Delta\alpha$ is negative. (c) In contrast to (b), absorption is reduced in the presence of a pump pulse for all I_{pu}, although the relaxation times differ. The relaxation is long at low and intermediate I_{pu}, indicating impurity-dominated interactions. At high I_{pu}, an additional instantaneous decay is observed along with a long decay.

imum possible change in absorption coefficient, i.e. $\Delta\alpha$= -21.34 mm^{-1}. At this point, the probe resonance is completely bleached out, and the band gap crosses the resonance energy, a phenomenon often referred to as the Mott transition [33, 98].

4.1.2 Fitting time-resolved traces

This chapter primarily focuses on the dynamics of the purification process. Therefore, the energy of the pump laser is always chosen to be greater than that of the probe laser, i.e. $E_{pump} > E_{probe}$. Furthermore, the intensity of both lasers is kept low enough to get maximal purification of the crystal. The black and orange curves in Fig. 4.4(a) exemplify typical transients of purification at two different probing scenarios: $n_{probe} = 10P$ and $12P$, while the pump laser is set to $16P$. With the arrival of the pump pulse at time t_{begin}= 4.065 μs, the crystal shows enhancement of absorption (i.e. $\Delta\alpha > 0$), changing from the old steady state to a new one. After the end of the pump pulse at t_0= t_{end}= 6.065 μs, the crystal environment begins to revert to its old steady state through several relaxation channels taking place on different timescales.

To understand the mechanism behind purification, we choose to analyse the decay of signal $\Delta\alpha$ using a unique fitting routine. We found that there are primarily five relaxation channels involved, which are shown in purple, red, blue, green and cyan lines in Fig. 4.4(b), respectively. These relaxation channels indicate the presence of five distinct underlying processes contributing to the total probe absorption change ($\Delta\alpha$) during purification. The following formula is used to fit the total $\Delta\alpha$ during the relaxation process

$$\begin{aligned}\Delta\alpha = \Delta\alpha_0 + A_1 e^{-\left(\frac{t-t_0}{t_1}\right)} + A_2 e^{-\left(\frac{t-t_0}{t_2}\right)} \\ + A_3 e^{-\left(\frac{t-t_0}{t_3}\right)} + A_4 e^{-\left(\frac{t-t_0}{t_4}\right)} + A_5 e^{-\left(\frac{t-t_0}{t_5}\right)}.\end{aligned} \tag{4.2}$$

Here, $\Delta\alpha_0$ represents an offset accounting for the non-zero background noise. t is time and $t_0 = 6.065\ \mu s$ is the time when the pump pulse ends. A_1 is the amplitude corresponding to the relaxation process with a time scale t_1, which is near the resolution limit (15 ns). A_2 to A_5 are the amplitudes associated with the relaxation timescales t_2 to t_5, respectively. In this chapter, we will focus on discussing the rates of different relaxation processes instead of their timescales. The relaxation rates R_1 to R_5 are inversely proportional to the timescales t_1 to t_5, respectively.

The amplitudes A_1, A_2, A_4 and A_5 have positive signs, indicating that they correspond to the neutralization or screening of the charged impurities, thereby reducing the stray electric field inside the crystal. On the other hand, A_3 has a negative sign, which may stem from the net photo-induced ionization of neutral impurities, signifying its role in the decrease of

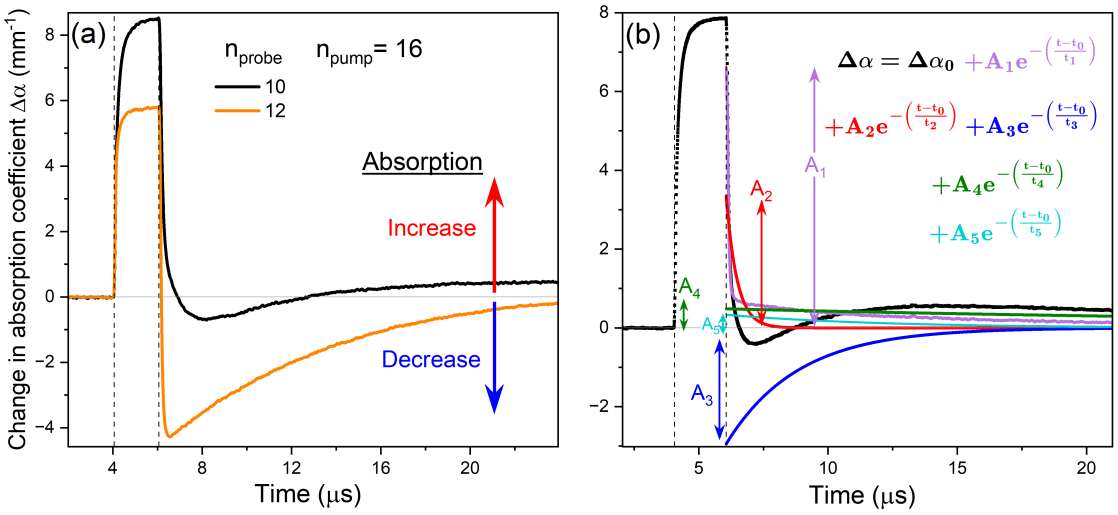

Figure 4.4: (a) Demonstration of purification dynamics. The change of absorption coefficient ($\Delta\alpha$) with time, upon arrival of a pump pulse for 2 μs for $E_{probe} < E_{pump}$. The pump laser resonantly excites 16P excitons, while the probe laser is set to n= 10 (black) and 12 (orange) resonances. The intensities of the pump and probe lasers are 6.98 and 3.47 mW /cm^2, respectively. (b) The system reverts towards the steady state via five different relaxation channels, indicating a total of five underlying physical processes contributing to purification. The relaxation channels are distinguished using an exponential fitting routine Eq. 4.2. The relaxation processes observed are as follows: the fastest relaxation (purple) has a time scale t_1 limited by the resolution (15 ns) of the experimental apparatus and has maximum amplitude (A_1). The other four relaxations as shown in red, blue, green and cyan lines, have relaxation times t_2 to t_5, and amplitudes A_2 to A_5, respectively. The amplitudes are evaluated at the end of the pump pulse (t_{end}). They are indicated using double-headed arrows with respective colours. A positive sign of $\Delta\alpha$ denotes an increase in absorption, whereas a negative sign indicates a decrease.

absorption.

4.2 Pumping at energies near the bandgap

In the previous chapter 3, we found that the absorption of the probe laser is maximally enhanced when the pump laser energy is close to the shifted bandgap $\tilde{E}_g = 2.1719034$ eV and at a suitable intensity which is low. To thoroughly comprehend the underlying intricate processes that result in the maximal purification, we focus here on the complex temporal evolution of $\Delta\alpha$ using a pulsed pump laser. Each panel in Fig. 4.5 depicts the TR traces for states with different probe principal quantum numbers n_{probe}. The intensity of the probe laser (I_{pr}) is constant, set to 6.94 mW /cm^2, while the pump laser intensity (I_{pu}) is slightly adjusted from panel to panel to achieve maximum purification. The n_{probe} and I_{pu} for

each panel are different, with the exact values shown in each panel. We evaluate the TR traces during the presence and aftermath of the pump pulse. Both scenarios are discussed separately in the following.

During the presence of the pump pulse, the absorption for all n_{probe} is enhanced, i.e. $\Delta\alpha > 0$. We observe a multi-exponential growth of the signal $\Delta\alpha$ with time until the end of the pulse. The overall maximum change of absorption ($\Delta\alpha_{max}$) increases from n_{probe}= 7 to 10 as shown in panels (a), (b), (c) and (d). At the same time, the optimum pump intensity (I_{pu}) used, i.e. 0.24 mW /cm^2, remains the same. For n_{probe}= 7, $\Delta\alpha_{max}$ is 3.93 mm^{-1}, while it achieves its highest value of 8.6 mm^{-1} for n_{probe}= 10. In the case of high-lying Rydberg states beyond 10P, i.e. $n_{probe} > 10$, we observe that the $\Delta\alpha_{max}$ value drops drastically as well as the used I_{pu}. It drops so much so that for n_{probe}= 15, $\Delta\alpha_{max}$ is a mere 0.52 mm^{-1}. The drop of $\Delta\alpha_{max}$ is in agreement with what we observed for CW measurements in Fig. 3.4(b). However, the $\Delta\alpha_{max}$ observed in the CW measurement is at least a factor of three higher than that found for the TR measurement. As an example, for $n_{probe} = 10$, $\Delta\alpha_{max}$ from CW measurement is 23.22 mm^{-1} (see Fig. 3.4), while it amounts to only 8.6 mm^{-1} for theTR measurement. The reason behind this discrepancy is still subject to ongoing research.

After the pump pulse is over, the system reverts towards the steady state, which results in the decrease of $\Delta\alpha$ from $\Delta\alpha_{max}$ to zero. This relaxation process takes a few tens of microseconds. However, for all n_{probe}, the reduction of $\Delta\alpha$ is not monotonic. For low n_{probe} states (upper panel (a), (b) and (c)), we observe a multi-exponential decay. Similarly, for high n_{probe} states (middle and lower panel), $\Delta\alpha$ drops from a positive $\Delta\alpha_{max}$ to a negative value within 200 - 400 ns. The negative amplitude of $\Delta\alpha$ increases from n_{probe}= 10 to 12 achieving a minimum of -3.88 mm^{-1} for n_{probe} = 12 and afterwards starts to drop for high n_{probe} states ($n_{probe} > 13$). Finally, $\Delta\alpha$ returns from a negative to a positive value (i.e. purification) and then levels at zero. The intricate dynamics of $\Delta\alpha$ indicate the involvement of many physical processes with different amplitudes and timescales.

To quantitatively compare different processes, we segregate the component relaxation channels using Eq. 4.2 and the methods mentioned in the previous section. The results are shown in Fig. 4.6. Panels (a) and (b) show the amplitudes and relaxation times of different constituent processes as a function of n_{probe}. The amplitudes are evaluated as a change in $\Delta\alpha$ at the end of the pump pulse.

The black dots in panel (a) are the total amplitudes, which increase from a value of 3.93 mm^{-1} for $n_{probe} = 7$ to a maximum of 8.5 mm^{-1} for $n_{probe} = 10$, and finally drop close to zero for $n_{probe} = 16$. Similarly, A_1 (purple) and A_2 (red) increase from values of 0.3 and 1.1 mm^{-1} for $n_{probe} = 7$ up to a maximum value of 7.57 and 5.9 mm^{-1} at around $n_{probe} = 9$ to 11, respectively. Eventually, A_1 and A_2 reduce to zero for $n_{probe} = 16$. A_3

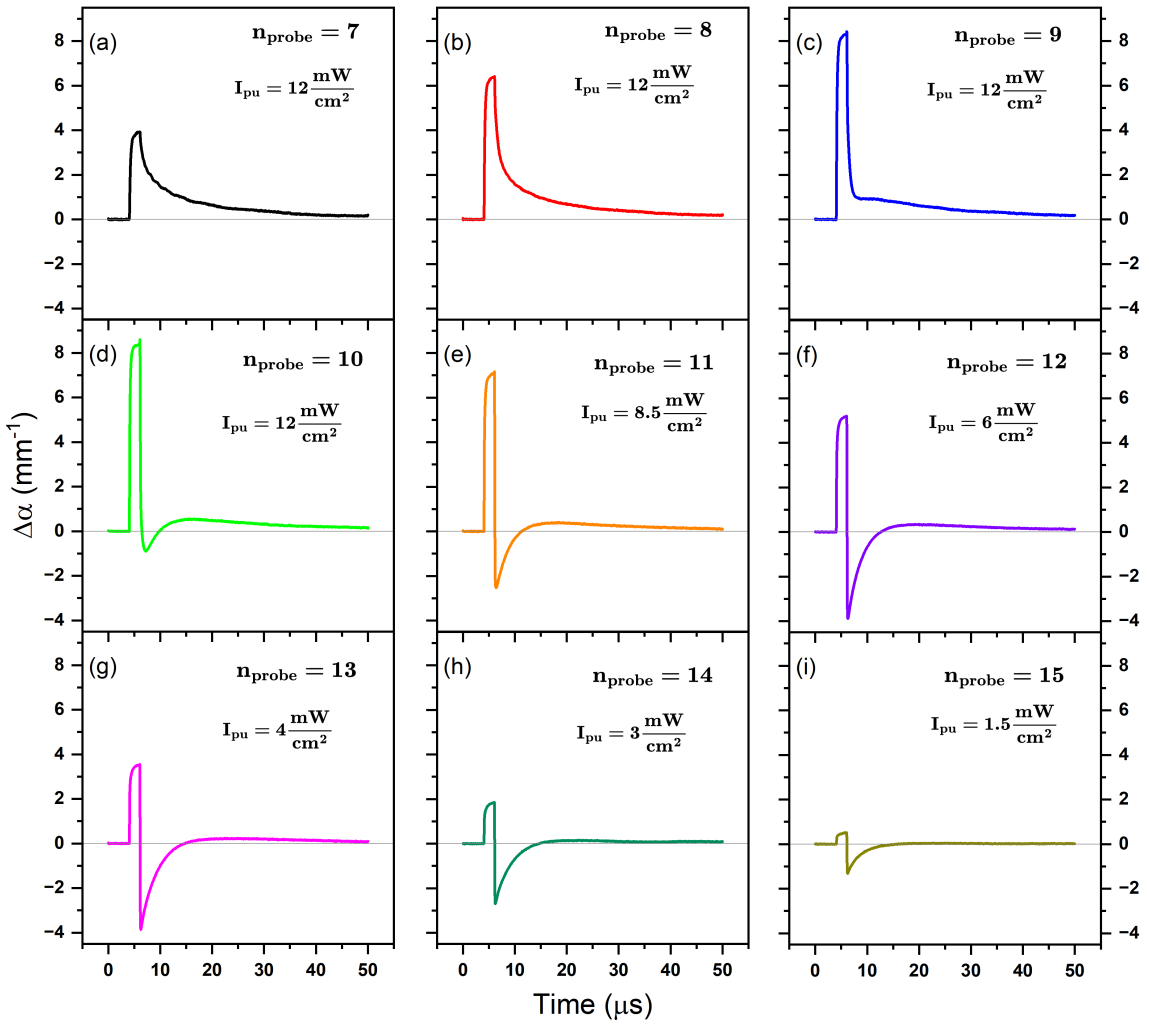

Figure 4.5: Each panel from (a) to (i) depicts the TR trace for a particular n_{probe} from 7 to 15P, respectively. The pump laser energy is always fixed close to the shifted bandgap ($\tilde{E}_g$) at 2.1719034 eV, as found in chapter 3. The probe intensity (I_{pr}) is 6.94 mW /cm^2, while optimum pump intensities (I_{pu}) are utilised for different n_{probe} to achieve maximum purification. In the presence of the pump pulse, all n_{probe} show enhancement of absorption (i.e. $\Delta\alpha > 0$). The maximum $\Delta\alpha$ increases from $n_{probe} = 7$ up to 10P, reaching the highest 8.6 mm^{-1}, and starts dropping after 10P. During the relaxation process, for low n_{probe} (upper panel (a), (b) and (c)), $\Delta\alpha$ always remains positive before monotonically decreasing to zero in a few tens of microseconds. However, for high n_{probe} (middle and lower panels), $\Delta\alpha$ becomes negative within 200 - 400 ns and then rises to values positive before reaching zero. This indicates a trade-off between different inherent processes contributing to the overall $\Delta\alpha$, based on the parameters of the pump and probe.

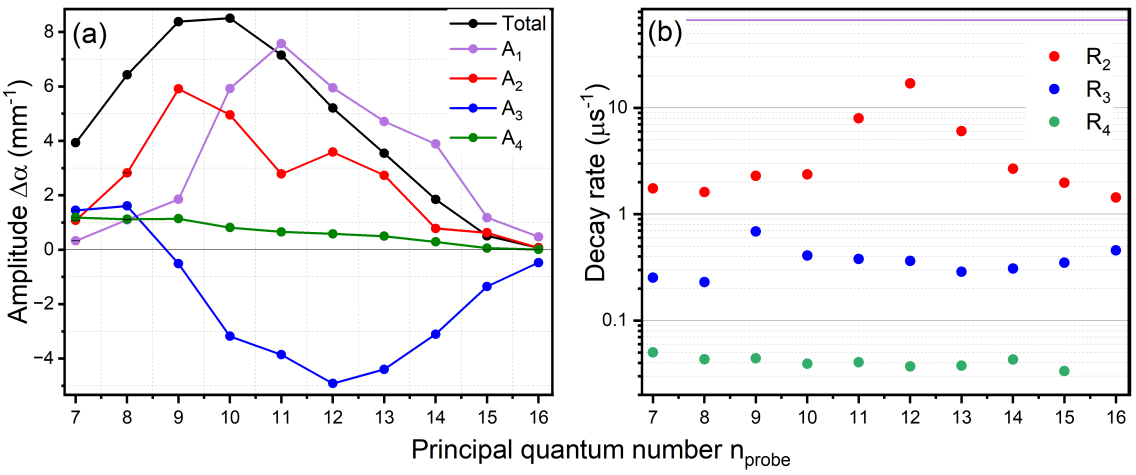

Figure 4.6: (a) Amplitudes of constituent relaxation channels as a function of the principal quantum number of probe exciton (n_{probe}), of the TR traces shown in Fig. 4.5. Black dots represent the total amplitude, while purple, red, blue and green dots represent the amplitudes from A_1 to A_4, respectively. (b) Rates R_2 to R_4 are related to the amplitudes A_2 to A_4, respectively. The timescale corresponding to the rate R_1 (horizontal purple line) lies within the resolution limit, i.e. 15 ns.

(blue) reduces from a positive $\Delta\alpha$ value of 1.44 mm^{-1} for $n_{probe} = 7$, to a minimum value of -4.91 mm^{-1} for $n_{probe} = 12$, and then grows to zero. A_4 (green) has a maximum value of 1.18 mm^{-1} at $n_{probe} = 7$, which monotonically approaches zero at $n_{probe} = 16$.

The relaxation rates R_2, R_3 and R_4 are plotted in Fig. 4.6(b) as red, blue and green dots. R_2 varies between 2 and 20 μs^{-1}, and has a maximum value at $n_{probe} = 12$. R_3 lies in the range of 0.2 - 0.8 μs^{-1}, while R_4 is 0.02 - 0.06 μs^{-1}. The time scale related to R_1 is below the resolution limit, i.e. 15 ns, indicated using a purple horizontal line.

The origin of these four relaxation mechanisms are discussed in detail in the following section.

4.3 Probe intensity dependence

While studying the purification dynamics, we primarily focus on and analyze the relaxation of the signal $\Delta\alpha$ after the end of the pump pulse, where only the continuous wave probe laser is present. Thus, to understand the origin of the constituent underlying physical processes contributing to the overall purification, it is imperative to investigate how these processes depend upon the probe laser intensity (I_{pr}). Here, in this section, we vary the intensity of the probe laser while the pump laser is fixed to a low intensity of $I_{pu} = 6.98$ mW /cm^2. At each I_{pr}, we acquire a TR trace and perform a comprehensive analysis of each of the five relaxation channels. n_{probe} and n_{pump} are set to $10P$ and $16P$ exciton resonances,

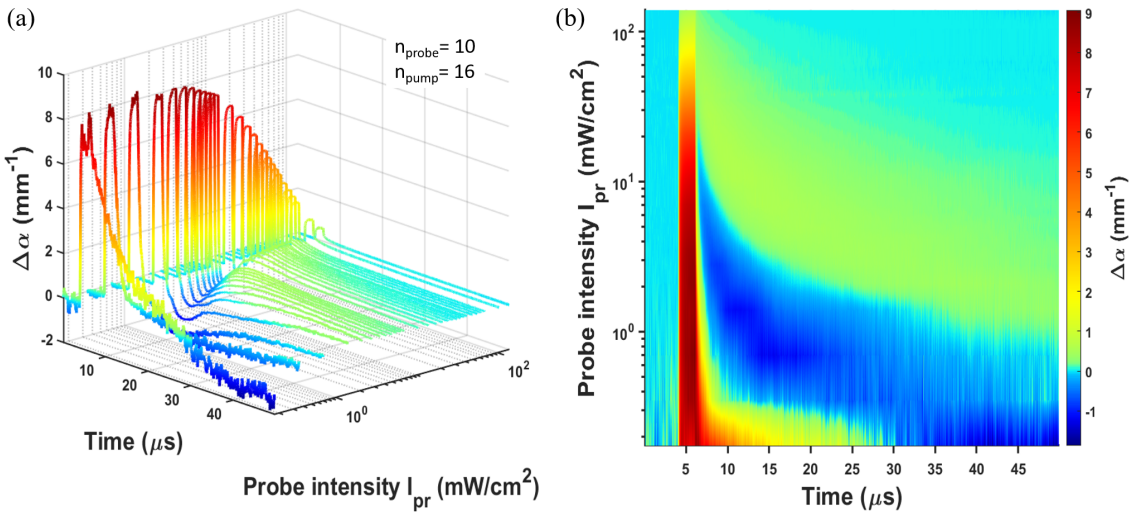

Figure 4.7: (a) Waterfall plot of TR traces for a series of probe laser intensities (I_{pr}), while the pump laser intensity (I_{pu}) is set to 6.98 mW /cm^2. The n_{probe} and n_{pump} are set to $10P$ and $16P$ exciton resonances, respectively. During the presence of the pump pulse, the probe absorption is enhanced to a maximum ($\Delta\alpha_{max}$). $\Delta\alpha_{max}$ drops with increased probe laser intensity. After the pump pulse is over, the purified new steady state reverts to the old steady state through five different relaxation channels. One of them is instantaneous, while the relaxation rates of the other four relaxation channels increase with an increase in probe intensity. (b) Corresponding two-dimensional plot of panel (a) with intermediate intensities interpolated.

respectively, so that we stay in the purification regime.

Figure 4.7(a) shows a waterfall plot of the complex temporal evolution of $\Delta\alpha$ for varying I_{pr}. At each coordinate, the value of $\Delta\alpha$ is represented by the colour scale depicted on the right side of the plot. Blue colour corresponds to the bleaching of the resonance, while green to deep red colours indicate an enhancement of absorption. When the pump pulse is present, we observe the maximum change in absorption ($\Delta\alpha_{max}$) of $\sim$9 mm^{-1} at low I_{pr}. With increased I_{pr}, $\Delta\alpha_{max}$ drops drastically, and the purification process becomes less efficient. Potential reasons for this effect include an increase in self-Rydberg blockade among probe excitons [51] or asymmetric Rydberg blockade between pump and probe excitons [39]. After the end of the pump pulse, we observe the relaxation of the impurity system towards the steady state. Most interestingly, depending on I_{pr}, $\Delta\alpha$ changes from positive to negative and then reverts to positive before returning to zero. We visualize this behaviour as a two-dimensional plot in Fig. 4.7(b), with intermediate I_{pr} values interpolated.

We again dissect and analyze the component relaxation channels using the fitting method and the formula (Eq. 4.2) as given in section 4.1.2. Figure 4.8(a) illustrates the correspond-

ing amplitudes $\Delta\alpha$ of all the relaxation channels at $t_{end} = 6.065\ \mu s$ (end of the pump pulse) as a function of I_{pr}. Black dots show the total amplitude. It drops exponentially with an increase in I_{pr}. The purple, red, blue, green and cyan dots represent A_1 to A_5, respectively, which also drop exponentially with increasing I_{pr}. Among these, A_3 has the fastest drop rate with I_{pr}, followed by A_1 and A_2.

In the right panel (b), the relaxation rates of all channels are plotted as a function of I_{pr}. The rate R_1, shown as a purple-coloured horizontal line, shows dynamics below the resolution limit (15 ns) of the experimental apparatus used here. The rates R_2 to R_5 are shown in red, blue, green and cyan, and plotted as a function of I_{pr}. Notably, R_2 and R_3 increase linearly with I_{pr}, while R_4 and R_5 follows a fourth and square root dependence, respectively. Overall, since both the amplitudes and relaxation rates vary with changing I_{pr}, it can be concluded that the underlying physical mechanisms are not spontaneous but instead driven by the probe laser. In the following, we discuss the model proposed by Bergen et al. [8] to describe the dynamics and speculate the potential origin of the underlying relaxation channels and corresponding physical mechanisms.

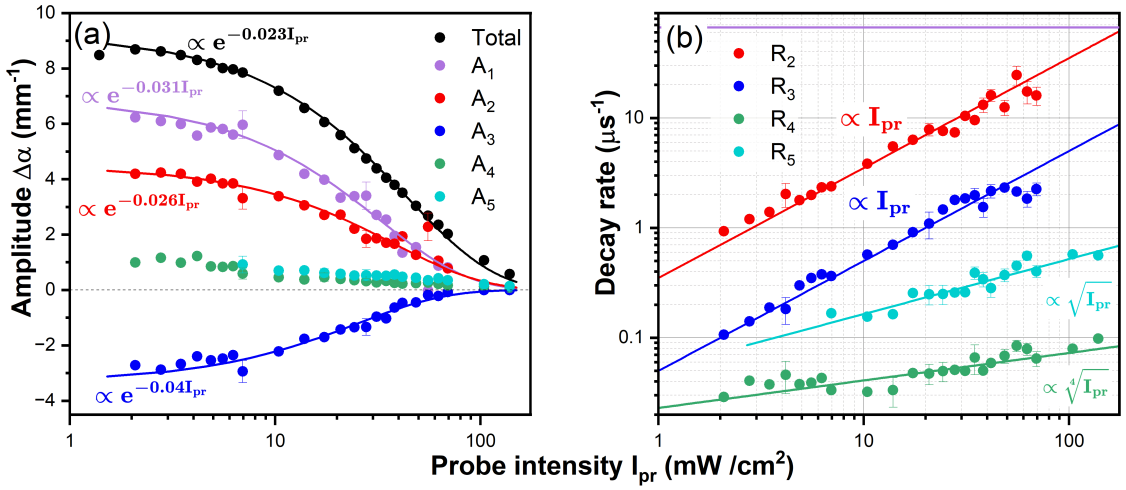

Figure 4.8: (a) Amplitudes of both the overall and different constituent relaxation channels present in the TR traces of Fig. 4.7, as a function of the probe laser intensity (I_{pr}). Black dots represent the overall amplitude, while purple, red, blue, green and cyan dots represent its constituent amplitudes A_1 to A_5, respectively. An exponential drop is observed for all the amplitudes, as indicated by the fitted lines with respective colours. (b) Relaxation rates as a function of I_{pr}. R_2 (red), R_3 (blue), R_4 (green) and R_5 (cyan) are the rates related to the amplitudes A_2, A_3, A_4 and A_5 respectively. The rate R_1 (purple line) has a timescale below the resolution limit of the experimental setup, i.e. 15 ns. R_2 and R_3 linearly increase with I_{pr}. The increase of R_4 and R_5 show a quadratic and square root dependence.

4.3.1 Inference of relaxation mechanisms

Bergen et al. [8] proposed a phenomenological model which describes the purification mechanism. Due to slow dynamics of purification, it is assumed that the intricate time dependence of $\Delta\alpha$ results from the change in the population of the charge state of the impurities. It further predicts that the relaxation rate depends linearly on I_{pr}. The model is described in the following.

If the total density of impurities in the material is ρ_0, then the density of charged impurities at any given point of time is $\rho_{ion}(t) = \rho_0 p_{ion}(t)$, where $p_{ion}(t)$ is the probability of finding an impurity in its charged state at that time. When a RE is in the vicinity of a charged impurity, it may become trapped by the impurity potential, screen the electric field of the impurity by altering the surrounding dielectric environment or neutralize it. Any of these processes reduce ρ_{ion} in the material. Conversely and simultaneously, the light field of both the pump and the probe laser can photo-ionize a neutral impurity, which results in increasing ρ_{ion} in the material. These two dynamic processes of neutralization of charged impurities by capturing a RE and ionization of neutral impurities by the light field are described by a capture rate r_{cap} and ionization rate r_{ion}. The dynamics of $\dot{p}_{ion}$ are expressed as follows:

$$\dot{p}_{ion} = r_{ion} - (r_{ion} + r_{cap}) p_{ion}. \tag{4.3}$$

Therefore, in the steady state, the probability of finding an impurity in the ionized state is

$$p_{ion,ss} = \frac{r_{ion}}{r_{ion} + r_{cap}}. \tag{4.4}$$

During the pump-probe experiment, the steady state changes twice: first, when the pump pulse begins and second when it ends. Thus, p_{ion} at any given point in time is described as follows

$$p_{ion}(t) = p_{ion,ss,new} - \Delta p_{ion} e^{-(r_{ion,new} + r_{cap,new})t}. \tag{4.5}$$

Here, Δp_{ion} is the difference in the probability of an impurity being in the charged state between the new and the old steady states, i.e. $\Delta p_{ion} = p_{ion,ss,new} - p_{ion,ss,old}$. The sum of the rates is defined as the total rate of relaxation, i.e. $r_{ion,new} + r_{cap,new} = R$. The old steady state is the initial state in the absence of the pump laser, i.e. when only the CW probe laser is present. Even though the intensity of the probe laser is low, it can still neutralize a charged impurity with a capture rate $r_{cap,probe}$ and ionize with $r_{ion,probe}$. In contrast, the new steady state contains both the pump and probe lasers. However, due to the low intensity of the probe laser, the new steady state is mainly defined by the pump pulse. The pump pulse changes the impurity state at a capture rate $r_{cap,pump}$ and ionization rate $r_{ion,pump}$.

Therefore, the charged state of impurities develops from the old to the new steady state with a total rate:

$$R' = r_{cap,pump} + r_{ion,pump}, \tag{4.6}$$

and, after the end of the pump pulse, the charged state of impurities reverts back to the old steady state with a total rate:

$$R = r_{cap,probe} + r_{ion,probe}. \tag{4.7}$$

The rates R' and R can be directly evaluated by separating individual relaxation channels from the TR traces. Moreover, Bergen et al. [8] define the capture rate as

$$r_{cap}(n) = \Gamma_{cap}(n)\, g_0(n)\, I, \tag{4.8}$$

where $\Gamma_{cap}(n) \propto n^{3.5}$ is the capture rate per exciton density, and it depends upon the principal quantum number n of the exciton excited. $g_0(n)$ represents the conversion factor between exciton density and intensities of the lasers used. It is determined by the peak absorption coefficient (α_n), lifetime of the exciton (T_n) and resonance energy (E), given as $g_0(n) = \frac{\alpha_n T_n}{E}$. After the end of the pump pulse, the capture process is driven by the probe laser only. For $n_{probe} = 10$, $g_0(10)$ is found to be around 8.2×10^{-9} cm^{-1}eV^{-1}s using $\alpha_{10} = 54$ mm^{-1}, $E_{10} = 2.171165$ eV and $T_{10} = \frac{\hbar}{\Gamma_{10}} = 33$ ps (for Γ_{10}, see Fig. 3.3(b)).

Similarly, the photo-induced ionization rate is given by

$$r_{ion} = k_{ion} I, \tag{4.9}$$

k_{ion} is the ionization rate per light intensity. In general, photo-ionization can happen in two following ways. Firstly, by the photoelectric effect. Light having an energy larger than the electron binding energy may get absorbed by the electron of a neutral impurity which undergoes to a transition to the conduction band, as shown in Fig. 4.9 (b) [2, 55]. In this process, the electron cannot transit to the lowest laying conduction band as the transition to this band is dipole-forbidden owing to the symmetry of the band. However, the dipole selection rule is locally broken due to the electric field of the impurities, which makes the transition locally allowed. Moreover, the transition to the second lowest conduction band is possible.

Secondly, the light field may tilt the potential barrier of the neutral impurity, facilitating the tunnelling of an electron and thereby driving the impurity towards a charged state. Figure 4.9 (a) illustrates such an optically induced tunnelling effect. However, this process is highly unlikely within the intensity ranges considered here. Moreover, the wavelengths

of both lasers are too short to create a quasi-static electric field, which is essential for such an optical tunnelling effect. For a fast oscillating AC field, such as an electromagnetic wave (light field) below a certain threshold wavelength, the impurity experiences a zero average electric field. The quasi-static nature of a light field can be quantified using the Keldysh parameter (γ), which is given by

$$\gamma = \frac{\omega \left(mE_g\right)^{1/2}}{eE}, \tag{4.10}$$

where E_g is the bandgap and ω is the angular frequency of the driving light. m and e are the mass and charge of an electron, respectively. E is the strength of the electric field of the light, which is related to the intensity as follows: $E = \sqrt{\frac{2I}{cn\varepsilon_0}}$. For the highest light intensity (100 mW /cm^2) used in our case, γ is found to be on the order of $\sim 10^8$. Electron tunnelling becomes likely for $\gamma \ll 1$ [9, 52, 114].

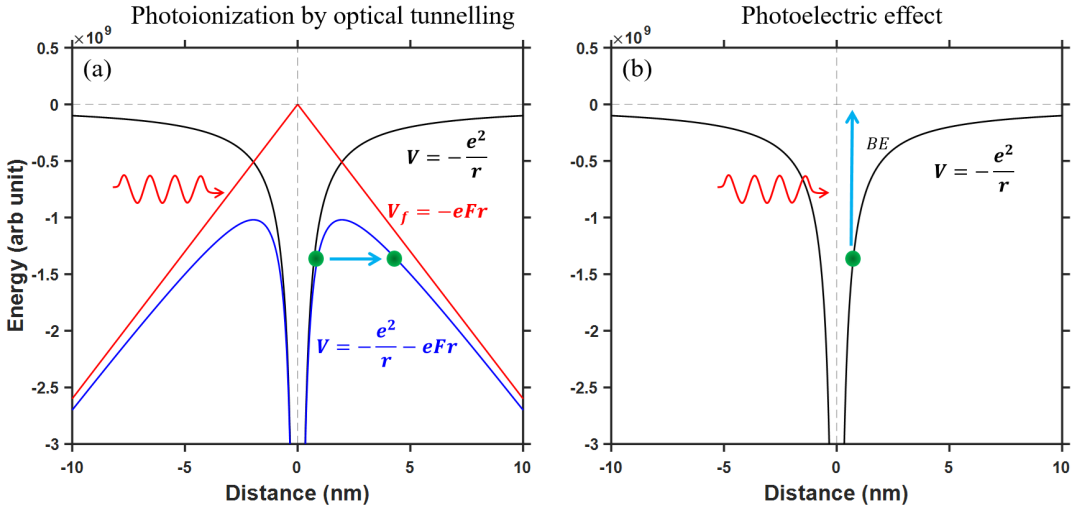

Figure 4.9: Photo-induced ionization of a neutral impurity, via two different processes: (a) A strong light field tilts the potential barrier of a neutral impurity and an electron tunnels away from it, resulting ionization. This effect occurs when the light has high intensity and a relatively long wavelength. (b) by the photoelectric effect, where an electron absorbs a photon with energy higher than its binding energy (BE) and transits to the conduction band.

Both of the above photo-ionization processes can drive a neutral impurity to a charged state and create an equal amount of free electrons above the bandgap.

Combining Eqs. 4.8 and 4.9, the total rate of relaxation (R) can now be expressed as

$$R = \left\{\Gamma_{cap}\left(n_{probe}\right) g_0\left(n_{probe}\right) + k_{ion}\right\} I_{pr}. \tag{4.11}$$

Similarly, from the above Eqs. 4.4, 4.8 and 4.9, one can deduce that,

$$p_{ion,ss} = \frac{k_{ion}}{k_{ion} + \Gamma_{cap}(n)\, g_0(n)}. \tag{4.12}$$

Notably both $\Gamma_{cap}(n)$ and $g_0(n)$ increase with n. Thus, when $n_{pump} > n_{probe}$, $p_{ion,ss}(pump + probe) < p_{ion,ss}(probe)$. This leads to the net reduction of charged impurities, so-called purification. On the other hand, for $n_{pump} < n_{probe}$, $p_{ion,ss}(pump + probe) > p_{ion,ss}(probe)$ is expected, which results in a net increase of charged impurities.

We now return to the discussion of the experimental results presented in the previous section 4.3. First, considering the resolution-limited rate R_1 and the positive amplitude A_1 (purple), the associated physical process is most likely related to a short living species, such as Rydberg excitons. When a Rydberg exciton is excited in the vicinity of a charged impurity, it may screen the stray electric field emanating from the charged impurities, thereby enhancing the absorption of other excitons. In principle, such screening can be induced by RE created by both pump and probe lasers. However, since the probe laser is continuous, the screening by the probe created RE does not change with time. On the other hand, the screening by pump excitons should vanish at the end of the pump pulse. Moreover, excitonic screening does not reduce the density of charged impurities ρ_{ion} inside the material. Instead, it only mitigates the influence of electric field of charged impurities on excitonic absorption.

The rate R_2 (red) increases linearly with I_{pr}, i.e. $R_2 \propto I_{pr}$, which is in agreement with the model discussed above (see, Eq. 4.11). The sign of the related amplitudes A_2 (red) is positive, indicating that the related physical process stems from the net reduction of charge impurities in the crystal. This process may include the simultaneous neutralization of a charged impurity via the capture of an exciton and photo-induced ionization of neutral impurities. The ratio between neutralization and photoionization rate defines the equilibrium density of ρ_{ion}. In the presence of the pump pulse, the rate of exciton capture by charged impurity sites may exceed the photoionization rate of neutral impurities, driving the crystal toward a steady state with a reduced density of charged impurities. However, after the pump pulse ends, the photoionization rate may surpass the neutralization rate.

The rate R_3 (blue) also shows a linear dependence with I_{pr}, i.e. $R_3 \propto I_{pr}$. Although the scaling of R_3 conforms with the model discussed above (see, Eq. 4.11), the sign of the related amplitudes A_3 (blue) is negative. In this case, in the presence of the pump pulse, the crystal develops toward a state with more charged impurities. Considering that the pump laser energy is higher than the probe energy, such a process cannot be explained using the model proposed by Bergen et al. [8]. The microscopic origin of this process remains unclear and is a subject for future investigation.

The slow process with amplitude A_4 (green) may be related to the bound exciton-

impurity complex (BEIC). In theory, the stability of such a bound complex is determined by the ratio of electron and hole mass (m_e/m_h). According to Refs. [93, 95], an exciton-donor impurity complex is possible if $m_h/m_e > 1.41$, while $m_e/m_h > 1.41$ is required to form a bound exciton-acceptor state. In Cu_2O , $m_e/m_h = 1.71$ and $m_h/m_e = 0.58$. Thus, only the formation of a bound exciton-acceptor complex is possible in Cu_2O . In that scenario, an exciton excited in the vicinity of a positively charged impurity gets trapped and forms a meta-stable bound complex. The signatures of such a bound complex are demonstrated in Refs. [44, 82] using photoluminescence (PL) measurements. The PL of bound excitons at energies below the $1S$-ortho resonance is observed. Roger et al. reported lifetimes of such bound excitons up to 640 μs [82].

In our case, Rydberg excitons may get directly trapped at an impurity site or relax to create a small density of $1S$ ortho and para excitons, which in turn get trapped to form a BEIC. Moreover, $1S$ excitons created by direct absorption at phonon background can also be trapped [56, 57]. Subsequently, the bound exciton may recombine, leaving the impurity state as it is.

Lastly, A_5 appears only at high $I_{pr} \geq 10$ mW /cm^2. Considering its positive amplitude A_5 and relaxation rate R_5 which shows as square-root scaling with I_{pr}, it may originate from the screening of charged impurities by the low-density e-h plasma [20, 113]. A detailed investigation of the plasma screening process will be provided in the next section.

In summary, in contrast to Bergen et al. [8], we are now able to identify five interaction mechanisms that lead to the overall purification of the material. We find a total of five channels in the relaxation process whose amplitudes drop exponentially with an increase in the probe laser intensity. Similarly, the corresponding relaxation rates also show an increase with I_{pr}, albeit different scaling laws are observed.

4.4 Influence of e-h plasma on purification

From several previous studies, e.g. Refs. [33, 98], it is well-known that RE are sensitive a surrounding electron-hole plasma. The presence of free charge carriers leads to a lowering of the bandgap, resulting in the ionization of RE into an absorption continuum, a well-known effect referred to as "Mott transition". RE are so sensitive that even a low density of plasma on the order of 0.01 μm^{-3} compels the highest RE to undergo the Mott transition, which is often considered as an unwanted detrimental effect. At the same time, the influence of a plasma on purification has not been studied so far. In this section, we discuss the impact of a low-density e-h plasma on the dynamics of purification.

In the experiment, we use a pulsed pump - CW probe setup along with an additional

CW green (532 nm) laser. Here, the role of the green laser is to create a finite density of e-h plasma through illumination above the bandgap at an energy of 2.3305 eV. The low-intensity pulsed pump laser temporarily purifies the crystal in the presence of an e-h plasma, while the corresponding dynamical changes in the optical properties of the material are evaluated by recording the change in absorption of the CW probe laser. The density of the e-h plasma is changed by varying the intensity of the green laser.

Similar to the previous section, the pump and probe lasers are set to the exciton resonances $16P$ and $10P$, i.e. $n_{pump} = 16P$ and $n_{probe} = 10P$, while their intensities are fixed to 6.98 and 3.47 mW /cm^2, respectively. Additionally, the intensity of the green laser I_{gr} is varied from 0 to 9.08 mW /cm^2. As a reference, Fig. 4.10 demonstrates the TR traces in the absence (black) and presence (red) of e-h plasma excited using a green laser with I_{gr}= 0.14 mW /cm^2. When a plasma is present, $\Delta\alpha_{max}$ is smaller than in the scenario without a plasma. At the same time, $\Delta\alpha$ does not become negative during relaxation, indicating a sign change of A_3, as an influence of the e-h plasma. Furthermore, the influence of a low-density e-h plasma is studied through a series of I_{gr}, which is shown in Fig. 4.10(b) as a two-dimensional plot of several TR traces. The colourmap on the right side denotes the value of $\Delta\alpha$. The critical I_{gr} required to remove the overshooting that makes $\Delta\alpha$ negative is indicated using a black horizontal dashed line.

The amplitudes and relaxation rates of all the four constituent relaxation channels as a function of I_{gr} are presented in Fig. 4.11(a) and (b), respectively. In panel (a), the black dots represent the total $\Delta\alpha$. Similarly, the amplitudes from A_1 to A_4 are denoted by purple, red, blue and green dots, respectively. All amplitudes except A_3, drop to zero from a positive value with increasing I_{gr}. A_3 shows an interesting behaviour. It increases from a minimum of -3.6 mm^{-1} at I_{gr}= 0.002 mW /cm^2 to a maximum of 2.20 mm^{-1} at I_{gr}= 2.27 mW /cm^2 and finally starts to drop. A_3 changes sign at $I_{gr,cr}$= 0.14 mW /cm^2. In panel (b), the relaxation rates are shown as a function of I_{gr}. The relaxation rate R_1 is related to A_1, whose timescale is limited by experimental resolution (15 ns). Thus, R_1 is shown as a horizontal purple line. The other relaxation rates R_2 (red), R_3 (blue) and R_4 (green) remain constant at low I_{gr}, and start to increase with I_{gr} beyond $I_{gr,cr}$. However, the increase does not strictly follow any scaling or power law.

4.4.1 Comparison between the impact of excitons and a plasma on purification

In this subsection, we quantitatively compare the impact of increasing both exciton density and electron-hole plasma density on the purification process, i.e. we investigate how the exciton capture at the impurity site and following re-ionization is influenced by either addi-

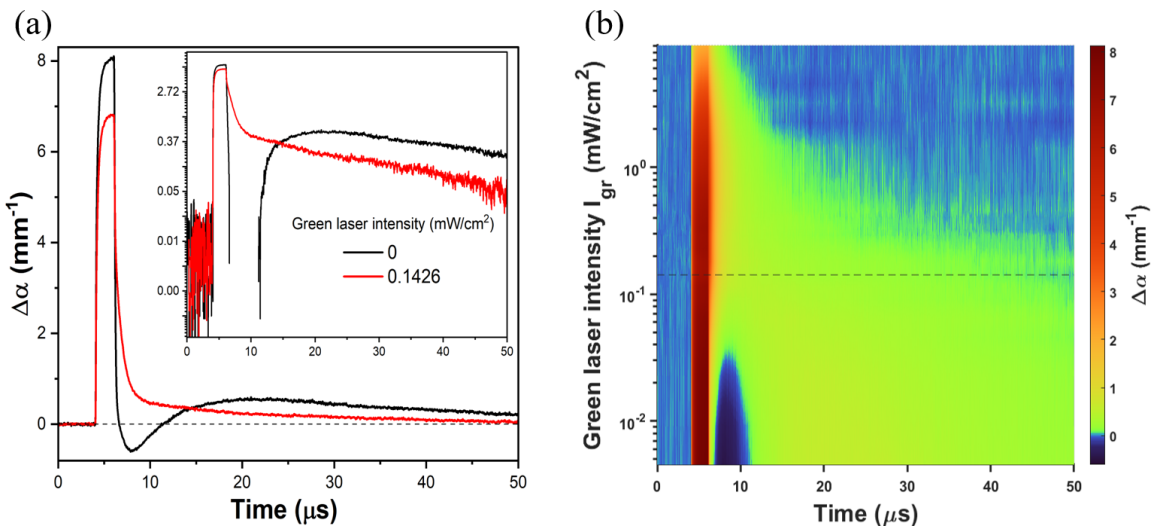

Figure 4.10: (a) Dynamical change of the probe absorption ($\Delta\alpha$) over time, at two different settings: without green laser (532 nm) (black) and with green laser intensity $I_{gr} = 0.142$ mW /cm^2(red). The green laser is used here to create an electron-hole plasma. The probe and pump energies are configured to achieve purification, i.e. $n_{probe}(10P) < n_{pump}(16P)$, with intensities set at 3.47 and 6.98 mW /cm^2, respectively. Due to the presence of a plasma, $\Delta\alpha_{max}$ is reduced during the presence of the pump pulse, and during relaxation, $\Delta\alpha$ does not become negative. This suggests a screening of impurities by the free carriers of the plasma. (b) A 2D plot of the TR traces at a series of I_{gr}. The dashed horizontal line represents the critical I_{gr} at which the change in sign of $\Delta\alpha$ is observed.

tional low-density RE or plasma. Essentially, in the following, we compare the amplitudes and rates of different relaxation channels observed in two previous sections 4.3 and 4.4.

At first, we focus on the total amplitudes and the amplitudes of the different constituent relaxation channels. The amplitudes are always evaluated in terms of $\Delta\alpha$ at the end of the pump pulse. In Fig. 4.12, the amplitude of different individual relaxation processes are shown in separate panels. Unlike the last two subsections, the x-axis is replaced with the intensity absorbed by the crystal for better comparison. The absorbed intensity at a particular excitation energy depends upon the absorption coefficient $\alpha(E)$ and the sample thickness (d), which is defined as follows

$$I(E) = I_0 - I_0 e^{-\alpha(E)d}. \tag{4.13}$$

Here, I_0 is the intensity of the laser at the surface of the sample. The given value for I_0 takes reflections and surface scattering into account.

In figure 4.12, the open dots represent the amplitude as a function of absorbed probe laser intensity $I_{pr,ab}$. The solid dots denote the amplitudes as a function of total intensity ($I_{gr,ab}$) absorbed from two different lasers: a CW probe laser of constant absorbed intensity

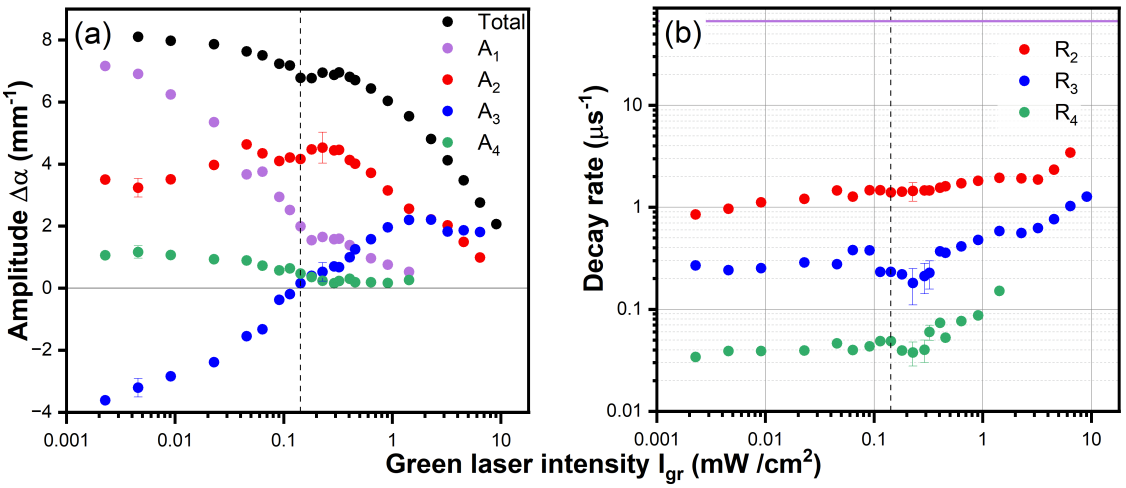

Figure 4.11: (a) Amplitudes of both the overall and different constituent relaxation channels present in TR traces of Fig. 4.10, as a function of green laser intensity (I_{gr}). The black dots represent the overall amplitude, while purple, red, blue and green dots represent its constituent amplitudes A_1 to A_4, respectively. Notably, A_3 changes sign, while others do not. The critical intensity ($I_{gr,cr}$= 0.14 mW /cm^2) at which A_3 changes sign is shown using a vertical dashed line. (b) Relaxation rates as a function of I_{gr}. R_2 (red), R_3 (blue) and R_4 (green) are the relaxation rates related to the amplitudes A_2, A_3 and A_4. R_1 (purple line) has a timescale below the resolution limit of the experiment, i.e. 15 ns.

$I_{pr,0}$ = 2.91 mW /cm^{2}and an additional green CW laser whose intensity $I_{gr,0}$ is varied. The vertical solid grey line indicates the absorbed intensity of the CW probe laser $I_{pr,0}$ = 2.91 mW /cm^2.

In panel (a), the total amplitude as a function of $I_{pr,ab}$ (black empty dots) and $I_{gr,ab}$ (black solid dots) is shown. In both scenarios, we observe the reduction of total amplitude (black dots) with increased light absorption. However, their scaling with intensity differs. An exponential drop is seen with $I_{pr,ab}$, which is shown by a cyan fitted line. On the other hand, a square root-like drop is observed in the case of $I_{gr,ab}$, as depicted by a black fitted line. Furthermore, the four constituent amplitudes A_1 to A_4 are shown in panels (b) to (e), respectively. The influence of the plasma (solid dot) is much stronger than the one from the exciton (open dot) for each relaxation channel. This is evidenced by the steep drop in the amplitudes represented by solid dots. Note that the panels (b), (c) and (e) are shown in a double-logarithimic plot, while A_3 is shown in a semi-logarithimic plot. A_3 which is negative at low $I_{gr,ab}$ changes its sign. It becomes positive and finally drops. On the contrary, A_3 grows from negative values towards zero amplitude, with increasing $I_{pr,ab}$. Overall, no specific scaling laws are found for the amplitudes of different constituent relaxations.

In figure 4.13, we demonstrate the relaxation rates R_2 (a), R_3 (b) and R_4 (c) as a function

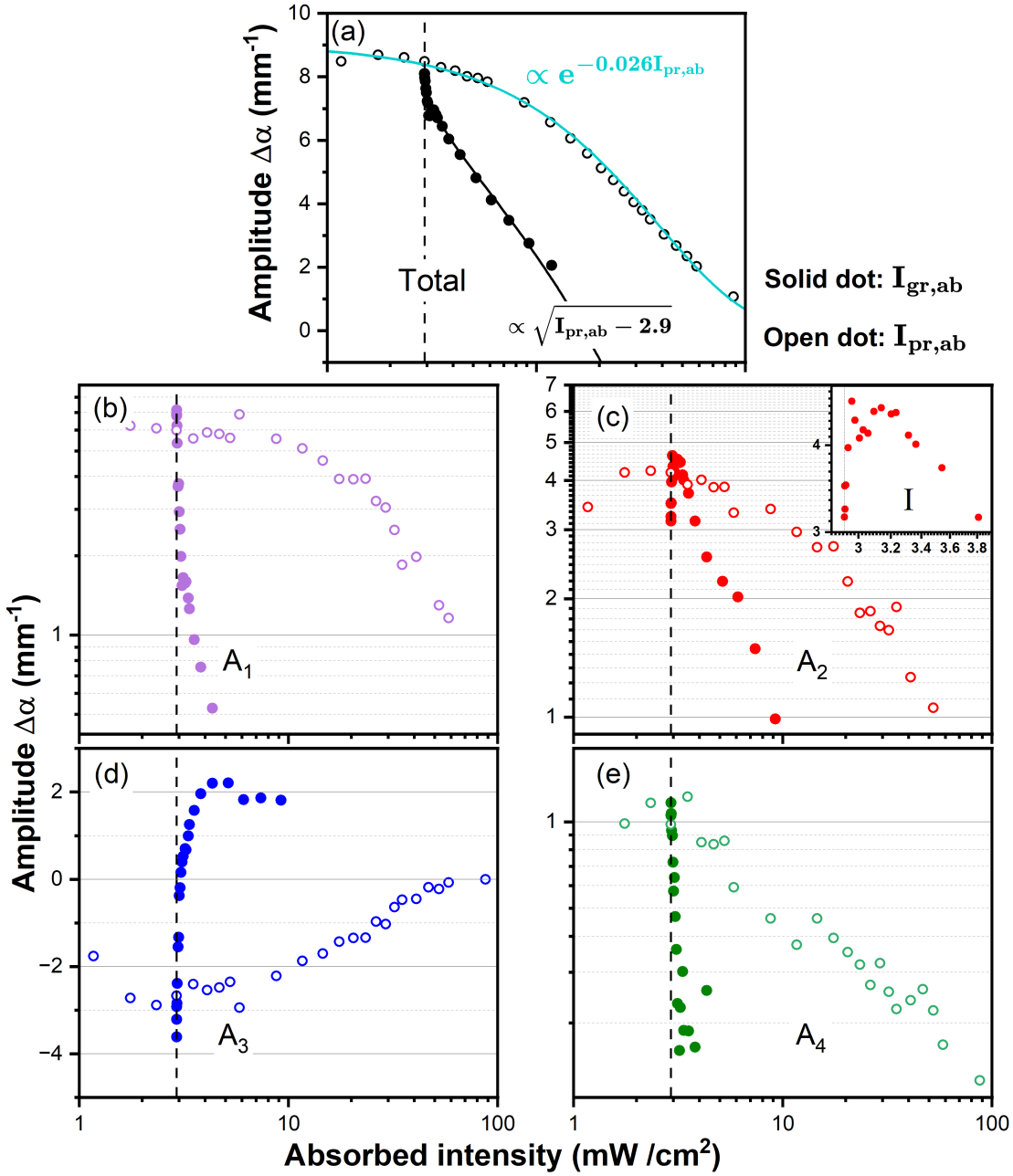

Figure 4.12: Comparison of amplitudes between Fig. 4.8(a) and 4.11(a) as a function of the absorbed intensity (I_{ab}). Solid dots: combined absorption of a probe laser with fixed intensity and varying green laser intensity ($I_{gr,ab}$), and open dots: absorption by varying only probe laser intensity ($I_{pr,ab}$). The black vertical line represents the absorbed intensity without the green laser. (a) The total amplitude drops exponentially with $I_{pr,ab}$, while the drop shows a square root dependence when $I_{gr,ab}$ is increased. The panels (b), (c), (d) and (d) show the amplitudes A_1, A_2, A_3 and A_4 as a function of the absorbed intensities $I_{gr,ab}$ (solid dots) and $I_{pr,ab}$ (open dots), respectively. No particular scaling is observed, albeit the amplitudes drop much faster with the increase in $I_{gr,ab}$ than $I_{pr,ab}$. A_3 changes its sign from negative to positive value with the increase in $I_{gr,ab}$, while it reduces to zero with $I_{pr,ab}$.

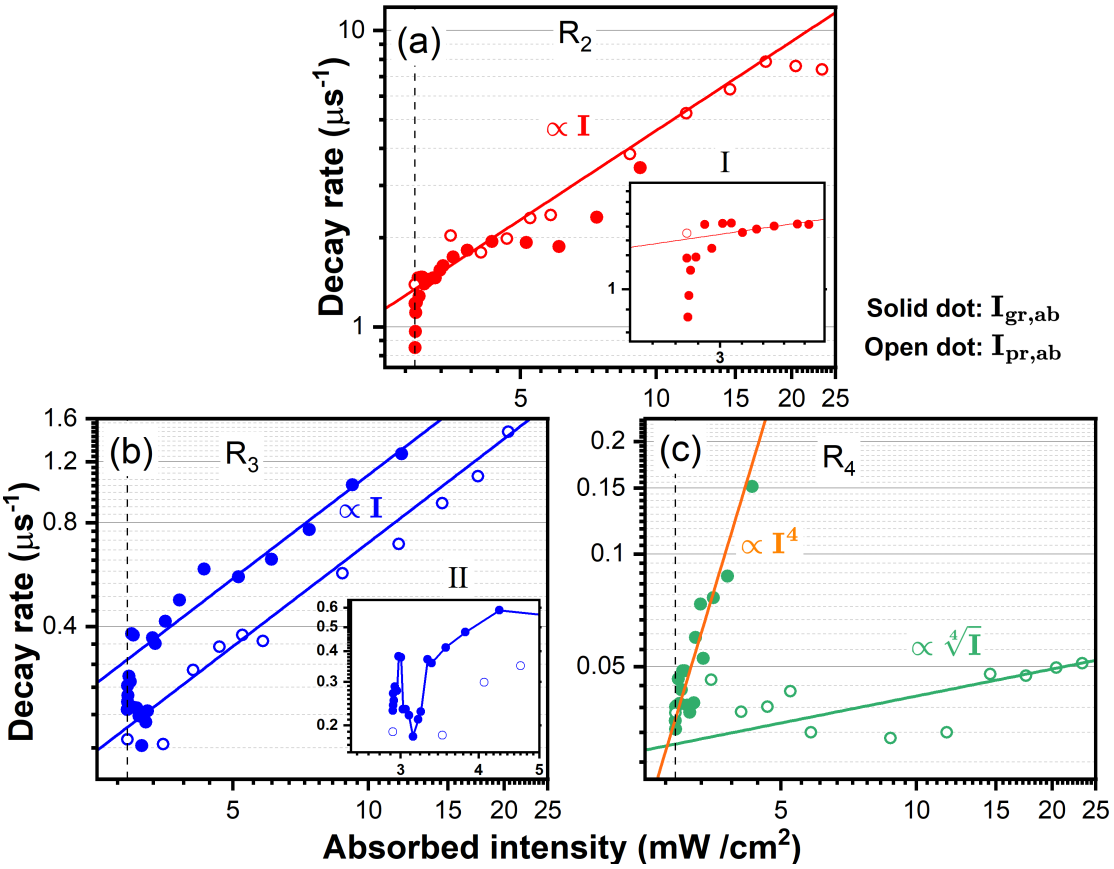

Figure 4.13: (a), (b) and (c) Comparison of rates (R_2, R_3 and R_4) between Fig. 4.8(b) and 4.11(b), as a function of the absorbed intensity. See Fig. 4.12 for the definition of absorbed intensity and meaning of solid and open dots. All rates R_2, R_3 and R_4 increases with $I_{pr,ab}$ and $I_{gr,ab}$. R_2 and R_3 increases linearly with $I_{pr,ab}$, while R_4 depicts a fourth root dependence. Conversely, at low $I_{gr,ab}$, R_2 and R_3 abruptly increases which is shown in insets. At high $I_{gr,ab}$, all rates R_2 and R_3 increases linearly. R_4 grows quadratically with $I_{gr,ab}$.

of the absorbed intensity $I_{pr,ab}$ (empty dots) and $I_{gr,ab}$ (solid dots). The rate of all three relaxations increases with both $I_{pr,ab}$ and $I_{gr,ab}$. R_2 and R_3 increase linearly with $I_{pr,ab}$, while R_4 shows a fourth root dependence. Similarly, at low $I_{gr,ab}$, R_2 (inset I) and R_3 (inset II) show a steep increase up to 50% and afterwards a linear increase. Such a steep increase of R_2 and R_3 may stem from the enhanced capture rate of free carriers at the impurity sites.

R_4 shows a fourth root dependence with the increase in $I_{pr,ab}$. As already discussed, it might be related to the bound exciton-impurity complex. On the other hand, R_4 increases quadratically with $I_{gr,ab}$. The origin of the enhanced relaxation rate at low plasma density $I_{gr,ab}$ is still unknown and a matter of ongoing investigation.

4.5 Purification at non-resonant excitation

In the previous chapter 3, Fig. 3.2, it is observed that along with the purification of crystal, the excitonic absorption becomes enhanced, and the excitonic resonances become sharper due to the increase in oscillator strengths and narrowing of linewidths. At the same time, the absorption peak of the exciton resonance is shifted towards higher energy (blue-shift) due to the reduction of the Stark effect originating from the ambient inhomogeneous electric field of the charged impurities. Thus, it is imperative to study the dynamics of purification across exciton resonances.

In this section, we discuss the dynamical change of probe absorption as a function of finite detuning of the probe laser from the peak of $10P$ resonance, while the pulsed pump laser is always fixed at the $16P$ resonance. The intensities of the pump (I_{pu}) and probe (I_{pr}) lasers are set to 6.98 and 3.47 mW /cm^2, respectively. These intensities are deliberately chosen to obtain maximal purification. As a reference, a three-dimensional waterfall plot of a series of TR traces at different probe detuning is shown in Fig. 4.14(a). The corresponding colour map is given on the right side in panel (b).

The dynamics can be separated into two temporal regimes for better understanding: the first regime covers the time window during the presence of the pump pulse for 2 μs. The second regime covers the relaxation of signal $\Delta\alpha$ after the pump pulse is over. In the following, both time windows are individually discussed and compared.

As mentioned before, the CW probe laser creates a steady state with a certain population density of charged and neutral impurities. During the presence of a pump pulse, the crystal is temporarily driven to a new steady state with an altogether different impurity density. The new steady state can have either more charged or neutral impurities based on the intensity and energy of both pump and probe lasers. In Fig. 4.14(a), the new steady state (between time 4.065 - 6.065 μs) displays dissimilar characteristics in two different ranges of detunings. Firstly, in the detuning range between -13 to 13 μeV, we observe an enhancement of probe absorption ($\Delta\alpha > 0$) up to a maximum of 7.5 mm^{-1}. Moreover, the maximal change in absorption at the $10P$ exciton resonance (middle dashed line in Fig. 4.14(b)) is shifted to higher energy by 5 μeV. This is a clear indication of a decrease in Stark shift induced by the stray electric fields and, accordingly, an enhanced probability of finding impurities being in the neutral state. On the other hand, in the detuning range between -40 to -13 μeV and 13 to 40 μeV, we observe a reduction of probe absorption ($\Delta\alpha < 0$) as shown in blue. In these detuning ranges, the minimum values of $\Delta\alpha$ are -0.8 and -1.4 mm^{-1}, respectively. Notably, the minimum values are observed near the resonances $10S$ and $10F$, as indicated using vertical black dashed lines at detunings of -34 and 24 μeV in Fig. 4.14(b).

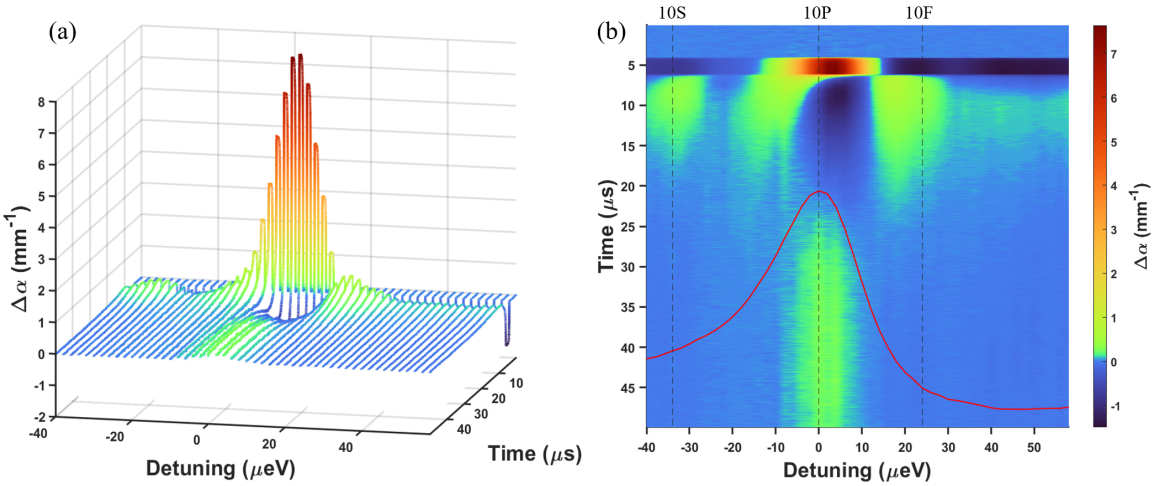

Figure 4.14: (a) Three-dimensional mesh plot of the dynamical change in probe absorption at a series of finite probe laser detuning from the absorption peak of the resonance $10P$ (n_{probe}), while pump laser is fixed at $16P$ (n_{pump}). The peak of resonances is evaluated from the absorption spectrum (e.g. Fig. 3.2). The intensity of the pump (I_{pu}) and the probe (I_{pr}) laser are set to 6.98 and 3.47 mW /cm^2, respectively. The corresponding colour map for $\Delta\alpha$ is shown on the right. A positive value of $\Delta\alpha$ represents the increase in absorption, and vice versa for negative $\Delta\alpha$. (b) 2D mapping of the 3D plot (a), with simulated temporal dynamics at intermediate detunings. The vertical grey dashed lines from left to right represent the spectral positions of $10S$, $10P$ and $10F$ exciton resonance peaks, respectively. The broad red curve represents the peak of $10P$ exciton absorption. During the presence of a pump pulse, the peak of resonance $10P$ is blue-shifted by 5 μeV, indicating the reduction of the Stark shift due to large-scale neutralization of the electric field stemming from the charged impurities.

After the end of the pump pulse at 6.065 μs, the crystal system reverts to the old steady state during a timescale which strongly depends upon the probe detuning. In the detuning range -13 to 13 μeV, $\Delta\alpha$ becomes negative within a few hundred nanoseconds and reverts to a positive value before reaching zero. Overall, it takes tens of microseconds for the crystal to reach the old steady state. On the other hand, at energies below -13 and above +13 μeV, $\Delta\alpha$ is positive for around 15 μs until it reaches zero. The green patches represent regions where we observe an enhancement of absorption ($\Delta\alpha > 0$) up to a maximum of 1 mm^{-1}.

To understand the complex specimens excited and the relaxation of their population, we compare amplitudes and relaxation rates of various associated relaxation channels by dissecting them using Eq. 4.2. In the following sections, both parameters are discussed.

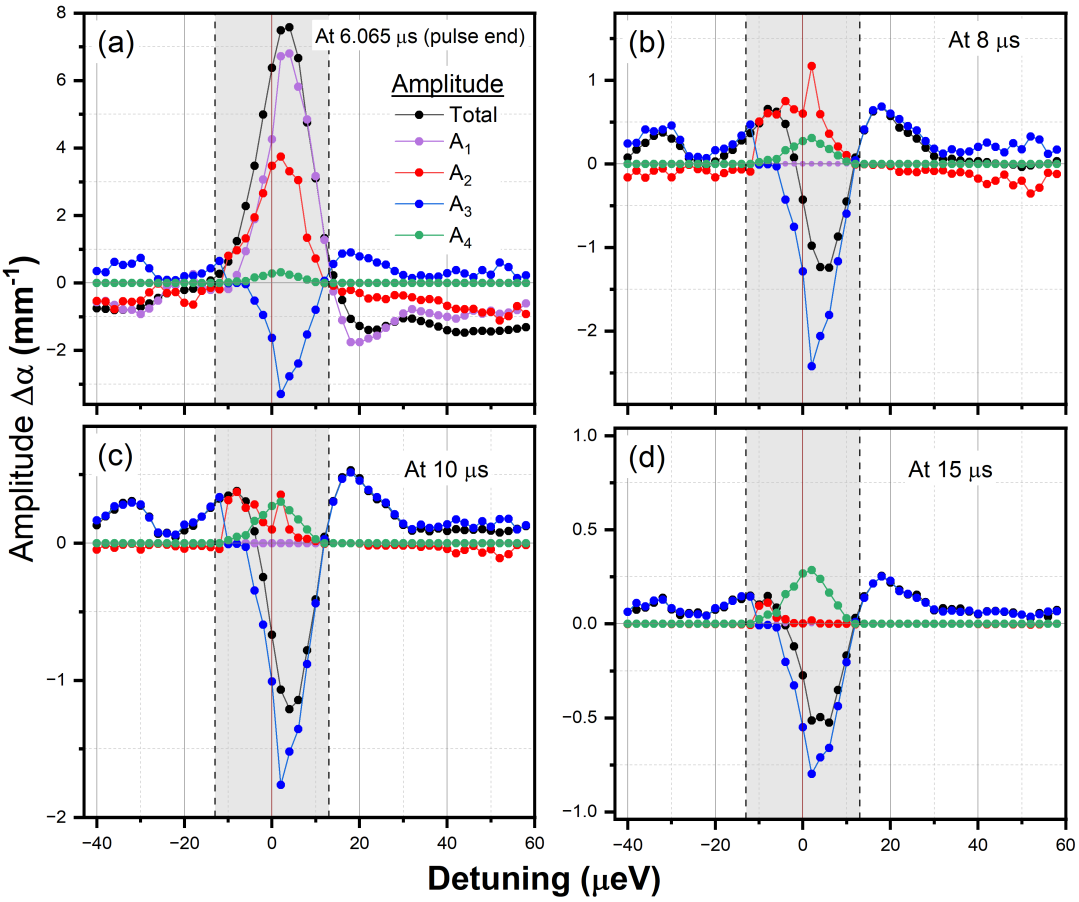

Figure 4.15: Amplitudes ($\Delta\alpha$) of individual relaxation channels present in the TR traces (as shown in Fig. 4.14) as a function of finite detunings at different time delays: (a) when the pump pulse ends at 6.065 μs, (b) at 8 μs, (c) at 10 μsand (d) at 15 μs. The ordinates scaling differs across the panels. The amplitudes are evaluated by the fitting routine discussed along Eq. 4.2. Black dots represent the overall amplitudes calculated from bare TR traces. Purple, red, blue and green dots represent amplitudes A_1 to A_4, respectively. In the detuning range -13 to 13 μeV (shaded grey areas), the amplitudes A_1, A_2 and A_4 have positive sign, while A_3 has a negative sign. The strongest change $|\Delta\alpha|$ occurs at $\sim$ 5 μeV away from the absorption peak due to the short-lived A_1, while the weakest change originates from of the long-lived A_4. Outside the shaded detuning range, all amplitudes show the opposite sign of $\Delta\alpha$, except for A_4, which becomes zero. At detunings -34 and 21 μeV, $\Delta\alpha$ for all amplitudes again reaches maximal values, indicating the influence of $10S$ and $10F$ exciton resonances.

4.5.1 Comparison of amplitudes and relaxation rates

In general, we find a total of four distinct relaxation channels with different relaxation timescales. In Fig. 4.15, amplitudes of all relaxations are shown as a function of the probe detuning. The amplitudes from A_1 to A_4 are shown in purple, red, blue and green dots, respectively. Similarly, black dots represent the total $\Delta\alpha$ which is the sum of all individual amplitudes. Different panels represent the amplitudes at different time: 6.065 μs (end of pump pulse) (a), 8 μs (b), 10 μs (c) and 15 μs (d). Beyond 15 μs, only the long-lived mechanism with the amplitude A_4 remains relevant. Thus, we choose not to compare the amplitudes at a later time. We observe completely different dynamics for different detuning ranges. The two vertical grey dashed lines split the detuning ranges into three parts: -40 to -13 μeV, -13 to 13 μeV (shaded grey areas in Fig. 4.15) and 13 to 58 μeV. In the following, we discuss and compare all amplitudes in the three different detuning ranges for all panels.

At first, we discuss the amplitudes in the small detuning range -13 to 13 μeV, as indicated by shaded grey areas in the different panels of Fig. 4.15. At the end of the pump pulse (6.065 μs), the total $\Delta\alpha$ is positive, as shown by black dots in Fig. 4.15(a). The maximal value of $\Delta\alpha$ is +7.6 mm^{-1}, found at a blue detuning of $\sim$ 5 μeV. However, with the evolution of time, the total $\Delta\alpha$ becomes negative as represented by black dots in panels (b), (c) and (d). The maximum negative values of $\Delta\alpha$ at 8, 10 and 15 μs are -1.24, -1.21 and -0.5 mm^{-1}, respectively. Surprisingly, akin to the observation at 6.065 μs, the maximal negative value is still blue detuned by $\sim$ 2 μeV at these times, albeit the magnitude of change in absorption dropped. We would expect a redshift of $\Delta\alpha$ if negative $\Delta\alpha$ was caused by an increasing amount of charged impurities which should give rise to an enhanced Stark shift. A_1, A_2 and A_4 are always positive, and hence corresponding processes contribute to the increase in probe absorption. On the contrary, A_3 is negative. $|\Delta\alpha|$ for all the amplitudes drop over time. For details about the potential origin of the physical processes corresponding to these amplitudes, a detailed discussion is given in subsection 4.3.1.

In the detuning ranges, -40 to -13 μeV and 13 to 58 μeV, the magnitude $|\Delta\alpha|$ of all individual relaxations are comparatively smaller. The maximal changes in the absorptions are seen near the detunings -34 and 21 μeV, which are close to the energies of the10S and 10F exciton resonances, respectively. At time 6.065 μs, we observe that the magnitude of maximal change ($|\Delta\alpha|$) for both overall and A_1 amplitude is a factor of $\sim$ 7 smaller as compared to the amplitudes observed for detuning between -13 to 13 μeV. At the same time, a drop of factor 4 is seen in the case of amplitude A_2 and A_3. $|\Delta\alpha|$ for A_4 is zero. Furthermore, with the evolution over time, outside detuning range -13 to 13 μeV, all amplitudes except A_3 approach zero as depicted in panels for the individual delays of (b) 8 μs,

(c) 10 μs and (d) 15 μs. The only remaining relevant amplitude after 15 μs is A_3.

To comprehend the shift of the amplitude maxima over time, we normalize (between 0 to 1) the amplitudes with respect to their maximal value. Each panel in Fig. 4.16 plots the normalised amplitude of different relaxation channels as a function of the probe laser detuning. We found that only amplitude A_2 shifts towards negative detuning with time, whereas the maxima of A_3 and A_4 do not shift. For A_1, it is difficult to interpret the shift considering the almost instantaneous nature of the decay time scale.

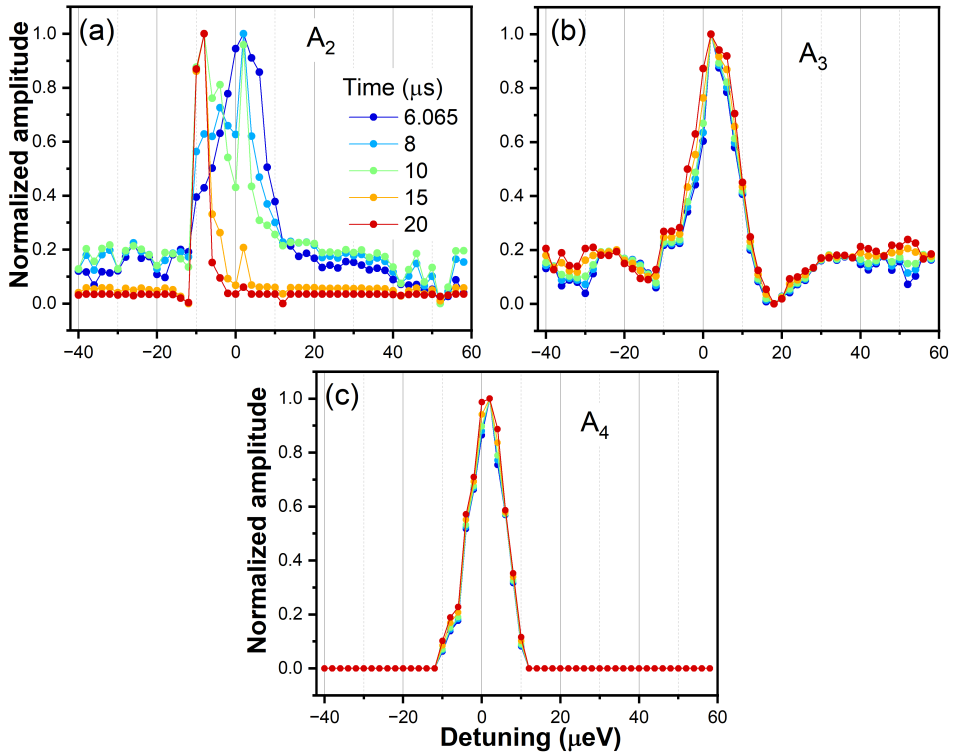

Figure 4.16: Normalized amplitudes A_2 (a), A_3 (b) and A_4 (c) as a function of the probe laser detuning from the peak of $10P$ resonance. The sign of A_3 is inverted for better visualization.

4.6 Summary

In this chapter, we studied the dynamics of purification using time-resolved two-colour pump-probe measurements. A pulsed pump laser was used for the excitation, and the corresponding changes in the optical properties of the material Cu_2O were recorded through changes in the absorption of a CW probe laser. We analysed the relaxation of the signal $\Delta\alpha$ after the pump pulse ends. A total of five relaxation channels were identified, indicating the involvement of five different physical processes.

First, the pump laser was spectrally positioned near the shifted bandgap $\tilde{E}_g = 2.17208$ eV and the probe laser was set to different exciton resonances. Among the four relaxation channels observed, A_1, A_2 and A_4 exhibit positive amplitudes ($\Delta\alpha > 0$), indicating their role in the increase of absorption, while A_3 has a negative amplitude. The relaxation rate R_1 is resolution-limited, while the other three relaxation rates R_2, R_3 and R_4 vary between 2 - 20 μs^{-1}, 0.2 - 0.8 μs^{-1} and 0.02 - 0.06 μs^{-1}, respectively. To understand the origin of these four relaxation processes contributing to the overall purification, we performed the following two sets of experiments and compared them.

In the first scenario, the effects of exciton density on the purification process were investigated by changing the intensity of the probe laser. The pump laser excited a low density of high-n RE at $n = 16$ to purify the material, while the probe laser was fixed at $n = 10$ with its intensity varied. The TR traces were recorded. The total amplitude, as well as all the individual amplitudes, decreased exponentially with increase in the probe intensity. The relaxation rates R_2 and R_3 increased linearly, while R_4 and R_5 exhibited a quadratic and square root dependence on the probe intensity, respectively.

The amplitude A_1, which showed resolution-limited dynamics, may be related to the lifetime of the excitons. The excitation of Rydberg excitons adjacent to a charged impurity might screen the impurity, thereby reducing the net stray electric field in the material, which in turn enhances the excitonic absorption. This process vanishes as soon as the pump pulse is switched off. From the scaling laws, it was speculated that the amplitudes A_2 might be related to the physical process of exciton capture at a charged impurity site and simultaneous photo-induced ionization of a neutral impurity, as discussed in Bergen et al. [8]. Although $R_3 \propto I_{pr}$, the negative sign of A_3 makes its origin unclear. Because of its longest relaxation time, the physical process related to A_4 may stem from a long-living bound exciton-impurity complex. Finally, since A_5 was observed only at high probe intensity. The corresponding physical process might be related to the screening of impurities by an e-h plasma.

In the second scenario, the influence of e-h plasma on the purification was studied. We fixed the pump and probe lasers to the resonances $n = 16$ and $n = 10$, respectively, and set their intensities to achieve maximal purification. On top of these two lasers, an additional CW laser excited the e-h plasma at varying intensities. The total amplitude dropped and revealed a square root dependence on the intensity of the green laser, while its component amplitudes did not show any specific dependence. Similarly, no particular scaling laws were observed for the relaxation rates.

Finally, we investigated the purification mechanism with non-resonant excitation. Essentially, we detuned the probe laser from the peak of the $n = 10$ resonance while keeping the pump laser fixed at $n = 16$. The intensities of both lasers were set to achieve the maxi-

mal purification. The purification process was most efficient at a detuning of ~ 5 μeV. The absorption decreased outside the detuning range of -13 to 13 μeV.

Chapter 5

Interaction dynamics of Rydberg excitons

In the previous chapter, we discussed the dynamics of purification. Essentially, we studied the non-equilibrium dynamics of exciton-impurity interaction using a pulsed pump laser for excitation and a CW probe laser for detection. The intensities of the pump and probe lasers were deliberately kept low to ensure that only impurities interact with RE, and exciton-exciton interaction or exciton-plasma interaction is minimal. Moreover, the energy of the pump laser was always set to values larger than that of the probe laser, i.e. $E_{pump} > E_{probe}$, so that purification reaches its maximal value. Thereafter, we distinguished different underlying physical processes with different timescales, which constitute the overall change in absorption.

In other excitation scenarios, with optical excitation of the sample, a complex mixture of specimens is created, such as excitons, plasma and charged impurities. The resulting absorption change may stem from exciton-exciton, exciton-plasma, or exciton-impurity interaction. The dominant type of interaction should explicitly depend upon the excitation energy and intensity of both lasers. Therefore, in the current chapter, we focus on studying the dynamical response of RE by changing the pump and the probe laser parameters, such as energy and intensity. The same TR pump-probe set-up we already applied in section 4.1 is employed here, and the decay of the signal after the end of the pulse is analysed to distinguish the involvement of different underlying physical mechanisms.

The outline of the whole chapter is as follows. In section 5.1, we discuss the methods and introduce the two settings used during data acquisition. In section 5.2, we fix the probe laser to a particular resonance and set the pump laser to different energies. In section 5.3, we fix the pump laser to a particular exciton resonance and vary the probe laser energy across several exciton resonances. In both sections, we collect TR traces of the change in

probe absorption at a series of pump laser intensities and analyse the amplitudes and times of different component relaxation channels involved. Section 5.4 summarises the chapter.

5.1 Methods

In the experiment, we employ the same time-resolved pump-probe setup that is used in the previous chapter 4. For details of the experimental setup and methods of the data acquisition, look at section 4.1. The only difference is that the measurements are performed by varying the pump laser intensity while the intensity of the probe laser is fixed. Essentially, we perform TR pump-probe measurements in the following two different settings. Firstly, the probe laser is fixed at $n_{probe} = 10P$ resonance, and the pump laser is varied to four different energies: resonant with $n_{probe} = 14P$ and $9P$, to 2.117957 eV (in the phonon background between $1S$ and $2P$ resonance) and to 2.0135 eV (lower than the energy of the $1S$ exciton resonance). Secondly, the pump laser is set to the $n_{pump} = 9P$ resonance, whereas the probe laser is set to different Rydberg exciton resonances, starting from $11P$ up to $18P$. In the following sections, both measurements and corresponding observations are qualitatively discussed.

5.2 Variation of pumping laser energy

The weak probe laser with intensity I_{pr}= 1.39 mW /cm^2 is fixed at the peak of the resonance $10P$, i.e. $n_{probe} = 10P$, and a comparatively stronger pump laser is set to four different energies (E_{pump}). The exact energies of the pump laser (E_{pump}) and the probe laser (E_{probe}) are indicated in Fig. 5.1(a) using different colours. Firstly, we fix E_{pump} to the resonance $n_{pump} = 14P$, which is indicated by a red. In this case, $n_{pump} > n_{probe}$. Secondly, the pump laser resonantly excites $9P$ excitons, i.e. $n_{pump} < n_{probe}$ (green arrow). In the third case, we excite $1S$ excitons by indirect absorption via the phonon continuum, where $E_{pump} =$ 2.117957 eV (violet arrow). Consequently, the $1S$ excitons create an electron-hole plasma through the two-body Auger process. The e-h plasma, in turn, may then influence the absorption of the probe laser (see chapter2.5). Besides these three spectral positions of the pump laser, we also set the pump laser energy below the $1S$ resonance, i.e. $E_{pump} =$ 2.01357 eV (brown arrow), where a priori no absorption is expected. The corresponding TR traces for each combination of E_{pump} and E_{probe}, are shown in Fig. 5.1(b), (c), (d) and (e) at three different pump laser intensities (I_{pu}). Here, a positive value of $\Delta\alpha$ indicates an increase in the probe laser absorption, while a negative $\Delta\alpha$ represents a reduction of the probe absorption. In the following, we qualitatively discuss each panel.

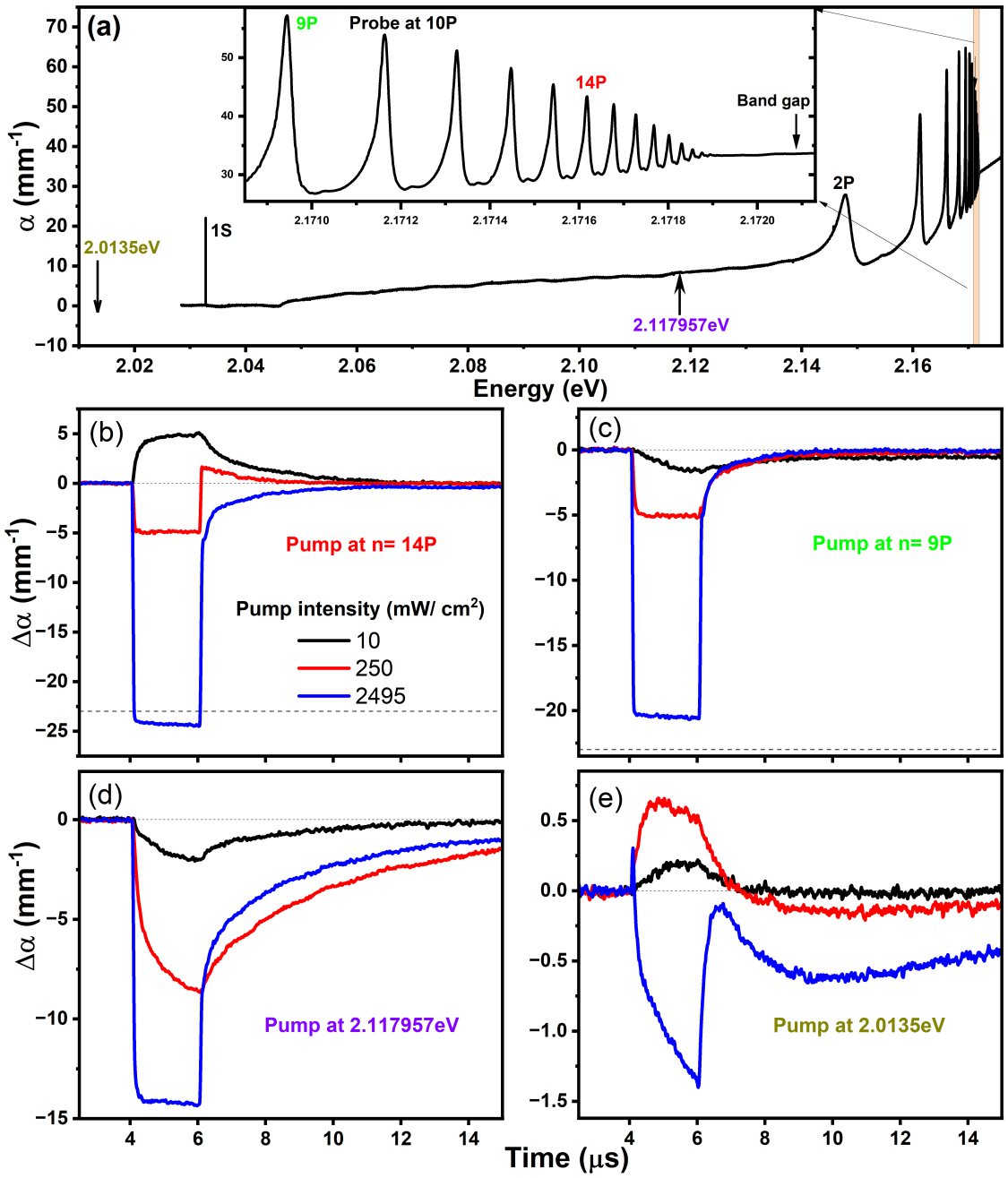

Figure 5.1: (a) Linear absorption spectrum of the yellow exciton series, starting from 2.0284 eV to 2.176 eV (above band gap). Distinct exciton resonances are visible as asymmetric Lorentzian peaks on top of the continuum phonon background, which starts at an energy of 13.6 meV above the 1*S* exciton energy. The pump laser is fixed at the following spectral positions: $n_{pump} = 14P$ (red), $9P$ (green), 2.117957 eV (purple) and 2.0135 eV (brown). The probe laser is set to the resonance $n_{probe} = 10P$ (black). (b), (c), (d) and (e) Change in absorption coefficient ($\Delta\alpha$) with time at the four mentioned pump energies. At each pump energy, TR traces are demonstrated for three different pump intensities: 10 (black), 250 (red) and 2495 mW /cm^2(blue).

In Fig. 5.1(b), TR traces are shown for E_{pump} resonant with $n = 14P$. At low I_{pu} = 10 mW /cm^2, the presence of the pump laser directly results in an increase in absorption ($\Delta\alpha > 0$) of the probe laser, as shown by the black curve. The origin of such an enhancement of absorption can be attributed to the neutralization of charged impurities by RE. After the pump pulse is over, $\Delta\alpha$ decays back to zero on a timescale of a few microseconds. Such a long relaxation time larger than the lifetime of RE indicates the involvement of impurities in the respective process. At an intermediate I_{pu} = 250 mW /cm^2, $\Delta\alpha$ becomes negative during the presence of the pump pulse, as depicted by the red curve. At the end of the pulse, $\Delta\alpha$ instantly changes sign from negative to positive on a nanosecond time scale, which is much faster compared to low pump intensities. This indicates some short-living species interacting with the probe created excitons while the pump pulse is present. From the positive value, $\Delta\alpha$ reverts back to the initial value $\Delta\alpha = 0$ on a microsecond timescale. Furthermore, $\Delta\alpha$ attains a minimum value of -25 mm^{-1} at the highest I_{pu} = 2495 mW /cm^2, as shown by the blue curve. At this intensity, the $10P$ resonance, where the probe laser is fixed, is completely bleached. When the pump pulse is over, $\Delta\alpha$ decays initially on a nanosecond timescale to a smaller amplitude, followed by a microsecond-long decay to zero. $\Delta\alpha$ does not become positive.

Figure 5.1(c) shows the TR traces when E_{pump} is set to the $9P$ resonance. The absorption of the probe laser is reduced for all I_{pu}, i.e. $\Delta\alpha < 0$. At low I_{pu}, the decay process takes a few microseconds. However, at intermediate and high I_{pu}, at the end of the pump pulse, $\Delta\alpha$ decays almost instantaneously within a few tens of nanoseconds to a smaller amplitude, followed by a long decay on a microsecond timescale. The presence of a long decay at all I_{pu} indicates the corresponding process to be related to impurities. In contrast to purification, this long decay process drives the impurity system towards an equilibrium state containing more charged impurities than the equilibrium state created by only the probe laser, see Ref. [8]. On the other hand, the instantaneous decay might stem from Rydberg blockade considering the humongous density of $9P$ RE that are excited by the pump laser. Additionally, the indirect creation of $1S$ exciton by absorption via the phonon background and subsequent creation of electron-hole plasma via the Auger effect may play an important role in reducing absorption.

When E_{pump} is set to enable the excitation of the $1S$ exciton via absorption at the phonon background, the probe absorption is always reduced irrespective of I_{pu}, i.e. $\Delta\alpha < 0$. This is shown in Fig. 5.1(d). The TR traces at low I_{pu} (black) are comparable in both panels (c) and (d). However, at the intermediate I_{pu} (red), the indirect excitation of the $1S$ exciton results in $\Delta\alpha$= -8 mm^{-1}, which is larger by 3 mm^{-1} compared to the case when the pump is set to $9P$ (panel (c)). This result is a contradictory, given that the absorption for $n_{pump} = 9P$ is nearly twice as high. At high I_{pu} (blue), an instantaneous decay with lower amplitude

is observed, which is less compared to the one in panel (c). A detailed comparison of the amplitudes is provided in the next section.

Lastly, we set E_{pump} to an energy below the resonance of $1S$ exciton. The corresponding TR traces are shown in Fig. 5.1(e). At this energy, no significant amount of absorption is expected because there are neither exciton resonances nor any phonon-related absorption [88]. However, the photoionization of impurities may result in a small change in absorption. Notably, we observe a well-defined response of $10P$ excitons to the pump pulse, albeit $\Delta\alpha$ is ten times weaker than the other three scenarios. The different scales of the ordinate should be kept in mind. Up to I_{pu}= 250 mW /cm^2(red line), we observe an increase in absorption ($\Delta\alpha > 0$) of about 0.65 mm^{-1} due to purification. While the origin of purification is attributed to the capture of RE at a charged impurity site, purification is not expected at this pump energy since no excitons are directly excited. Another possibility is the excitation of an electron-hole plasma by a two-photon process, which may cause purification after relaxation to the high-lying RE states. After the pump pulse is over, $\Delta\alpha$ does not directly revert to zero but becomes negative and finally decays slowly over a few μs. At high pump intensity of I_{pu}= 2495 mW /cm^2 (blue line), $\Delta\alpha$ is reduced to a minimum value of -1.2 mm^{-1}during the presence of pump pulse. This could be due to photoionization of neutral impurities. However, the $10P$ resonance is still far away from complete bleaching. After the end of the pump pulse, the decay of $\Delta\alpha$ to zero is complex and consists of a fast decay, a slow growth and another slower decay.

5.2.1 Separation of constituent relaxation processes

To quantitatively compare the four different excitation scenarios as shown in Fig. 5.1, the decay of $\Delta\alpha$ after the end of the pump pulse is analysed. Constituent relaxation channels are segregated using the fitting routine mentioned in Chapter 4 and subsection 4.1.2. The fitting function is again mentioned in Eq. 5.1. In all excitation scenarios, we find that there are primarily four relaxation channels involved, which can be better noticed in a semilogarithmic representation (see Fig. 5.2(c)). The four relaxation channels associated, are shown by green, cyan, red and blue lines.

$$\begin{aligned}\Delta\alpha = \Delta\alpha_0 + A_1 e^{-\left(\frac{t-t_0}{t_1}\right)} + A_2 e^{-\left(\frac{t-t_0}{t_2}\right)} \\ + A_3 e^{-\left(\frac{t-t_0}{t_3}\right)} + A_4 e^{-\left(\frac{t-t_0}{t_4}\right)}.\end{aligned} \tag{5.1}$$

Here, A_1 to A_4 are the amplitudes of the four constituent relaxation channels, which sum up to give the total change in probe absorption ($\Delta\alpha = \alpha_{pump} - \alpha_0$). The related relaxation

times are t_1 to t_4. Notably, the amplitudes are always evaluated near the end of the pump pulse at time t_0= 6.065 μs.

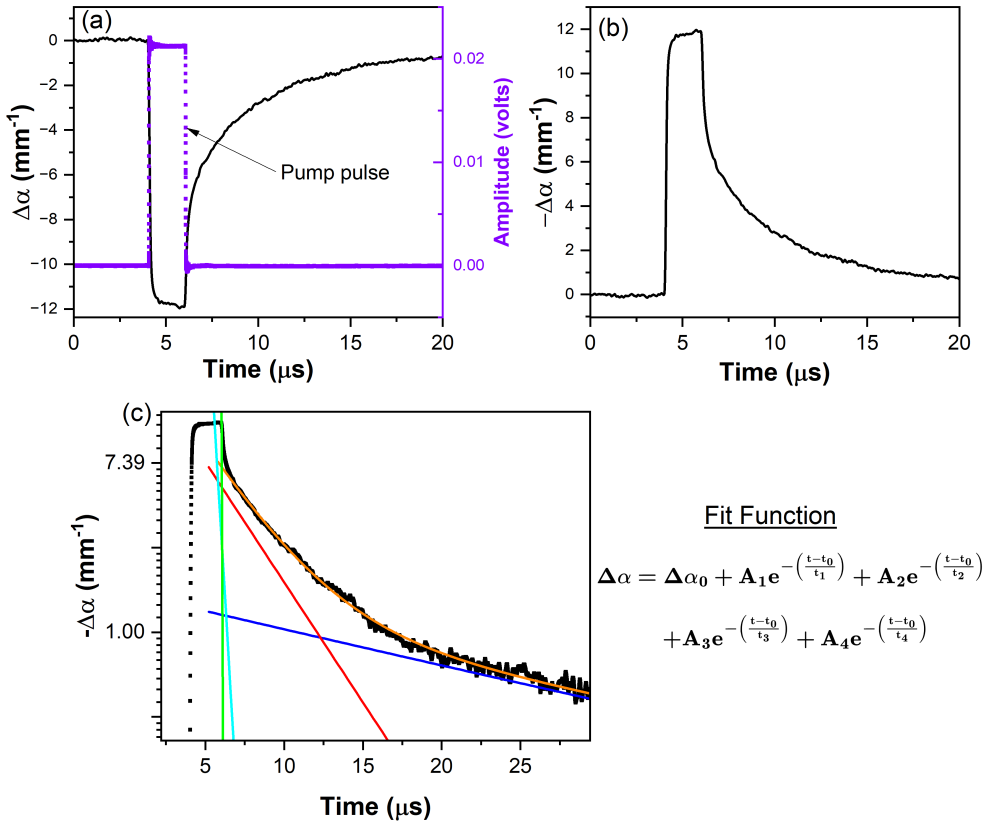

Figure 5.2: (a) Black curve: TR trace of change in absorption coefficient ($\Delta\alpha = \alpha_{pump} - \alpha_0$). The pump ($I_{pu}$) and the probe ($I_{pr}$) intensities are 1577 and 1.39 mW /cm^2, respectively. The probe laser is fixed on resonance $n_{probe} = 10P$, while the pulsed pump laser is set to an energy of 2.117957 eV. The purple dots represent the pump pulse in the time domain. $\Delta\alpha < 0$ means a drop in probe absorption, while $\Delta\alpha > 0$ indicates an increase in absorption. (b) TR trace with y-axis changed to $-\Delta\alpha$ for better demonstration. (c) Fitting of the decay of the TR trace using the procedure mentioned in Eq. 5.1. A total of four relaxation channels are found as shown by green, cyan, red and blue lines.

5.2.2 Relaxation times and amplitudes

Figure 5.3 shows the parameters, such as amplitudes and relaxation times obtained from the fitting procedure, as a function of I_{pu} at four different values of E_{pump}. The amplitudes and relaxation times are shown in the upper and lower panels, respectively. The amplitudes from A_1 to A_4 are represented by green, cyan, red and blue dots, as well as the corresponding relaxation times. The hollow and solid dots represent the sign of the amplitude. For positive amplitudes, open dots are used, while solid dots are used for negative amplitudes.

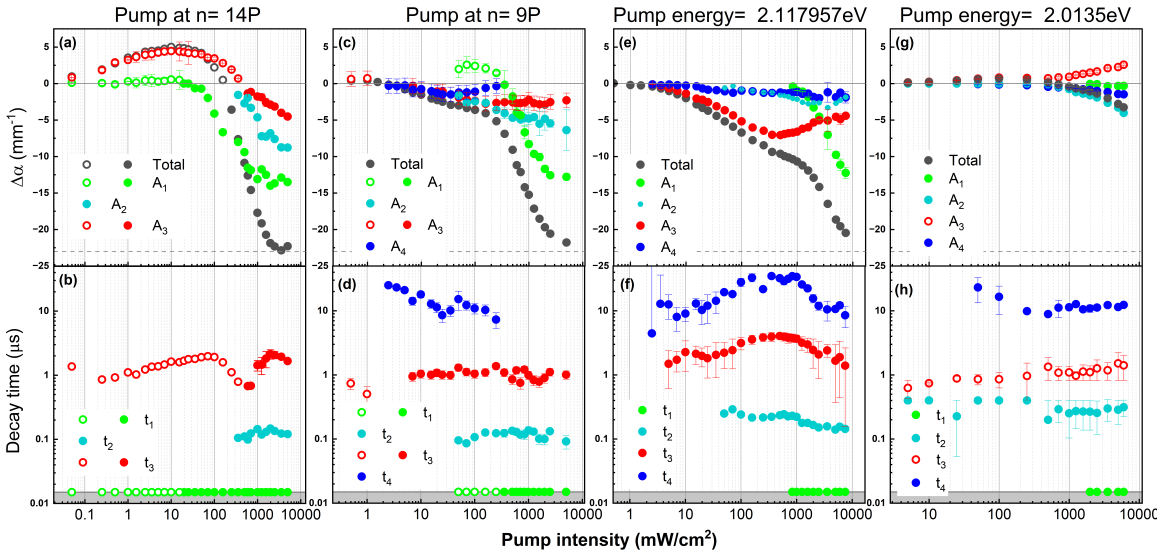

Figure 5.3: Upper panels: change in absorption coefficient ($\Delta\alpha$) as a function of pump laser intensity, at four different pump energies: 14P (a), 9P (c), 2.117957 eV (e) and 2.0135 eV (g). The probe is set to the intensity of 2.35 mW /cm^2(except in (g), which is measured with 500 nW) and fixed on the resonance $n_{probe} = 10P$. The grey dashed lines indicate the maximum possible $\Delta\alpha$ ($\Delta\alpha_{min}$= -23 mm^{-1}) for 10P resonance. The $\Delta\alpha_{min}$ is defined as the point at which complete ionization of resonance occurs. Black dots are for overall absorption changes which are dissected into constituent relaxation channels using fitting routine 4.1.2. There are a total of four relaxations with amplitudes A_1 to A_4, which are shown in green, cyan, red and blue dots. Open and solid dots are used for the positive and negative signs of the amplitude, respectively. Lower panel: corresponding timescales t_1 to t_4 are plotted as a function of pump intensity in (b), (d), (f) and (h), respectively. t_1 falls under the resolution limit (15 ns), while t_2, t_3 and t_4 have relaxation timescales in the range 0.1-0.3, 0.9-3 and 10-30 μs, respectively.

Black dots in each panel of the upper row represent the total change in probe absorption in terms of $\Delta\alpha$. The largest possible magnitude of change in absorption coefficient ($\Delta\alpha_{min}$) per exciton resonance is given by the difference between the absorption in the absence of a pump laser, i.e. α_0, and the absorption when the resonance is completely bleached, i.e. $\alpha_{pump,min}$. For $n_{probe} = 10P$, we know from corresponding CW measurements that $\Delta\alpha_{min}$ is -23 ± 1 mm^{-1}. $\Delta\alpha_{min}$ is depicted by the horizontal grey dashed lines in the upper panels. The minimum I_{pu} required to achieve $\Delta\alpha_{min}$ relies entirely on E_{pump}. In the following, we quantitatively describe the constituent amplitudes and decay times in detail.

We begin with discussing the scenario of pumping 14P excitons (leftmost column). We observe an enhancement of the total amplitude (black dots) at low I_{pu} (hollow dots). The maximum amplitude is found to be $\sim$5 mm^{-1} at I_{pu}= 20 mW /cm^2. The enhancement of the probe absorption is due to purification. With the further increase in I_{pu}, the total amplitude drops steeply and changes from a positive to a negative value. Finally, saturation

($\Delta\alpha_{min}$= -21 $\pm$1 mm^{-1}) occurs at I_{pu} $\sim$ 3000 mW /cm^2. The amplitude A_1 (green dots) remains close to zero at low I_{pu} and starts to decrease strongly after 100 mW /cm^2 until it reaches a minimum value of -12 mm^{-1}. The related decay time t_1 is less than 15 ns, which is given by the resolution limit of our experimental setup. The fast decay time indicates that the process might be related to a short-living species. In this case, RE are most likely involved. A_2 shows similar trend to A_1, albeit reaching a minimum value of -8.5 mm^{-1}. t_2 is in the range of 100 ns. Such timescales on the order of hundred nanoseconds suggest that this effect is related to free charge carriers such as electrons and holes. These carriers can be formed by the Auger decay of 1S-excitons created through absorption via the phonon background. In contrast to A_1 and A_2, amplitude A_3 increases to a positive maximum value of $\sim$ 5 mm^{-1} at low I_{pu} of 20 mW /cm^2, and then begins to drop. Considering the positive amplitude at low I_{pu}, this process might be related to purification as well. At $I_{pu} \sim$ 800 mW /cm^2, A_3 becomes negative, and reduces to a minimum value of -5 mm^{-1} at the highest I_{pu} of 7500 mW /cm^2. This may be linked to the net enhancement of the density of charged impurities, which may take place through photo-ionization. The timescale t_3 is in the range of 0.8-2 μs. A_4 is negligible and impossible to calculate at this pump and probe laser energy combination.

When $E_{pump} < E_{probe}$ (middle left and right columns of Fig. 5.3), the total amplitude (black dots) is always negative and drops in a step-like manner with I_{pu}, albeit differently based on E_{pump}. Such a step-like feature indicates the dominance of different entities at different regimes of I_{pu}. Both middle columns are discussed in the following.

When the pump laser is set to 9P (middle left column), a step-like drop in the total amplitude is observed. The drop is only -5 mm^{-1} at I_{pu}= 100 mW /cm^2. Beyond I_{pu}= 100 mW /cm^2, the drop is steep, and the total amplitude becomes significantly larger by a factor of 4 until it achieves saturation. The fastest process with amplitude A_1 has a positive value of 2.5 mm^{-1} at low I_{pu}. Such a fast process with a positive amplitude may be related to the screening of charged impurities by the RE as it vanishes at the end of the pump pulse. A_1 drops with I_{pu} and takes to negative values at higher $I_{pu} \geq$400 mW /cm^2. Akin to pumping at 14P states, the drop of A_1 may be linked to the Rydberg blockade of 9P excitons or Auger-created e-h plasma. A_2 is always negative, reduces with increasing I_{pu}, and reaches a largest value of -6 mm^{-1}. Its timescale t_2 is around 100 ns. This process may stem from an e-h plasma created by long-living 1S-para excitons via the Auger process. The other amplitudes A_3 and A_4 have comparatively smaller negative values. In fact, A_4 is absent beyond I_{pu} of 20 mW /cm^2. The corresponding timescales t_3 and t_4 are in the range of 1 μs and 10 μs, respectively. The presence of these two different decays with long decay dynamics hints at their potential origin from two different types of impurity-related processes.

In the third scenario (middle right column), the pump laser energy is away from resonance at E_{pump}= 2.117957 eV. The total amplitude ($\Delta\alpha$, black dots) still drops in a step-like manner. Below I_{pu}= 1000 mW /cm^2, we observe a reduction of the total amplitude by -10 mm^{-1}. In this case, we have not reached the saturation value $\Delta\alpha_{min}$ even at the highest I_{pu} of 7500 mW /cm^2. A_1 is almost zero until I_{pu}= 1000 mW /cm^2, and abruptly rises beyond. Considering its fast timescale and dominance at high I_{pu}, one can speculate that this process originates from species with a lifetime in order of a few nanoseconds. In this case, the species could be 1S-ortho excitons, which can reduce the probe absorption by creating e-h plasma via the Auger process. Also, 2-photon absorption that directly creates plasma cannot be ruled out. On the other hand, similar to pumping at 14P and 9P, the process related to amplitude A_2 and timescale t_2 may stem from comparatively long-living 1S-para excitons. A_2 and A_4 are small, and they have a minimum negative amplitude of -1.5 mm^{-1} at the highest I_{pu}. These two processes can only be differentiated based on their decay timescales which are 100 ns and 10 - 30 μs. A_3 which is related to impurities, decreases to -7.5 mm^{-1} up to I_{pu}= 300 mW /cm^2, and starts to increase afterwards. The onset of the increase coincides with the sharp decrease of A_1. This suggests the dominance of free carriers over impurity effects at high I_{pu}.

The rightmost column is a special case. Here, the pump energy is fixed at E_{pump}= 2.0135 eV (below 1S-ortho exciton). Ideally, no absorption is expected. However, we see a small change in the absorption of the probe laser. The total amplitude increases to a maximum of 0.7 mm^{-1} at I_{pu}= 100 mW /cm^2, and starts to drop at higher intensities. It finally changes sign to negative and achieves a mere -3.3 mm^{-1} even at the highest I_{pu} of 7500 mW /cm^2. The amplitudes A_1, A_2 and A_4 are always negative and reduce with I_{pu}. Their timescales t_1, t_2 and t_4 are $\leq$15 ns, 300 ns, 10 - 20 μs. On the contrary, A_3 is positive and increases up to 3 mm^{-1} at the highest I_{pu}. The purification at this pump energy is surprising as the pump laser does not directly excite any excitons. However, the pump laser may be absorbed by 2-photon absorption to create a plasma, which in turn can relax to create Rydberg excitons.

5.2.3 Comparison of A_1 with the prediction of plasma model

From the discussion in the previous section, we found that for all E_{pump}, A_1 is more prominent at high I_{pu}, and its timescale t_1 is limited by the resolution (15 ns) of the experimental setup. Such characteristics indicate a potential connections to an e-h plasma or Rydberg blockade. However, when E_{pump} is set to the phonon background between 1S and 2P resonances, i.e. $E_{pump} = 2.117957$ eV, Rydberg blockade can be ruled out completely or is at least minimal. Here, we focus on comparing the amplitude A_1 for $E_{pump} = 2.117957$ eV,

and the plasma-induced change in absorption coefficient ($\Delta\alpha$) calculated using Eq. 2.47, 2.48 and 2.58. These equations are derived from the theory developed by Stolz et al. [98]. Details of the theory are given in chapter 2 and section 2.5.

For better comparison between different pump energies, the total amplitudes (black dots), as shown in the upper row in Fig. 5.3 are merged into a single plot, which is depicted in Fig. 5.4(a). The corresponding amplitudes A_1 are presented in panel (b). In panel (c), A_1 (orange) for the pump energy at 2.117957 eV and the plasma-induced change from the theory (cyan) are plotted. The rate constants used to fit the experimental data are given in table 5.1. These are different from the rate constants reported in Ref. [98] and Fig. 2.11.

Rate constant	Meaning (at steady state)	Value from fit	Value from theory	Unit
Γ_{0P}	Ortho-para conversion rate	0.006	0.2	ns^{-1}
a_{0PP}	Para-para Auger rate	10^{-6}	4×10^{-6}	$\mu m^3 \cdot ns^{-1}$
Γ_{0augnr}	Nonradiative decay rate of Auger created electrons and hole	1/5	1/500	ns^{-1}
Γ_{0augr}	Radiative recombination of Auger created electrons and hole into excitons	30	1	$\mu m^3 \cdot ns^{-1}$

Table 5.1: Comparison of rate constants from fitting A_1 amplitude and from theory [98]

.

5.3 Probing at different Rydberg exciton resonances

In the second set of measurements, we fix the pump laser at a low principal quantum number state $n_{pump} = 9P$ and vary its intensity I_{pu}. The pump laser creates a finite density of $9P$ excitons as well as $1S$ excitons via absorption in the phonon background. The $1S$ excitons, in turn, create an e-h plasma via the Auger process, which is primarily responsible for the change in probe absorption. Here, the pump excitons are unlikely to create significant Rydberg blockade, considering the small dipole moment, and thus the low blockade efficiency of $9P$ excitons (see Ref. [39]). The probe laser intensity I_{pr} is always fixed to 2.35 mW /cm^2, while its energy is varied to different Rydberg states from $n_{probe} = 11P$ to $18P$.

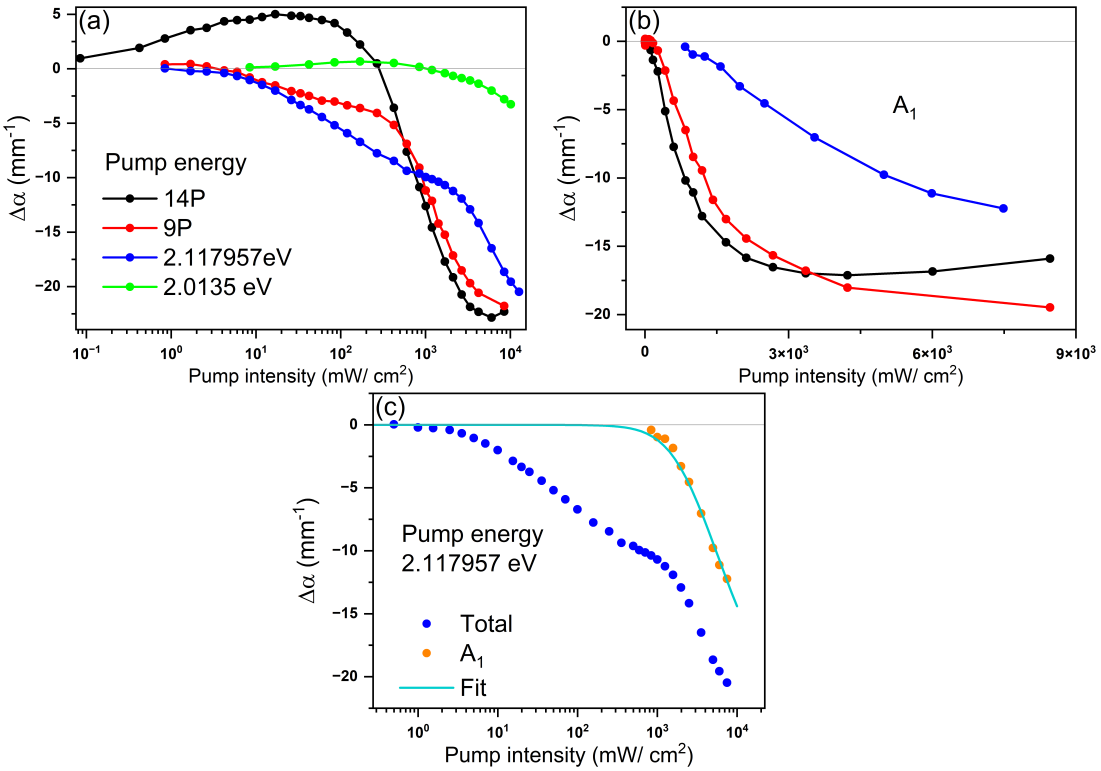

Figure 5.4: (a) Total amplitude in $\Delta\alpha$ as a function of pump laser intensity, at four different pump energies: $14P$ (black), $9P$ (red), 2.117957 eV (blue) and 2.0135 eV (green). (b) Corresponding A_1 amplitude. (c) Comparison of A_1 amplitude with plasma model [98].

5.3.1 Stretched exponential decay

The black dots in Fig. 5.5(a) show the typical TR traces of the pump-induced dynamical change in probe absorption. We investigate the relaxation of signal $\Delta\alpha$ after the end of the pump pulse. However, instead of a distinct finite number of exponential decays, as observed in the last section 5.2, we observe a more complex relaxation. This includes a series of decay channels with amplitudes and timescales that vary over time and an additional underlying long decay component. This kind of decay feature is usually seen in glass or, in general, disordered amorphous solids, where a lone atomic site interacts with inhomogeneously distributed neighbours [11, 48]. Here, we use a fit function called Stretched exponential or Kohlrausch Williams-Watts (KWW) function to accommodate a time-varying decay rate, along with a usual long decay to fit the data. The following fit function is used during analysis

$$\Delta\alpha = \Delta\alpha_0 + A_1 e^{-\left(\frac{t-t_0}{t_1}\right)^{\beta}} + A_2 e^{-\left(\frac{t-t_0}{t_2}\right)}. \tag{5.2}$$

Here, $\Delta\alpha_0$ is a small offset accounting for background noise. A_1 and A_2 are the amplitudes of the stretched exponential and the underlying long relaxation components, respectively.

The corresponding relaxation times are t_1 and t_2. β represents the statistical distribution of the time-varying relaxation rate. For $\beta = 1$, Eq. 5.2 reduces to a double exponential function. A detailed demonstration of fitting using such a function is shown in Fig. 5.5 (a). The green curve is the total fit function to the data shown by black dots. The red and blue curves represent the stretched exponential with distributed varying relaxation timescales and a long single exponential, respectively. The function used is further graphically delineated in Fig. 5.5 (b) and (c). In panel (b), the relaxation time (t_1) is fixed to 0.5 μs while three selected values for β are chosen, i.e. β= 0.2, 0.5 and 1. The order of amplitudes for different values of β flips after a particular time which is indicated by the vertical grey dashed line. Panel (c) shows a simulation of amplitude change with time at a fixed β value and three different t_1, i.e. t_1= 0.2, 0.5 and 1 μs.

5.3.2 Comparison of parameters

For each probed state n_{probe}, we measure the TR traces for a series of I_{pu}. The corresponding total change in probe absorption ($\Delta\alpha$) as a function of I_{pu}, is shown in Fig. 5.6 (a). For a better presentation, only every second n_{probe} is shown. For low n_{probe} states, i.e. $n_{probe} < 14P$, we observe a step-like feature of the change in $\Delta\alpha$ with I_{pu}, akin to the previous section, Fig. 5.3. The step-like behaviour indicates separate intensity regimes where a different types of interaction my dominate, such as exciton-impurity interactions at low intensities or exciton-plasma interactions at high intensities. Moreover, at a critical $I_{pu,cr}$ of around 250 mW /cm^2, the step of $\Delta\alpha$ occurs. On the other hand, such step-like features are absent for higher n_{probe} states, i.e. $n_{probe} \geq 14P$. This could be due to the complete bleaching of resonance before $I_{pu,cr}$.

To understand the underlying mechanisms which lead to the overall absorption change, we analyse the relaxation part of the collected TR traces. We fit the decays using the sum of a stretched exponential and regular exponential like Eq. 5.2. The parameters such as the amplitude A_1, the relaxation time t_1 and β are plotted as a function of I_{pu} in panels (b), (c) and (d) of Fig. 5.6, respectively. A_2 and t_2 are not plotted here as A_2 is less than 5% of A_1. Therefore, A_2 is manually put in most cases, which is indicated and accommodated using error bars in the plot. Moreover, A_1 decreases with increasing I_{pu} at the beginning and saturates after a certain I_{pu}. The saturation value ($A_{1,sat}$), and I_{pu} required to achieve saturation, strongly depend upon the excited probe states (n_{probe}). For Rydberg states higher than n= 14(i.e. $n_{probe} \geq 14$), $A_{1,sat}$ is reached when the resonance lines are bleached completely and the Mott transition occurs. Further, increased pump intensity (I_{pu}) only generates a

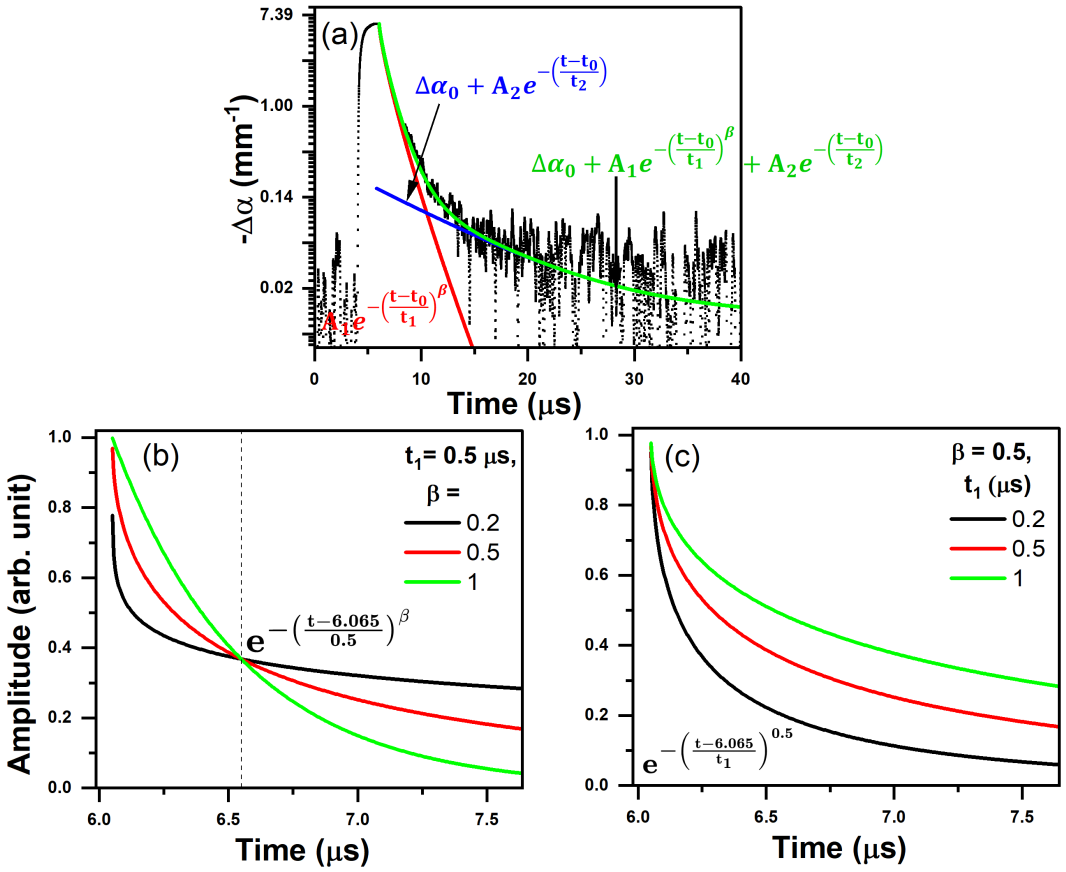

Figure 5.5: (a) Black dots: change in absorption coefficient ($\Delta\alpha$) as a function of time. Green curve: fit function (Eq. 5.2) that consists of a stretched exponential combined with an additional small slow decay. The blue and red curves individually represent regular and stretched exponentials, respectively. (b) Demonstration of a stretched exponential decay with constant decay time while varying parameters β, which determines the statistical distribution of the change in the decay rate. (c) Stretched exponential decay with varying decay times at a fixed β value of 0.5.

higher density of free charge carriers in the crystal. For Rydberg states with $n_{probe} < 14$, resonances are not bleached at saturation of A_1. Rather an additional instantaneous decay process kicks in, which is discussed in section 5.2. Similarly, with the increase in I_{pu}, t_1 increases from $\sim$0.5 μs up to $\sim$1.25 μs and remains unchanged beyond the saturation pump intensity. β smaller than 1 indicates the interaction of RE with neighbouring inhomogeneously distributed defects, such as charged impurities or vacancies. This is found at low I_{pu}These entities could be the charged impurities or vacancies. The value of β becomes close to 1 at high I_{pu}, which means less inhomogeneously distributed impurity impact.

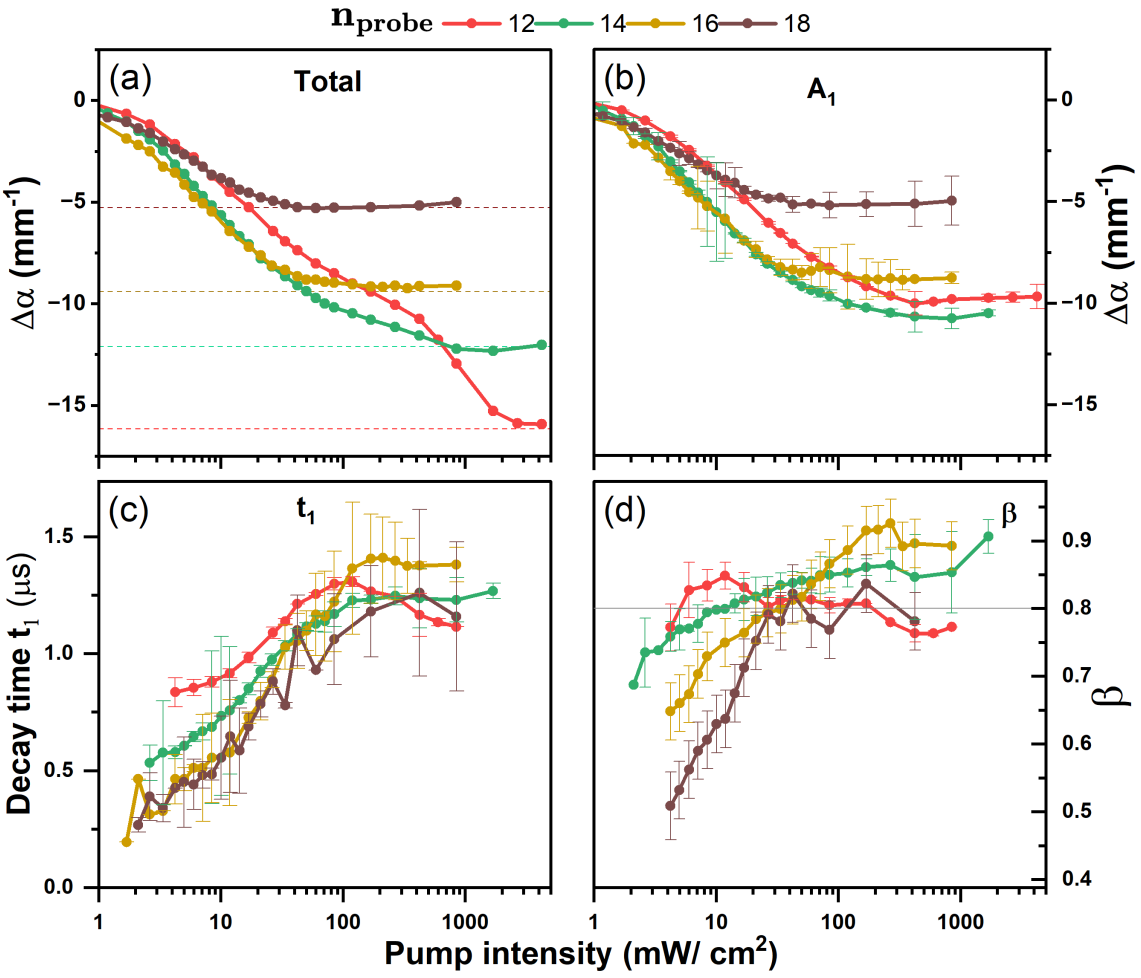

Figure 5.6: Parameters obtained from the stretched exponential fit. The pump laser is always fixed at $n_{pump} = 9P$, and the probe is set to several resonances, from $n_{probe} = 11P$ to $18P$. (a) and (b) show the total change in absorption coefficient and amplitude A_1 as a function of pump laser intensities (I_{pu}) at four alternate probe resonances. Decay time (t_1) and β change with respect to I_{pu}, are plotted in (c) and (d), respectively. t_1 increases up to $I_{pu} \sim 200$ mW /cm^2, then it has a constant value of 1.25 μs. Beyond I_{pu} = 30 mW /cm^2, β value starts to drop, which could be a sign of plasma dominance taking over from impurity dominating low powers.

5.4 Summary

In conclusion, we investigated the intricate dynamical response of Rydberg excitons under different excitation conditions, using TR pump-probe measurements. We analysed the relaxation of the signal $\Delta\alpha$ after the end of the pump pulse to understand the underlying physical interactions of RE with other entities such as other RE, impurities and an e-h plasma. Essentially, the following two sets of experiments were performed.

First, we probed at the $10P$ resonance and set the pump laser energy to four different spectral positions: $14P$, $9P$, 2.117957 eV, and 2.0135 eV. Moreover, the pump intensity was changed at each pump-probe combination. For all scenarios, we uncovered four different underlying physical processes whose relaxation timescales do not vary among the different pump laser energies.

The relaxation with amplitude A_1 was the fastest relaxation whose timescale ($\leq$ 15 ns) was limited by the temporal resolution of the experimental apparatus used. Therefore, it cannot be construed as a single decay. It might consist of several physical processes with individual relaxation timescales. A_1 can be positive at low pump intensity (see Fig.5.3 (a) and (c)), indicating it is related to RE. At high pump intensity, the amplitude was always negative which indicates its role in the decrease of absorption. The timescale of the process related to amplitude A_2 was 100 - 300 ns. It may stem from the decay of an e-h plasma formed via the Auger process of long-living para excitons. Similarly, for all of the pumping scenarios, we observed a process with timescale t_3= 1 μs. Its amplitude A_3 can be either positive or negative. The positive amplitude arises from purification, while the negative amplitude may stem from the photo-ionization of neutral impurities. Lastly, the slowest process with amplitude A_4 had a timescale in the range of 10 - 30 μs. It may originate from long-living impurities.

In the second set of measurements, we fixed the pump laser to the $9P$ resonance and varied the probe laser energy across different exciton resonances from $12P$ to $18P$. The decay of the signal $\Delta\alpha$ consisted of a series of relaxation channels with increasing timescales, which was fitted using a stretched exponential and an additional long decay. The involvement of many relaxation channels indicates the interaction of RE with surrounding inhomogeneously distributed entities, which may be impurities or plasma. The amplitude A_1 from the stretched exponential dropped with increasing pump intensity for all probing scenarios. On the contrary, the timescale t_1 increased with pump intensity. The timescale distribution parameter β varied between 0.5 to 1 with pump intensity for all scenarios. No clear scaling laws with probing n were found. The regular exponential decay underlying the stretched decay had time scale t_2 in the range of 5 - 20 μs and amplitude A_2 which was mere 5% of A_1.

Chapter 6

Conclusions and future perspectives

This thesis comprises several studies on the interactions of Rydberg excitons with various types of carriers present in a Cu_2O crystal, using both time-integrated and time-resolved optical pump-probe spectroscopy. The following sections provide a summary of the chapters in the thesis and outline potential future experiments to further explore the physics of Rydberg excitons.

In chapter 3, we demonstrated the neutralization of charged impurities using high-n Rydberg excitons, a process referred to as purification. As a result of this process, the inhomogeneous electric stray fields emanating from charged impurities are reduced, leading to an enhancement of excitonic absorption up to 100 % and a narrowing of the corresponding resonances. Surprisingly, the resonances of high-n Rydberg excitons ($n \geq 16$) which are most sensitive to charged impurities, did not show any improvement, and the exciton series was not extended. Moreover, purification was found to be maximum when the pump laser energy was set to the vicinity of the bandgap.

Our findings on purification can be utilized to enhance the quality of Cu_2O crystals, or more generally, materials hosting Rydberg excitons. This improvement could also increase the coherence of semiconductor-based quantum systems affected by charge noise. Although significant progress has been made in reducing detrimental charged impurities, achieving crystals with zero impurities will remain a challenging task for the future, which could pave the path towards further extending the Rydberg exciton series.

Besides charged impurities, unwanted exciton-phonon coupling poses another major challenge that hinders the exploitation of Rydberg excitons in Cu_2O for quantum applications. Specifically, exciton-phonon coupling weakens the strong interactions among excitonic dipoles. While Walther et al. [107] theoretically proposed using electro-magnetically induced transparency (EIT) to control such coupling, alternative approaches, such as modifying the phonon density of states using resonator or phonon engineering, could also be

effective in suppressing phonons. However, experimental demonstration of these methods remains an open challenge for future research.

The optical excitation of Cu_2O simultaneously creates a complex mixture of entities, such as Rydberg excitons, e-h plasma, and charged impurities. The interactions between different excitons, between excitons and plasma, and between excitons and impurities collectively contribute to an overall change in absorption, resulting in a complex spectral signature at the exciton resonance. Distinguishing these interactions is of fundamental interest to gain deeper insights into Rydberg exciton physics. A common strategy to isolate a specific interaction includes leveraging the scaling laws of the underlying interactions or focusing on the intensity regime where one interaction prevails over the others. Here, in chapter 4 and 5, we took advantage of the timescales of the underlying interactions to distinguish different interaction mechanisms of Rydberg excitons. These timescales were evaluated using time-resolved pump-probe measurements. The pulsed pump laser periodically changed the optical properties of the material, which were then recorded as changes in the absorption of a weak probe laser. A careful separation of the individual relaxation channels involved in the intricate relaxation after the end of the pump pulse provides insight into the underlying physical processes.

Chapter 4 was devoted to understanding the physical mechanisms behind purification, i.e. exciton-impurity interaction. A maximum of five distinct relaxation channels, each representing a unique physical process with individual amplitude and timescale, were identified which in sum describe the total change in probe absorption. The origins of these processes were estimated from the signs of their amplitudes and the power-scaling of their corresponding relaxation rates.

In chapter 5, the overall interaction mechanisms of Rydberg excitons, such as exciton-exciton, exciton-plasma and exciton-impurity interaction, were investigated. To explore these mechanisms, the properties of the pump and probe beams, such as energy and intensity, were systematically varied. The probe-pump combinations resulted in two distinct observations. In some cases, four relaxation channels were identified, pointing to the involvement of four different underlying physical processes. In other cases, the relaxation of signals consisted of multiple channels with timescales that increase over time, suggesting interactions between Rydberg excitons and inhomogeneously distributed carriers, such as impurities or plasma.

In summary, the time-resolved pump-probe spectroscopy employed in this study enables to study the interaction dynamics with timescale longer than 15 ns, such as exciton-impurity and exciton-plasma interactions. However, physical processes within timescale shorter than 15 ns, such as the Rydberg blockade, remain unexplored, emphasizing the need for ultrafast measurements.

Appendix

A.1 Calculation of exciton lineshape parameters

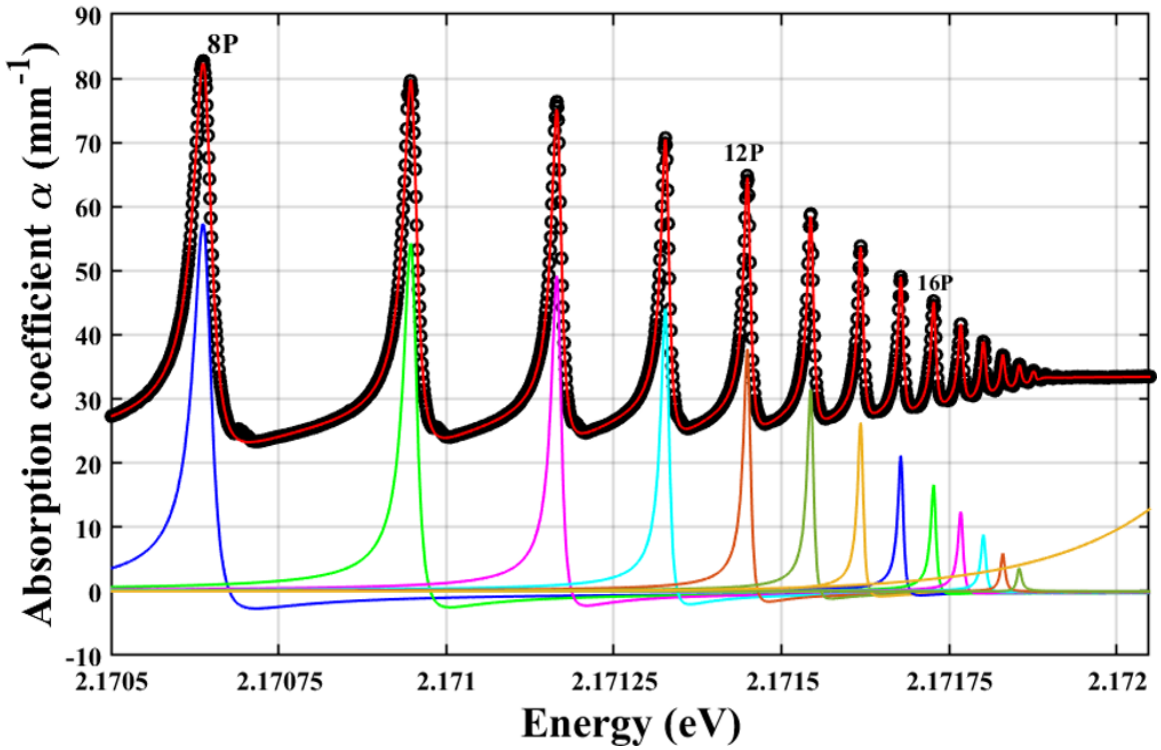

Figure 6.1: Black dots: typical absorption spectrum of RE. Red curve: fitting of entire spectrum. Individual exciton resonances are shown as asymmetric Lorentzian lines in different colours.

In order to quantify the exciton resonances, we have used the following function 6.1 to fit the entire absorption spectrum, spanning from $8P$ up to near the bandgap.

$$\alpha(E) = C_U e^{(E-\tilde{E}_g)/E_U} + \sum_{n=8}^{21} \frac{O_n}{\pi} \frac{\Gamma_n/2 + 2q_n(E-E_n)}{(\Gamma_n/2)^2 + (E-E_n)^2} \tag{6.1}$$

The first term in the above expression accounts for the Urbach-like exponential tail where

C_U and E_U are the amplitude and Urbach energy, respectively. The second term represents the sum of the absorption of all excitonic resonances from $8P$ to $21P$. These resonances are described by asymmetric Lorentzian lines with parameters E_n (resonance energy), O_n (oscillator strength), Γ_n (linewidth, full width half maximum) and q_n (asymmetry parameter).

The black dots in Fig. 6.1 show the typical absorption spectrum of excitons, while the red curve represents the overall fit. The line shapes of the individual resonances are depicted in different colours at the bottom of the absorption spectrum. Notably, during the fitting process, intermediate peaks between adjacent P-states are not taken into account, as these peaks have little oscillator strength compared to P-states. Furthermore, the fitting routine is performed using the nonlinear least squares method in the MATLAB programming software.

A.2 Calculation of laser intensity

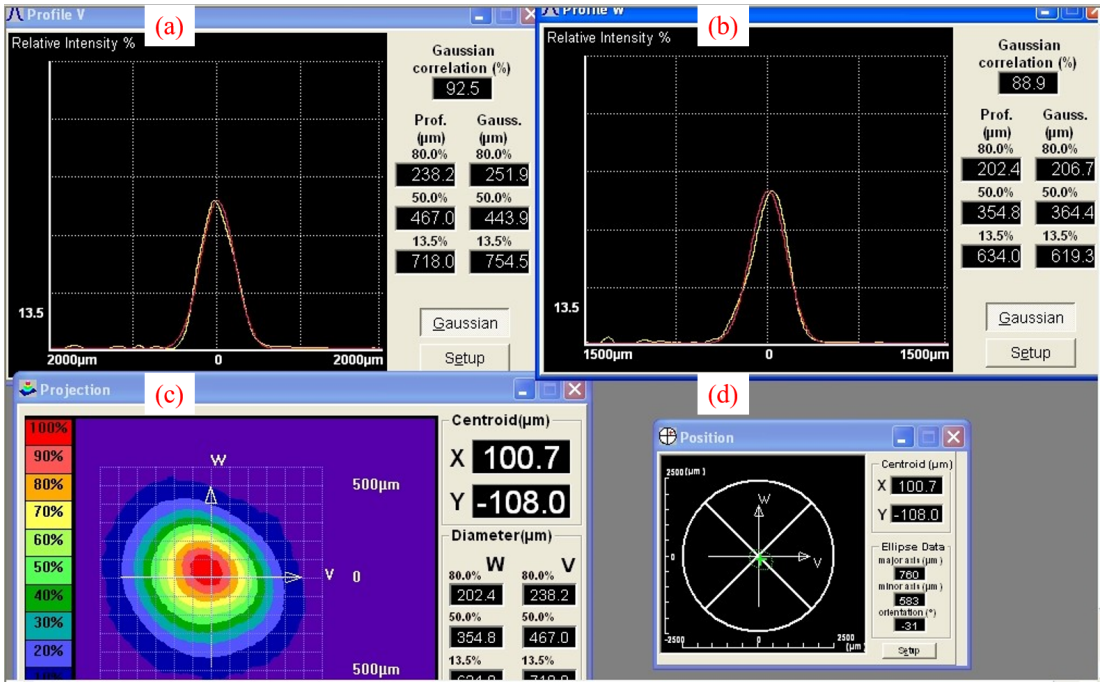

Figure 6.2: Prototype spatial beam profile of a laser along V (a) and W (b) axis. (c) Complete cross-section profile of the laser beam. Notably, the profile is measured near the sample surface. (d) Position (green dot) at which incoming laser beam hits the sensor of the beam profiler.

To calculate the intensity of the incoming laser on the sample surface, we collect the following two parameters: firstly, before each measurement, the average power (P_{avg}) of the laser beam in front of the cryostat using a power meter (Thorlabs PM100D), and secondly, only once the laser beam diameter at the sample surface using a beam profiler. The intensity is calculated using the formula given by

$$\text{Intensity} = 0.59 * \frac{4P_{avg}}{\pi v w}. \tag{6.2}$$

The factor 0.59 is included here to accommodate 59% reduction of laser powers due to reflections from several surfaces, such as 4% from 3 front windows (6 surfaces) of the cryostat and 25% from the front surface of the sample. v and w are the diameters of the laser beam along V and W direction as shown in panels (a) and (b) of Fig.6.2. We use the following three lasers: the probe, the pump, and the green laser, whose diameters v$\times$w are 140$\times$140 μm, 294$\times$256 μm and 467$\times$354 μm, respectively.

List of Symbols

Symbol	Meaning
A	vector potential of the electromagnetic wave
A_0	amplitude of the plane wave for the vector potential
A_i	amplitude of relaxation channel
a_B^{ex}	exciton Bohr radius
a_B^H	hydrogen Bohr radius
$\hat{a}/\hat{a}^\dagger$	annihilation/ creation operator of photon
α	absorption coefficient
α_U	Urbach like exponential absorption
α_{con}	continuum absorption
$\alpha_{jS_y}^{\Gamma_i^-}$	phonon absorption
α_{bkg}	background absorption beneath exciton resonance
α_{pump}	absorption coefficient in presence of pump and probe laser
α_0	absorption coefficient in presence of probe laser
α_{max}	maximum absorption coefficient
$\hat{b}/\hat{b}^\dagger$	annihilation/ creation operator of emitter
C_U	Urbach amplitude
$C_{jS_y}^{\Gamma_i^-}$	prefactor of function accounting phonon absorption
$C_6(n,n')$	van der Waals coefficient
$C_3(n,n')$	Förster coefficient
C_{plasma}	prefactor related to plasma-contributed linewidth of exciton resonance
$D_f(E)$	Density of final states
$D_0(\omega)$	photon density of states in free space

$D_c(\omega)$	modified photon density of states inside a cavity
ΔE_{int}	energy shift due to Rydberg interaction
ΔE_{sp}	single-particle energy shift due to plasma screening
Δ	shift of band edge from unperturbed band edge
Δ_{eh}	band edge shift due to plasma
ΔE_{eh}	shift of exciton resonance due to plasma
$\Delta\alpha$	change in absorption coefficient
E_C	energy of the light field
E_X	excitation energy of the emitter
$E_{UP,LP}$	energy of upper and lower polariton branch
E_g	bandgap energy
$\tilde{E}_g$	energy of shifted bandgap
E_U	Urbach energy
E_{pump}	pump laser energy
E_{probe}	probe laser energy
ε_0	vacuum permittivity
ε_r	relative permittivity of the material medium
E_n	exciton resonance energy
E_A	thermal activation energy of exciton
$\mathrm{E_{applied}}$	electric field applied to the sample
$\mathrm{E_{induced}}$	field induced inside sample due to exciton dipoles
$\mathrm{E_{eff}}$	effective electric field inside sample
f	oscillator strength of the emitter
g	coupling constant
Γ_{if}	Transition rate
$\Gamma_i^{\pm}$	irreducible representation of the O_h symmetry
Γ_c	spontaneous emission rate of an emitter inside a cavity
Γ_0	spontaneous emission rate of an emitter in free space
Γ_{phonon}	phonon-contributed linewidth of exciton resonance
Γ_{plasma}	plasma-contributed linewidth of exciton resonance
Γ_{total}	total linewidth of exciton resonance
Γ_n	linewidth of exciton resonance
Γ_{cap}	capture rate per exciton density
γ_C	loss rate of photons through cavity mirrors

γ_X	damping rate of the emitter
γ	Keldysh parameter
H_e	Hamiltonian of electron
H'_e	modified Hamiltonian of electron
H_{int}	interaction Hamiltonian
$\hbar$	reduced Planks constant
I_0	impurity PL intensity at very low temperature
I_{pr}	probe laser intensity
I_{gr}	green laser intensity
$I_{gr,cr}$	critical green laser intensity
I_{pu}	pump laser intensity
$I_{pr,ab}$	absorbed probe laser intensity
$I_{pu,ab}$	absorbed pump laser intensity
$I_{gr,ab}$	absorbed green laser intensity
k	momentum
k_{ion}	ionization rate per light intensity
κ_D	inverse Debye screening length
λ	wavelength of light
Λ_a	thermal de Broglie wavelength of plasma
m_e	mass of electron
m_h	mass of hole
M_{eh}	total translational mass of electron and hole complex
N	number of emitters interacting with photons
n_{eh}	plasma density
n_{P1S}	1S-para exciton density
n_{O1S}	1S-ortho exciton density
n_{max}	exciton with maximum principal quantum number
n_{pump}	principal quantum number of pump laser
n_{probe}	principal quantum number of probe laser
O_n	exciton oscillator strength

O^+, O^{++}	oxygen impurities present in sample
p_e	momentum of single electron
p_{eh}	momentum of electron and hole complex
Φ_e	wave function of electron
Φ_h	wave function of hole
Φ^{env}_{nlm}	envelop function of exciton
$\Phi(K,n,l,m)$	wave function of exciton
ϕ	scalar potential of the electromagnetic wave
q_n	asymmetry parameter related to exciton resonance
R^{ex}_y	Rydberg energy of exciton
R^H_y	Rydberg energy of hydrogen atom
R_b	blockade radius
R_{eh}	position of center of mass of electron and hole complex
r_{ion}	ionization rate of neutral exciton
r_{cap}	capture rate of exciton at charged impurity site
ρ_a	plasma density
T_{pr}	transmission of probe laser
$T_{pr,pu}$	pump laser induced transmission of probe laser
T_{bkg}	background transmission
t_{begin}	onset time of pump pulse
t_{end}	end time of pump pulse
t_i	timescale of relaxation channel
T_n	lifetime of exciton
μ_{eh}	reduced mass of electron and hole complex
μ_n, $\mu_{n'}$	dipole moment of exciton
V	mode volume of the cavity
V_b	blockade volume
V_D	screened Coulomb potential
Ω_R	Rabi frequency
ω	angular frequency

$\left\|X_{k_\parallel}\right\|$, $\left\|C_{k_\parallel}\right\|$	in-plane dispersion of Hopfield coefficients
ζ	ratio between thermal escape and radiative decay rate of exciton from impurity site

Bibliography

[1] C. S. Adams, J. D. Pritchard, and J. P. Shaffer. Rydberg atom quantum technologies. *Journal of Physics B: Atomic, Molecular and Optical Physics*, 53(1):012002, 2019.

[2] J. Allen. Photo-ionization of deep impurities in semiconductors. *Journal of Physics C: Solid State Physics*, 2(6):1077, 1969.

[3] M. Aßmann and M. Bayer. Semiconductor Rydberg physics. *Advanced Quantum Technologies*, 3(11):1900134, 2020.

[4] D. G. Baranov, M. Wersall, J. Cuadra, T. J. Antosiewicz, and T. Shegai. Novel nanostructures and materials for strong light–matter interactions. *ACS Photonics*, 5(1):24–42, 2018.

[5] K. Barua, S. Peana, A. D. Keni, V. Mkhitaryan, V. Shalaev, Y. P. Chen, A. Boltasseva, and H. Alaeian. Bottom-up fabrication of 2d Rydberg exciton arrays in cuprous oxide. *arXiv preprint arXiv:2408.03880*, 2024.

[6] M. Bayer, T. L. Reinecke, F. Weidner, A. Larionov, A. McDonald, and A. Forchel. Inhibition and Enhancement of the Spontaneous Emission of Quantum Dots in Structured Microresonators. *Physical Review Letters*, 86(14):3168, 2001.

[7] J. Bellessa, J. Bloch, E. Deleporte, V. Menon, H. Nguyen, H. Ohadi, S. Ravets, and T. Boulier. Materials for excitons–polaritons: Exploiting the diversity of semiconductors. *MRS Bulletin*, 49(9):932–947, 2024.

[8] M. Bergen, V. Walther, B. Panda, M. Harati, S. Siegeroth, J. Heckötter, and M. Aßmann. Large scale purification in semiconductors using Rydberg excitons. *Nature Communications*, 14(1):8235, 2023.

[9] C. I. Blaga, F. Catoire, P. Colosimo, G. G. Paulus, H. G. Muller, P. Agostini, and L. F. DiMauro. Strong-field photoionization revisited. 5(5):335–338.

[10] P. Bloch, B. Meyer, and C. Schwab. Sample thickness dependence of the exciton polariton absorption coefficient in Cu_2O. *Journal of Physics C: Solid State Physics*, 13(2):267, 1980.

[11] A. K. Boddeti, Y. Wang, X. G. Juarez, A. Boltasseva, T. W. Odom, V. Shalaev, H. Alaeian, and Z. Jacob. Reducing Effective System Dimensionality with Long-Range Collective Dipole-Dipole Interactions. *Physical Review Letters*, 132(17):173803, 2024.

[12] D. E. Chang, V. Vuletić, and M. D. Lukin. Quantum nonlinear optics—photon by photon. *Nature Photonics*, 8(9):685–694, 2014.

[13] J. Dahl and A. Switendick. Energy bands in cuprous oxide. *Journal of Physics and Chemistry of Solids*, 27(6-7):931–942, 1966.

[14] G. Dasbach, D. Fröhlich, R. Klieber, D. Suter, M. Bayer, and H. Stolz. Wave-vector-dependent exchange interaction and its relevance for the effective exciton mass in Cu_2O. *Physical Review B*, 70(4):045206, 2004.

[15] G. Dasbach, D. Fröhlich, H. Stolz, R. Klieber, D. Suter, and M. Bayer. Wave-Vector-Dependent Exciton Exchange Interaction. *Physical Review Letters*, 91(10):107401, 2003.

[16] H. Deng, H. Haug, and Y. Yamamoto. Exciton-polariton bose-einstein condensation. *Reviews of modern physics*, 82(2):1489–1537, 2010.

[17] J. O. Dimmock, R. Wheeler, H. Statz, et al. *Properties of the Thirty-Two Point Groups*. Armed Services Technical Information Agency, 1961.

[18] J. D. Dow and D. Redfield. Toward a unified theory of urbach's rule and exponential absorption edges. *Physical Review B*, 5(2):594, 1972.

[19] R. Elliott. Intensity of optical absorption by excitons. *Physical Review*, 108(6):1384, 1957.

[20] N. L. Frazer, R. D. Schaller, and J. Ketterson. Unexpectedly slow two particle decay of ultra-dense excitons in cuprous oxide. *Solid state communications*, 170:34–38, 2013.

[21] M. French, R. Schwartz, H. Stolz, and R. Redmer. Electronic band structure of Cu_2O by spin density functional theory. *Journal of Physics: Condensed Matter*, 21(1):015502, 2008.

[22] J. Frenkel. On the transformation of light into heat in solids. i. *Physical Review*, 37(1):17, 1931.

[23] D. Fröhlich, J. Brandt, C. Sandfort, M. Bayer, and H. Stolz. Anisotropic effective mass of orthoexcitons in Cu_2O. *Physical Review B*, 84(19):193205, 2011.

[24] L. F. Gonçalves and L. G. Marcassa. Control of Rydberg-atom blockade by dc electric-field orientation in a quasi-one-dimensional sample. *Physical Review A*, 94(4):043424, 2016.

[25] J. Grimmel. *Controlling Rydberg atoms in external electric fields*. PhD thesis, Universität Tübingen, 2018.

[26] L. O. Grondahl. The copper-cuprous-oxide rectifier and photoelectric cell. *Reviews of Modern Physics*, 5(2):141, 1933.

[27] E. Gross. Optical spectrum of excitons in the crystal lattice. *Il Nuovo Cimento (1955-1965)*, 3(Suppl 4):672–701, 1956.

[28] E. Gross and N. Karryev. Pogloshchenie sveta kristallom zakisi medi v infrakrasnoi i vidimoi chasti spektra. *Doklady Akademii Nauk SSSR*, 84(2):261–264, 1952.

[29] P. Grünwald, M. Aßmann, J. Heckötter, D. Fröhlich, M. Bayer, H. Stolz, and S. Scheel. Signatures of Quantum Coherences in Rydberg Excitons. *Physical Review Letters*, 117(13):133003, 2016.

[30] M. Hayashi and K. Katsuki. Hydrogen-like absorption spectrum of cuprous oxide. *Journal of the Physical Society of Japan*, 7(6):599–603, 1952.

[31] J. Heckötter. *Strongly interacting Rydberg excitons in Cu_2O*. PhD thesis, Dissertation, Dortmund, Universität Dortmund, 2020, 2020.

[32] J. Heckötter, M. Aßmann, and M. Bayer. Rydberg excitons and quantum sensing. *MRS Bulletin*, pages 1–10, 2024.

[33] J. Heckötter, M. Freitag, D. Fröhlich, M. Aßmann, M. Bayer, P. Grünwald, F. Schöne, D. Semkat, H. Stolz, and S. Scheel. Rydberg Excitons in the Presence of an Ultralow-Density Electron-Hole Plasma. *Physical Review Letters*, 121(9):097401, 2018.

[34] J. Heckötter, M. Freitag, D. Fröhlich, M. Aßmann, M. Bayer, M. Semina, and M. Glazov. High-resolution study of the yellow excitons in Cu_2O subject to an electric field. *Physical Review B*, 95(3):035210, 2017.

[35] J. Heckötter, M. Freitag, D. Fröhlich, M. Aßmann, M. Bayer, M. Semina, and M. Glazov. Scaling laws of Rydberg excitons. *Physical Review B*, 96(12):125142, 2017.

[36] J. Heckötter, M. Freitag, D. Fröhlich, M. Aßmann, M. Bayer, M. Semina, and M. Glazov. Dissociation of excitons in Cu_2O by an electric field. *Physical Review B*, 98(3):035150, 2018.

[37] J. Heckötter, D. Janas, R. Schwartz, M. Aßmann, and M. Bayer. Experimental limitation in extending the exciton series in Cu_2O towards higher principal quantum numbers. *Physical Review B*, 101(23):235207, 2020.

[38] J. Heckötter, B. Panda, K. Brägelmann, M. Harati, and M. Aßmann. Neutralization of impurities by continuous-wave excitation of high-*n* Rydberg excitons. *Phys. Rev. B*, 108:235212, Dec 2023.

[39] J. Heckötter, V. Walther, S. Scheel, M. Bayer, T. Pohl, and M. Aßmann. Asymmetric Rydberg blockade of giant excitons in cuprous oxide. *Nature communications*, 12(1):3556, 2021.

[40] M. Hertzog, M. Wang, J. Mony, and K. Börjesson. Strong light–matter interactions: a new direction within chemistry. *Chemical Society Reviews*, 48(3):937–961, 2019.

[41] T. Ito and T. Masumi. Detailed examination of relaxation processes of excitons in photoluminescence spectra of Cu_2O. *Journal of the Physical Society of Japan*, 66(7):2185–2193, 1997.

[42] T. Ito, H. Yamaguchi, K. Okabe, and T. Masumi. Single-crystal growth and characterization of Cu_2O and CuO. *Journal of materials science*, 33:3555–3566, 1998.

[43] T. Itoh and S.-i. Narita. Analysis of wavelength derivative spectra of exciton in Cu_2O. *Journal of the Physical Society of Japan*, 39(1):140–147, 1975.

[44] J. Jang, Y. Sun, B. Watkins, and J. Ketterson. Bound excitons in Cu_2O: efficient internal free exciton detector. *Physical Review B*, 74(23):235204, 2006.

[45] J. Jang and J. Wolfe. Exciton decay in Cu_2O at high density and low temperature: Auger recombination, spin–flip scattering, and molecule formation. *Solid state communications*, 137(1-2):91–96, 2006.

[46] T. Jenkins. A brief history of... semiconductors. *Physics education*, 40(5):430, 2005.

[47] Y. Jiao, J. Bai, R. Song, S. Bao, J. Zhao, and S. Jia. Electric field tuned dipolar interaction between Rydberg atoms. *Frontiers in Physics*, 10:892542, 2022.

[48] D. Johnston. Stretched exponential relaxation arising from a continuous sum of exponential decays. *Physical Review B*, 74(18):184430, 2006.

[49] A. V. Kavokin, J. J. Baumberg, G. Malpuech, and F. P. Laussy. *Microcavities*, volume 21. Oxford university press, 2017.

[50] G. Kavoulakis and A. Mysyrowicz. Auger decay, spin exchange, and their connection to bose-einstein condensation of excitons in Cu_2O. *Physical Review B*, 61(24):16619, 2000.

[51] T. Kazimierczuk, D. Fröhlich, S. Scheel, H. Stolz, and M. Bayer. Giant Rydberg excitons in the copper oxide Cu_2O. *Nature*, 514(7522):343–347, 2014.

[52] L. V. Keldysh. Ionization in the field of a strong electromagnetic wave. *Zh. Eksperim. i Teor. Fiz.*, 47, 1964.

[53] D. Kleppner. Inhibited Spontaneous Emission. *Physical Review Letters*, 47(4):233, 1981.

[54] C. F. Klingshirn. *Semiconductor Optics*. Springer, Berlin ; New York, third edition, 2007.

[55] S. M. Kogan and T. Lifshits. Photoelectric spectroscopy–a new method of analysis of impurities in semiconductors. *physica status solidi (a)*, 39(1):11–39, 1977.

[56] S. Koirala, N. Naka, and K. Tanaka. Correlated lifetimes of free paraexcitons and excitons trapped at oxygen vacancies in cuprous oxide. *Journal of luminescence*, 134:524–527, 2013.

[57] S. Koirala, M. Takahata, Y. Hazama, N. Naka, and K. Tanaka. Relaxation of localized excitons by phonon emission at oxygen vacancies in Cu_2O. *Journal of luminescence*, 155:65–69, 2014.

[58] S. O. Krüger, H. Stolz, and S. Scheel. Interaction of charged impurities and Rydberg excitons in cuprous oxide. *Phys. Rev. B*, 101:235204, Jun 2020.

[59] A. Lambrecht, J.-M. Courty, S. Reynaud, and E. Giacobino. Cold atoms: A new medium for quantum optics. *Applied Physics B*, 60:129–134, 1995.

[60] J. Loison, M. Robino, and C. Schwab. Progress in melt growth of Cu_2O. *Journal of Crystal Growth*, 50(4):816–822, 1980.

[61] L. Łukasiak and A. Jakubowski. History of semiconductors. *Journal of Telecommunications and information technology*, (1):3–9, 2010.

[62] S. A. Lynch, C. Hodges, S. Mandal, W. Langbein, R. P. Singh, L. A. Gallagher, J. D. Pritchett, D. Pizzey, J. P. Rogers, C. S. Adams, et al. Rydberg excitons in synthetic cuprous oxide Cu_2O. *Physical Review Materials*, 5(8):084602, 2021.

[63] M. Makhonin, A. Delphan, K. W. Song, P. Walker, T. Isoniemi, P. Claronino, K. Orfanakis, S. K. Rajendran, H. Ohadi, J. Heckötter, et al. Nonlinear Rydberg exciton-polaritons in Cu_2O microcavities. *Light: Science & Applications*, 13(1):47, 2024.

[64] P. R. Markworth, R. P. Chang, Y. Sun, G. Wong, and J. B. Ketterson. Epitaxial stabilization of orthorhombic cuprous oxide films on MgO (110). *Journal of Materials Research*, 16(4):914–921, 2001.

[65] N. Matsuda, R. Shimizu, Y. Mitsumori, H. Kosaka, and K. Edamatsu. Observation of optical-fibre Kerr nonlinearity at the single-photon level. *Nature photonics*, 3(2):95–98, 2009.

[66] H. Matsumoto, K. Saito, M. Hasuo, S. Kono, and N. Nagasawa. Revived interest on yellow-exciton series in Cu_2O: An experimental aspect. *Solid state communications*, 97(2):125–129, 1996.

[67] C. McCormick, D. Solli, R. Chiao, and J. Hickmann. Saturable nonlinear refraction in hot atomic vapor. *Physical Review A*, 69(2):023804, 2004.

[68] C. Morin, J. Tignon, J. Mangeney, S. Dhillon, G. Czajkowski, K. Karpiński, S. Zielińska-Raczyńska, D. Ziemkiewicz, and T. Boulier. Self-Kerr Effect across the Yellow Rydberg Series of Excitons in Cu_2O. *Physical Review Letters*, 129(13):137401, 2022.

[69] J. Mund, D. Fröhlich, D. R. Yakovlev, and M. Bayer. High-resolution second harmonic generation spectroscopy with femtosecond laser pulses on excitons in Cu_2O. *Physical Review B*, 98(8):085203, 2018.

[70] N. Nilius, J. Goniakowski, and C. Noguera. A surface science view onto cuprous oxide: Growth, termination, electronic structure and optical response. *Surface Science Reports*, page 100622, 2024.

[71] J. W. Orton. *Semiconductors and the information revolution: magic crystals that made IT happen*. Academic Press, 2009.

[72] E. Paik, L. Zhang, K. Fai Mak, J. Shan, and H. Deng. Excitons and polaritons in two-dimensional transition metal dichalcogenides: a tutorial. *Advances in Optics and Photonics*, 16(4):1064–1132, 2024.

[73] A. S. Paul, S. K. Rajendran, D. Ziemkiewicz, T. Volz, and H. Ohadi. Local tuning of Rydberg exciton energies in nanofabricated Cu_2O pillars. *Communications Materials*, 5(1):43, 2024.

[74] F. Pei, S. Wu, G. Wang, M. Xu, S.-Y. Wang, L.-Y. Chen, and Y. Jia. Electronic and optical properties of noble metal oxides M_2O (M= Cu, Ag and Au): first-principles study. *Journal of the Korean Physical Society*, 55(3):1243–1249, 2009.

[75] I. Pelant and J. Valenta. *Luminescence spectroscopy of semiconductors*. OUP Oxford, 2012.

[76] Y. Peter and M. Cardona. *Fundamentals of semiconductors: physics and materials properties*. Springer Science & Business Media, 2010.

[77] T. Peyronel, O. Firstenberg, Q.-Y. Liang, S. Hofferberth, A. V. Gorshkov, T. Pohl, M. D. Lukin, and V. Vuletić. Quantum nonlinear optics with single photons enabled by strongly interacting atoms. *Nature*, 488(7409):57–60, 2012.

[78] J. D. Pritchett, L. A. Gallagher, A. Brewin, H. Q. Wong, W. Langbein, S. A. Lynch, C. S. Adams, and M. Jones. Giant microwave–optical Kerr nonlinearity via Rydberg excitons in cuprous oxide. *APL Photonics*, 9(3), 2024.

[79] A. Rahimi-Iman. Polariton physics. *Springer Series in Optical Sciences (Springer International Publishing, 2020)*, 229, 2020.

[80] B. K. Ridley. *Quantum processes in semiconductors*. Oxford University Press, USA, 2013.

[81] J. Robertson. Electronic structure and x-ray near-edge core spectra of Cu_2O. *Physical Review B*, 28(6):3378, 1983.

[82] J. P. Rogers, L. A. P. Gallagher, D. Pizzey, J. D. Pritchett, C. S. Adams, M. P. A. Jones, C. Hodges, W. Langbein, and S. A. Lynch. High-resolution nanosecond spectroscopy of even-parity Rydberg excitons in Cu_2O. *Phys. Rev. B*, 105:115206, Mar 2022.

[83] E. Ruiz, S. Alvarez, P. Alemany, and R. A. Evarestov. Electronic structure and properties of Cu_2O. *Physical Review B*, 56(12):7189, 1997.

[84] M. Saffman. Quantum computing with atomic qubits and Rydberg interactions: progress and challenges. *Journal of Physics B: Atomic, Molecular and Optical Physics*, 49(20):202001, 2016.

[85] K. Saito, M. Hasuo, T. Hatano, and N. Nagasawa. Band gap energy and binding energies of Z3-excitions in CuCl. *Solid state communications*, 94(1):33–35, 1995.

[86] F. Schöne, S.-O. Krüger, P. Grünwald, M. Aßmann, J. Heckötter, J. Thewes, H. Stolz, D. Fröhlich, M. Bayer, and S. Scheel. Coupled valence band dispersions and the quantum defect of excitons in Cu_2O. *Journal of Physics B: Atomic, Molecular and Optical Physics*, 49(13):134003, 2016.

[87] F. Schöne, S.-O. Krüger, P. Grünwald, H. Stolz, S. Scheel, M. Aßmann, J. Heckötter, J. Thewes, D. Fröhlich, and M. Bayer. Deviations of the exciton level spectrum in Cu_2O from the hydrogen series. *Physical Review B*, 93(7):075203, 2016.

[88] F. Schöne, H. Stolz, and N. Naka. Phonon-assisted absorption of excitons in Cu_2O. *Physical Review B*, 96(11):115207, 2017.

[89] F. Schweiner, J. Main, M. Feldmaier, G. Wunner, and C. Uihlein. Impact of the valence band structure of Cu_2O on excitonic spectra. *Physical Review B*, 93(19):195203, 2016.

[90] D. Semkat, H. Fehske, and H. Stolz. Influence of electron-hole plasma on Rydberg excitons in cuprous oxide. *Physical Review B*, 100(15):155204, 2019.

[91] D. Semkat, H. Fehske, and H. Stolz. Quantum many-body effects on Rydberg excitons in cuprous oxide. *The European Physical Journal Special Topics*, 230(4):947–950, 2021.

[92] D. K. Sharma, S. Shukla, K. K. Sharma, and V. Kumar. A review on ZnO: Fundamental properties and applications. *Materials Today: Proceedings*, 49:3028–3035, 2022.

[93] R. Sharma and S. Rodriguez. Theory of excitons bound to ionized impurities in semiconductors. *Physical Review*, 153(3):823, 1967.

[94] X.-F. Shi. Quantum logic and entanglement by neutral Rydberg atoms: methods and fidelity. *Quantum Science and Technology*, 7(2):023002, 2022.

[95] T. Skettrup, M. Suffczynski, and W. Gorzkowski. Properties of excitons bound to ionized donors. *Phys. Rev. B*, 4:512–517, Jul 1971.

[96] S. Steinhauer, M. A. Versteegh, S. Gyger, A. W. Elshaari, B. Kunert, A. Mysyrowicz, and V. Zwiller. Rydberg excitons in Cu_2O microcrystals grown on a silicon platform. *Communications Materials*, 1(1):11, 2020.

[97] H. Stolz and D. Semkat. Scattering of Rydberg excitons by phonon-plasmon modes. *Journal of Physics: Condensed Matter*, 33(42):425701, 2021.

[98] H. Stolz, D. Semkat, R. Schwartz, J. Heckötter, M. Aßmann, W.-D. Kraeft, H. Fehske, and M. Bayer. Scrutinizing the debye plasma model: Rydberg excitons unravel the properties of low-density plasmas in semiconductors. *Physical Review B*, 105(7):075204, 2022.

[99] M. Takahata and N. Naka. Photoluminescence properties of the entire excitonic series in Cu_2O. *Physical Review B*, 98(19):195205, 2018.

[100] D. Thomas. The exciton spectrum of zinc oxide. *Journal of Physics and Chemistry of Solids*, 15(1-2):86–96, 1960.

[101] Y. Toyozawa. Interband effect of lattice vibrations in the exciton absorption spectra. *Journal of Physics and Chemistry of Solids*, 25(1):59–71, 1964.

[102] D. Trauernicht and J. Wolfe. Drift and diffusion of paraexcitons in Cu_2O: Deformation-potential scattering in the low-temperature regime. *Physical Review B*, 33(12):8506, 1986.

[103] L. C. Tropf. *Strong light-matter coupling in organic microcavities: investigating the fundamental principles of strong coupling in strongly disordered materials experimentally*. PhD thesis, University of St Andrews, 2019.

[104] T. Ueno. On the contour of the absorption lines in Cu_2O. *Journal of the Physical Society of Japan*, 26(2):438–446, 1969.

[105] C. Uihlein, D. Fröhlich, and R. Kenklies. Investigation of exciton fine structure in Cu_2O. *Physical Review B*, 23(6):2731, 1981.

[106] V. Walther. *Nonlinear Optics with Rydberg Excitions*. PhD thesis, Technische Universität Dresden, 2019.

[107] V. Walther, P. Grünwald, and T. Pohl. Controlling Exciton-Phonon Interactions via Electromagnetically Induced Transparency. *Physical Review Letters*, 125(17):173601, 2020.

[108] V. Walther, S. O. Krüger, S. Scheel, and T. Pohl. Interactions between Rydberg excitons in Cu_2O. *Physical Review B*, 98(16):165201, 2018.

[109] V. Walther and T. Pohl. Plasma-Enhanced Interaction and Optical Nonlinearities of Cu_2O Rydberg Excitons. *Physical Review Letters*, 125(9):097401, 2020.

[110] G. Wang, A. Chernikov, M. M. Glazov, T. F. Heinz, X. Marie, T. Amand, and B. Urbaszek. Colloquium: Excitons in atomically thin transition metal dichalcogenides. *Reviews of Modern Physics*, 90(2):021001.

[111] S. Wang, J. Yuan, L. Wang, L. Xiao, and S. Jia. Measurement of the Kerr nonlinear refractive index of the Rb vapor based on an optical frequency comb using the z-scan method. *Optics Express*, 28(25):38334–38342, 2020.

[112] G. H. Wannier. The structure of electronic excitation levels in insulating crystals. *Physical Review*, 52(3):191, 1937.

[113] J. P. Wolfe and J. I. Jang. The search for Bose-Einstein condensation of excitons in Cu_2O: exciton-Auger recombination versus biexciton formation. *New Journal of Physics*, 16(12):123048, 2014.

[114] A. Zheltikov. Laser-induced tunneling, the Kapitza effective potential, and the limits of perturbative nonlinear optics. *Opt. Express*, 27(6):8246–8257, Mar 2019.

List of Publications

1. **B. Panda**, J. Heckötter and M. Aßmann, Dynamics of purification in semiconductors using Rydberg excitons, * in preparation

2. **B. Panda**, J. Heckötter, S. Siegeroth, M. Harati and M. Aßmann, Effective interaction dynamics of Rydberg excitons, arXiv preprint arXiv:2409.14960, 2024.

3. J. Heckötter, **B. Panda**, K. Brägelmann, M. Aßmann and M. Bayer, A Temperature Study of High-n Rydberg States in Cu_2O, Advanced Quantum Technologies, 2300426 (2024).

4. J. Heckötter, **B. Panda**, K. Brägelmann, M. Harati and M. Aßmann, Neutralisation of impurities by continuous-wave excitation of high-n Rydberg excitons, Physical Review B 108, 235212 (2023)

5. M. Bergen, V. Walther, **B. Panda**, M. Harati, S. Siegeroth, J. Heckötter and M. Aßmann, Large scale purification in semiconductors using Rydberg excitons, Nature Communications 14 (1), 8235 (2023).

6. A. Neubauer, J. Heckötter, M. Ubl, M. Hentschel, **B. Panda**, M. Aßmann, M. Bayer and H. Giessen, Spectroscopy of nanoantenna-covered Cu_2O: Towards enhancing quadrupole transitions in Rydberg excitons, Physical Review B 106 (16), 165305 (2022)